Title
Paleomagnetic and stratigraphic techniques for identifying sediment processes on continental margins

Author
Schwehr, Kurt

Publication Date
2006

Peer reviewed|Thesis/dissertation

UNIVERSITY OF CALIFORNIA, SAN DIEGO

Paleomagnetic and Stratigraphic Techniques for Identifying Sediment Processes on Continental Margins

A dissertation submitted in partial satisfaction of the
requirements for the degree Doctor of Philosophy
in
Earth Sciences

by

Kurt Schwehr

Committee in charge:

Professor Lisa Tauxe, Co-Chair
Professor Neal Driscoll, Co-Chair
Professor Scott Ashford
Professor Kevin Brown
Professor Yuri Fialko
Professor Catherine Johnson

2006

The dissertation of Kurt Schwehr is approved, and it is acceptable in quality and form for publication on microfilm:

Co-Chair

Co-Chair

University of California, San Diego

2006

To Sarah and Bailey

TABLE OF CONTENTS

LIST OF FIGURES

LIST OF TABLES

ACKNOWLEDGMENTS

I have depended on the help and support of many people, both at Scripps Institution of Oceanography, and outside of the Institution. Too many have contributed or encouraged me to mention them all. I must start with a memorial to the Mars Polar Lander whose crash landing on Mars convinced me that it was time to go back for my doctorate.

This dissertation is inspired by the work of Matt Cronin, Peter Selkin, and Lisa Tauxe. Without their hard work and their "noise in the quiet zone" this thesis would never have happened. I am grateful to Neal Driscoll for arriving just in the nick of time to round out this thesis with his intelligence, wit, charm, and the super chirp. Lisa and Neal are two truly amazing advisors.

I am grateful for the financial support from a wide range of people and organizations: CalIT^2, JPL Solar System Visualization, the Nimitz Fellowship, NSF, ONR, John Orcutt, and the SIO Visualization Center. Additionally, Neal Driscoll, Catherine Johnson, and Lisa Tauxe supported me immensely in between the funding from the other sources. Additionally, Jeff Gee spent many hours working to improve the software in the paleomagnetic laboratory, which saved me untold hours while measuring samples.

I would like to thank my fellow lab and office mates who kept me company through many days and nights on ships and at SIO through the 5 years of this journey. Those included are Danny Brothers, Laurent Beguery, Julie Bowels, Jeff Dingler, Rebecca Fenwick, Roi Granot, Jenna Hill, Leah Hogarth, Liz Johnstone, Nico Le Dantec, Peter Selkin, Travis Smith, Aurelio Tinio, Jose, Robin, Stef, the OSU coring group, and the crews of the R/V Sproul and R/V Thompson. The advice and patience of the magnetics and stratigraphy groups has been critical to my understanding of these two very different fields.

No thesis would be possible without the advice and help of all of the technical people who keep the labs and ships in working order. They have spent immeasurable hours answering my every question, and keeping me in good spirits.

In the Paleomagnetic Laboratory, the cast includes Steve DiDonna, Winter Miller, Jason Steindorf, and Andrew Harris. In the Geologic Collections, I could not have survived the core processing with out the help of Jerry Bode, Dick Norris, Warren Smith, and Paula Worstell. In the stratigraphic world, there was Christie Lindemann who was always cheerful, no matter what.

It has been a pleasure to be a part of the geologic community. Many people have provided access to data and valuable discussions. The list includes J. Borgeld, R. Burger, D. Caress, B. Edwards, G. Fulthorpe, J. Gardner, K. Kodama, H.J. lee, J. Locat, L. Mayer, G. Mountain, J. Rosenbaum, and many others.

During my time at SIO, I am extremely thankful for two very exiting experiences that I got to participate in outside of my thesis. The first was an invitation by Steve Cande to join a research cruise to Antarctica. The second was the offer extended by Eric DeJong, Barbara McGuffie, and Steve Levoe to join the Mars Exploration Rover Mission. I want to thank everyone that I worked with on the mission, and Catherine Johnson for advising me throughout the process. I have never met so many people in such a short time.

It is difficult to know where to start in acknowledging the role of my family throughout my entire life. My parents, Bob and Linda, and my sister, Kiley, mean the world to me. Throughout our countless family journeys across the western half of the US, my parents have exposed me to more geology than any academic program. They instilled in me a deep curiosity about all that surrounds us. Some of my favorite childhood memories include things like the whole family helping me collect Mt. Saint Helens volcanic ash off of plants at a rest stop in Washington state and my parents staying up all night with me to watch the first launch of the Space Shuttle on TV. My family has been with me through the entire adventure and I could not have done it without their love and support.

Finally, my most profound thanks goes to my wife, Sarah Raymond, to whom this thesis is dedicated in love and joy. Her companionship, advice, and encouragement made this all worthwhile.

Chapter 2, in full, is a reprint of the material as it appears in *Geology*, vol. 31, no. 3, p. 203-206, Characterization of soft-sediment deformation: Detection of cryptoslumps using magnetic methods, Schwehr, Kurt; Tauxe, Lisa; 2003.

I carried out all of the measurements used in the chapter, however the sampling of the cores was done by Matt Cronin, Peter Selkin, and Lisa Tauxe. Lisa Tauxe provided advice on the laboratory methods, data processing, and analysis. Tauxe also edited the paper in addition to teaching me how to use her PMAG software and the LaTeX document processing system. Neal Driscoll provided advice and discussion on interpretations of the paleoenvironment of the Ardath Shale.

Chapter 3, in full, is the material as submitted to *Geochemistry, Geophysics, Geosystems*, Detecting Compaction Disequilibrium with Anisotropy of Magnetic Susceptibility, Schwehr, Kurt; Tauxe, Lisa; Driscoll, Neal; Lee, Homa; 2006.

The CHIRP seismic data and cores were collected on the BPSIO-2004 cruise with Jeff Dingler and Kurt Schwehr as Co-Chief Scientists for that portion of the cruise. I was responsible for all of the core processing, CHIRP processing, analytical work, and data analysis. The data interpretation was done in conjunction with Lisa Tauxe, Neal Driscoll, and Homa Lee. Jeff Gee provided valuable advice and discussion. Lisa Tauxe, Neal Driscoll, and Homa Lee edited the text.

Chapter 4, in full, is the material as submitted to *Marine Geology*, Origin of continental margin morphology: submarine-slide or downslope current-controlled bedforms, a rock magnetic approach, Schwehr, Kurt; Driscoll, Neal; Tauxe, Lisa; 2006.

The CHIRP seismic data was collected by Neal Driscoll on cruise TTN-096. The cores were acquired on cruise TTN-136B with Kurt Schwehr as Chief Scientist using the OSU Coring Group. I was responsible for all of the core processing, CHIRP processing, analytical work, and data analysis. A portion of the magnetic measurements were performed by Andrew Harris and Jason Steindorf. Jim Gardner assisted with the processing of the Huntec seismic data. The data interpretation was done in conjunction with Neal Driscoll and Lisa Tauxe. Lisa Tauxe and Neal Driscoll edited the text.

VITA

1989-1990	Associate Researcher, NASA Ames Research Center
1991-1996	Consultant to the USGS, SETI, and NASA Ames
1996	B.S., Geology, Stanford University
1996-2000	Computer Scientist, NASA Ames Research Center
1998-1999	Visiting Scientist, Field Robotics Center, Carnegie Mellon University
2003-2004	MER Flight Team, Jet Propulsion Laboratory
2000-2006	Ph.D. student, University of California San Diego
2006	Ph.D., University of California San Diego

PUBLICATIONS

K. D. Schwehr, N. W. Driscoll, and L. Tauxe. Origin of continental margin morphology: submarine-slide or downslope current-controlled bedforms, a rock magnetic approach. Submitted to *Marine Geology*, 2006.

K. D. Schwehr, L. Tauxe, and N. W. Driscoll. Detecting Compaction Disequilibrium with Anisotropy of Magnetic Susceptibility. Submitted to *Geochemistry, Geophysics, Geosystems*, 2006.

K. D. Schwehr, A. Derbes, L. Edwards, L. Nguyen, and E. Zbinden. Designing visualization software for ships and robotic vehicles. *IS&T/SPIE*, 5669-23, 2005.

K. D. Schwehr, C. L. Johnson, D. Kilb, A. Nayak, and C. Nishimura. Visualization tools facilitate geological investigations of Mars exploration rover landing sites *IS&T/SPIE*, 5669-15, 2005.

K. Schwehr and L. Tauxe. Characterization of soft sediment deformation: Detection of crypto-slumps using magnetic methods. *Geology*, 31(3): 203-206, 2003.

Cabrol et al. Nomad Rover Field Experiment, Atacama Desert, Chile: 1. Science results overview. *JGR* 106(E4):7785-7806, 2001.

Nguyen et al. Virtual reality interfaces for visualization and control of remote vehicles. *Autonomous Robots*, 11(1): 59-68, 2001.

Stoker et al. Analyzing Pathfinder Data using Virtual Reality and Super-resolved Imaging. *JGR*, 104 (E4): 8889-8906, 1999.

Stoker et al. Exploration Of Mono Lake With An ROV: a prototype experiment for the MAPS AUV program. *IEEE AUV Technology*. 1996.

ABSTRACT OF THE DISSERTATION

Paleomagnetic and Stratigraphic Techniques for Identifying Sediment Processes on Continental Margins

by

Kurt Schwehr
Doctor of Philosophy in Earth Sciences
University of California, San Diego, 2006
Professor Lisa Tauxe, Co-Chair
Professor Neal Driscoll, Co-Chair

Understanding the origin of stratigraphic and morphologic features, whether they are formed by primary deposition or are the consequence of post-depositional alteration, is the critical first step to determining the history and evolution of continental margins. I have developed a new approach that when combined with prior geological and geophysical data, provides new constraints on the origin of stratigraphic sequences. This approach can detect high water content that could evolve into overpressure. Such zones have the potential to develop into slope failures. In addition, this approach can determine if morphologic features observed on many continental margins are current-controlled bedforms or retrogressive slides. The method combines anisotropy of magnetic susceptibility (AMS) with CHIRP seismic data, which provides new insights into the processes responsible for strata formation. First, I explore the limb of a slump in the Ardath Shale in the cliffs of La Jolla, CA. Laterally adjacent to the observed slump, AMS is able to identify a "crypto-slump" that is not directly identifiable in outcrop. Next, a study of the Santa Barbara basin explores the rapid deposition and deformation occurring on the northern slope, where AMS combined with other rock magnetic techniques distinguished diagenesis from zones of excess water and overconsolidation. Finally,

I use the AMS approach to address the controversy regarding the formation of the Humboldt Slide. Based on morphology observed in CHIRP seismic data and the AMS signature of collocated piston cores, the Humboldt Slide is composed of a series of sediment waves, not a thin skinned deformation feature.

Chapter I

Introduction

The overarching goal of this thesis is to understand the origin of depositional features observed on continental margins. It is important to determine if these features record primary deposition or have undergone post-depositional alteration. Often it is difficult to distinguish between the two. Here I present a new approach which places constraints on the processes that form stratigraphy on continental margins. Defining the processes which form stratigraphy is the critical first step toward understanding continental margin development and evolution.

I.A Slope failure and slumps

Several mechanisms have been proposed for triggering submarine failures, however, how these processes act alone or in concert remains poorly understood. The infrequent occurrence and the challenge of underwater sensing means that most slope failures are examined after the fact by observing the slide scar and consequent slide deposit. Researchers then attempt to reconstruct the sequence of events that led to the resulting morphology. It appears that upslope migration paths for gas-charged fluids, permeability structures imparted by downslope creep, and bedding planes may all play an important role in governing slope failure. Our working hypothesis is that cracks observed on continental margins might represent the initial stage of slope failure of the outer shelf and upper slope, and may become headwalls of future submarine landslides such as the Goleta Slide (Fisher et al., 2005), US East Coast (Driscoll et al., 2000; Hill et al., 2004), and the Storegga Slide (Evans et al., 1996). The impetus for studying slope failure is two-fold. First, new knowledge about slope instability and failures will lead to a greater understanding of how cycles of broad-scale mass wasting, canyon cutting, and sedimentation interact to shape the observed morphology of continental margins. Second, from a societal perspective it is important to understand these features as any submarine landslides nucleating on a continental margin might generate tsunami that pose a danger to populations and infrastructure along the adjacent coast and margin.

The study of the Ardath Shale, demonstrated that this AMS approach was able to detect minor post-depositional deformation (Figure I.2:1). Several studies have used deflection of the eigenvector associated with the minimum in susceptibility, V_3, as a criterion to identify post-depositional deformation. However, this criteria does not work in all cases. We examined the AMS record of a well-exposed slump and found that although demonstrable deformation can occur without deflecting the V_3 directions, an oblate AMS fabric is transformed into a triaxial fabric during the initial deformation. Thus, transformation of the fabric from oblate to triaxial can occur during initial stages of slumping without deflection of the V_3 axes. We suggest that subtle soft-sediment deformation can be detected by using AMS fabric combined with examination of V_3.

In clay-rich sediment, micro and macro structures influence how the sediments deform when under stress. When lithology is fairly constant, anisotropy of magnetic susceptibility (AMS) can be a simple technique for measuring the relative consolidation state of sediment, which reflects the sediment burial history. AMS can reveal areas of excess water that may evolve into zones of overpressure and apparent overconsolidation (collectively known as compaction disequilibria; Mello and Karner, 1996) associated with unconformities where sediment overburden has been removed. By utilizing AMS on cores collected in the Santa Barbara Basin (Figure I.2:2), we were able to identify a number of compaction disequilibria on the northern slope of the basin: an unconformity, and several zones of excess water. Zones of excess water may evolve into overpressured layers, that could in turn create zones of weakness in the strata that may localize failure or slide surfaces (Dugan and Flemings, 2000), whereas unconformities may lead to apparent overconsolidation that record past failures and erosion. Mello and Karner (1996) describe deviations from normal consolidation as compaction disequilibria. With the AMS tool able to detect minor deformation and "crypto-slumps", it provides a powerful new approach to test between the two proposed hypotheses for the formation of sedimentary features observed on many continental slopes.

I.B Bedforms or slumps

Landslides on continental margins can have a devastating effect on the coastal environment because of the possibility of tsunamis and the ensuing coastal erosion. Accurate risk assessment demands that we know the probability of large landslides occurring, as a result, it is imperative to know the frequency of landslide events in the past. To assess frequency, it is necessary to identify, with some certainty, features that are products of slope failure. Given the controversy surrounding identification of features such as the Humboldt Slide, the development of criteria for positive identification of post-depositional deformation gains urgency. Seismic and outcrop stratigraphic studies have shown that margin sedimentary successions are pervaded by physical discontinuities that occur over a wide range of scales, and are generated by various processes acting separately or in concert (Christie-Blick and Driscoll, 1995).

Geologists have long appreciated the importance of submarine landslides and failures in the development of unconformities (Embley and Jacobi, 1986; Booth et al., 1993; Evans et al., 1996). Recently there has been much debate concerning the identification of submarine landslides and rotational slumps in seismic reflection data (Dillon et al., 1993; Gardner et al., 1999; Holbrook, 2001; Holbrook et al., 2002; Lee et al., 2002; Trincardi et al., 2004). The controversy arises, in large part, because the stratal geometry of many deposits, previously identified as retrogressive slumps, is not unique and could equally be generated from down- or along-slope currents (e.g. Blake-Bahama collapse structure, Figure I.1; Holbrook et al., 2002; Humboldt Slide in the Eel River basin, Figure I.2:3). Deposition and erosion of the slope may be caused by a number of different processes (e.g., slope failure, incision and overbank deposits, bottom currents, shelf-edge deltas). Understanding how these processes sculpt the continental slope is critical to generating quantitative geologic models of continental slope evolution (Pratson and Coakley, 1996; Driscoll and Diebold, 1999). Developing a test to discriminate between these

alternative scenarios (i.e., retrogressive slumps versus current-controlled deposits) would provide valuable new insights into the origin of these deposits and their relative importance in the construction and evolution of continental margins.

Gardner et al. (1999) interpret the Humboldt Slide as retrogressive failure a with rotation of blocks above a shear zone. In contrast, Lee et al. (2002) reinterpreted the Humboldt Slide complex as a series of sediment waves emplaced by downslope gravity flows that infill a slide scar. The differing interpretations of the slide structure by Gardner et al. (1999) and Lee et al. (2002) highlight the ongoing controversy regarding the origin of this type of morphological features on continental margins. These two interpretations (primary depositional features versus retrogressive faulting and internal deformation) are based on the same Huntec (Dodds, 1980) seismic data set.

Seismic data alone may be able to answer the question as to the origin of these features, but at a great expense and without independent confirmation of their origin. For example, Holbrook (2001) reinterpreted existing USGS data from the Blake-Bahama outer ridge and refined the previous interpretation of Dillon et al. (1993) that certain features were normal faults associated with a gas-hydrate collapse structure. By examining the stratal geometry, Holbrook (2001) suggested the structures were growth faults recording several events, not just one event as suggested by Dillon et al. (1993). Subsequently, Holbrook et al. (2002) conducted an expensive 3D seismic survey, that suggested the features were actually sediment waves.

For sedimentary sequences with small variations in facies, many processes are difficult to detect with remote sensing. This dissertation combines CHIRP seismic profiles with magnetic properties of cores to understand sedimentological evolution of continental shelves and slopes. A range of magnetic techniques are employed, but the main focus is on AMS as a proxy for grain level fabric changes imparted by depositional processes and post-depositional alteration.

Many geologic studies examine sedimentary sequences to determine the

tectonic and climatic history of the region. Stratigraphy is the tape recorder of earth history. However, the sedimentary record is often incomplete or altered. It is critical to have a wide arsenal of tools available to determine the link between depositional process and the preserved stratigraphy.

Many criteria are used today to determine the stability of sedimentary layers. They range from Zijderveld plots in paleomagnetic demagnetization studies (Zijderveld, 1967) to visual core description of slumps and slides in wet sediment cores. Most studies of paleoclimate and paleomagnetic fields pose the question, "To what extent has the sediment been altered after deposition?" Large amounts of strain often leave clear visual and structural clues, but the greater challenge resides in detecting and understanding the small scale deformation and alteration features. These features may either be pervasive or localized. If these features can be identified, it may be possible to correct for the deformation, increase the error estimation, or simply reject one or more data points as erroneous.

Current techniques for evaluating small scale deformation are often difficult or expensive. For example, on the sample scale, methods such as microscopic thin sections are challenging to acquire from wet sediments without drying or difficult epoxy injections. Conducting a robust statistical analysis to characterize sediment fabric with these techniques is not expensive, but is extremely time consuming and has associated statistical sampling pitfalls. On a regional scale, high resolution seismic profiles can often resolve ambiguous features with high density seismic surveys. Such studies are often cost prohibitive requiring large amounts of ship time.

In this thesis, I will focus on the paleomagnetic technique of AMS because it is a tool that has great potential to detect small changes in sedimentary fabric. The magnetic fabric of geological materials, and in particular of sediments, has been a focus of interest for decades (e.g. Ising, 1942; Granar, 1958; Rees, 1965). The new testing method outlined in this thesis underscores the relevance of previous AMS fabric work and adds to the suite of tests for fabric changes.

I will first present a study of a slump in the Ardath Shale (La Jolla, CA; Figure I.2:1). This study shows the potential of AMS to detect small amounts of deformation (termed "crypto-slumps"). Next, the technique will be applied to wet sediment cores from the Gaviota Slide structure off shore of Santa Barbara, CA (Figure I.2:2). To help with understanding of the statistical methods, I will compare this method to those previously employed on cores to illustrate why a range of tests provide a complementary strategy.

Finally, I apply the new set of statistical techniques to the Humboldt Slide controversy (off Eureka, CA; Figure I.2:3). To determine whether the features within the top 8 meters represent slope failure or are sediments waves.

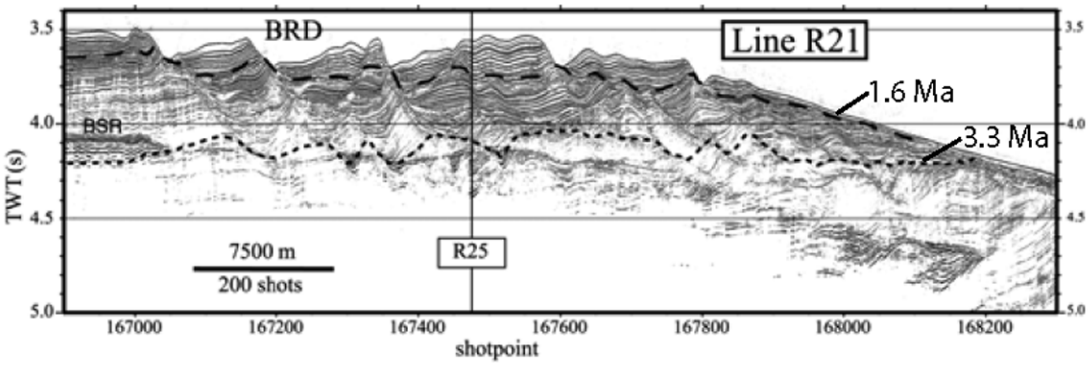

Figure I.1: Multi Channel Seismic line (MCS) across the Blake Ridge Depression (BRD) from (Holbrook et al., 2002). The bottom-simulating reflector (BSR) is absent within the BRD.

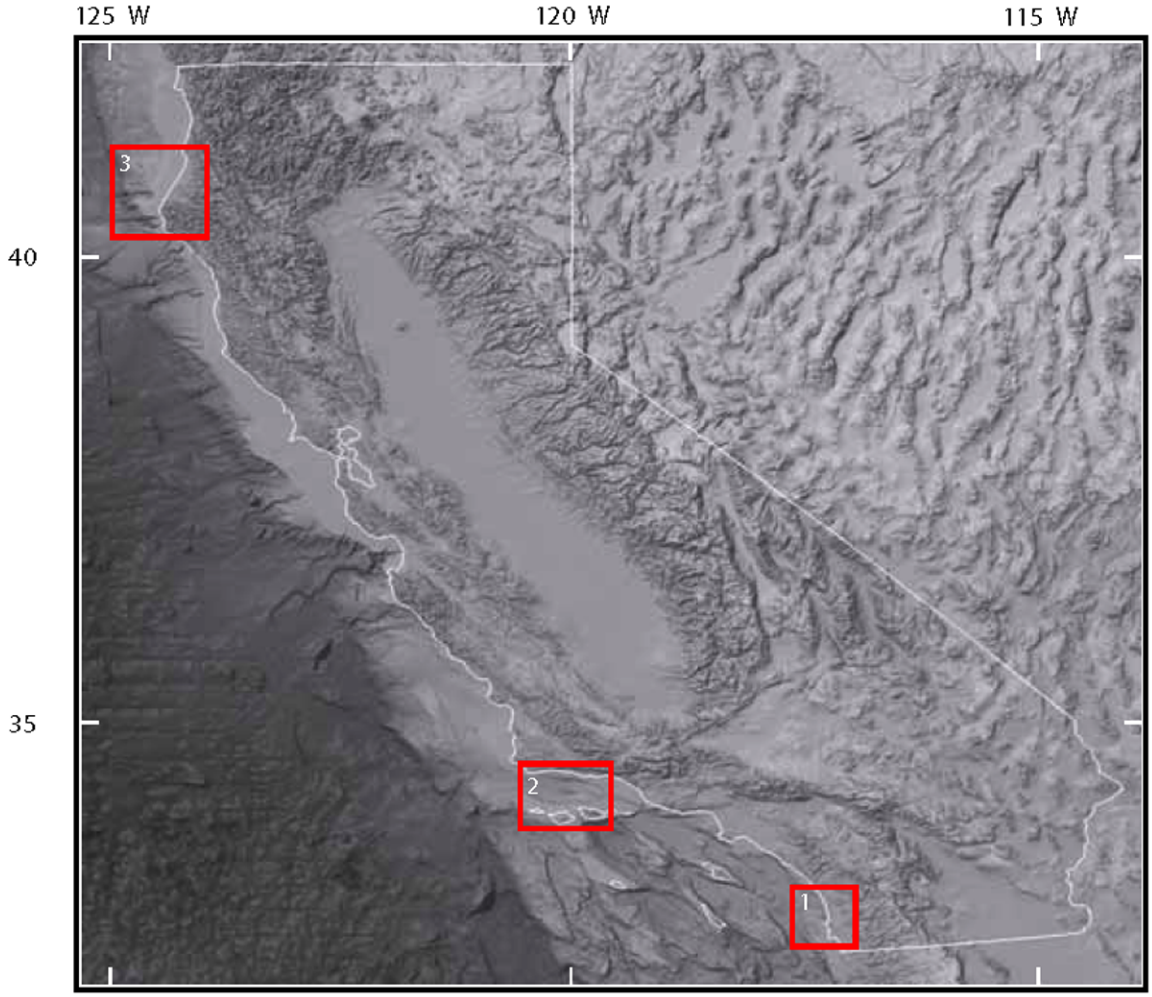

Figure I.2: Field sites for thesis chapters. 1) Ardath Shale, La Jolla, CA. 2) Santa Barbara Basin, CA. 3) Eel River Basin, CA.

Figure I.3: The study location in the Ardath Shale is located at the base of the cliff.

Figure I.4: The Hondo Platform is located next to the Gaviota Slide in the Santa Barbara Basin.

Figure I.5: The Eel River in flood stage. Photo by Jeff Borgeld, Humboldt State College.

Chapter II

Characterization of soft-sediment deformation: Detection of cryptoslumps using magnetic methods

Characterization of soft-sediment deformation: Detection of cryptoslumps using magnetic methods

Kurt Schwehr
Lisa Tauxe
Scripps Institution of Oceanography, University of California—San Diego, La Jolla, California 92093-0208, USA

ABSTRACT

Many workers have explored anisotropy of magnetic susceptibility (AMS) of sediments as an indicator of deformation. Several studies have used deflection of the eigenvector associated with the minimum in susceptibility, $\mathbf{V}_3$, as a criterion for deformation. We examine the AMS record of a well-exposed slump and find that although demonstrable deformation can occur without deflecting the $\mathbf{V}_3$ directions, an oblate AMS fabric is transformed into a triaxial fabric during initial deformation. Transformation of the fabric from oblate to triaxial appears to be highly correlated with an increase in natural remanent magnetization scatter, whereas deflection of the $\mathbf{V}_3$ axes is not. We suggest that subtle soft-sediment deformation can be detected by using AMS fabric.

Keywords: Ardath Shale, soft-sediment deformation, anisotropy of magnetic susceptibility, paleomagnetism.

INTRODUCTION

The magnetic fabric of geological materials, in particular of sediments, has been a focus of interest for decades (e.g., Ising, 1942; Granar, 1958; Rees, 1965). Given that it is extremely sensitive to strain, magnetic fabric has recently been used to detect subtle deformation of sediments and to distinguish geomagnetic features from deformational artifacts (e.g., Rosenbaum et al., 2000). Cronin et al. (2001) suggested that the anisotropy of magnetic susceptibility (AMS) could be used to detect slumps not otherwise obvious from the geologic field evidence (so-called cryptoslumps).

A range of laboratory experiments has been done on the depositional controls of magnetic fabric and its relationship to natural remanent magnetization (NRM; summarized in Tauxe, 1998.) In quiet-water conditions, there is a tendency for elongate particles to lie subparallel to the bedding plane. Because the magnetic susceptibility is usually at a maximum parallel to the long axis of particles, $\mathbf{V}_1$ will tend to be within the bedding plane. (Because many articles on AMS confuse eigenvalues and eigenvectors, referring to both as, e.g., k_{min}, we use the terminology of Tauxe [1998], whereby the eigenvectors are denoted by $\mathbf{V}$ and the eigenvalues as τ, τ_1 being the largest and τ_3 the smallest.) There is no preferred direction within the bedding plane, however, so $\mathbf{V}_2$ and $\mathbf{V}_1$ will be indistinguishable, as will the associated eigenvalues τ_2 and τ_1. Hence the magnetic fabric will be oblate with a vertical $\mathbf{V}_3$ direction.

In moderate water currents, especially on inclined bedding planes, particles may be slightly imbricated, resulting in slightly off-vertical $\mathbf{V}_3$ directions. Here we expect the fabric to be characterized by an oblate AMS ellipsoid, but the $\mathbf{V}_3$ direction will be antiparallel to the direction of paleocurrent. When deposition occurs under high current flow, with particles entrained, the $\mathbf{V}_1$ distribution is streaked, $\mathbf{V}_1$ is perpendicular to the flow direction (Jeffrey, 1922), and the fabric is characterized by prolate or triaxial ellipsoids.

What happens to the magnetic fabric during postdepositional deformation is more complex. Initial theoretical work on the relationship between magnetic fabrics and actual grain fabrics with respect to strain was done by Owens (1974), Hrouda and Hruskova (1990), and Housen et al. (1993). Most studies concerning strain in relation to AMS fabric have dealt with tectonic scales (e.g., Kanamatsu et al., 2001; Pares et al., 1999) and at least weakly metamorphosed rocks. However, as suggested by Rosenbaum et al. (2000) and Cronin et al. (2001), it appears that even minor amounts of soft-sediment deformation can have a profound effect on the paleomagnetic record. Such deformation, however, can be extremely difficult to detect on the basis of visual observations alone, hence the term cryptoslump. In this paper we pursue the idea that soft-sediment deformation can be detected through the use of AMS by investigating both cryptoslumped sediments from a marine environment along with the sediments from within and above the slump to try to confirm observations of Cronin et al. (2001). Our cryptoslump can be traced to a slumping event along the outcrop. Without the excellent exposure along the outcrop, however, its slumped nature would not be easily detected. Our goal is to develop a robust test for deformation based on the AMS characteristics of the slumped versus undeformed sediments.

GEOLOGIC SETTING

The Ardath Shale Formation of the La Jolla Group is part of a sequence of Eocene (49–46 Ma) rocks. The La Jolla Group was deposited within an ancient submarine channel and fan system that opened westward to the Pacific Ocean; it has since been uplifted to its present position (Kennedy, 1975; Chanpong, 1975). The Ardath Shale crops out along the base of an ~100-m-high sea cliff (Fig. 1) north of the pier at the Scripps Institution of Oceanography (La Jolla, California). Contained in the cliff are a number of cut-and-fill channel sequences that were likely sediment-transport conduits much like the Scripps Canyon head today. On the basis of data presented by May and Warme (1991), the paleocurrent direction is inferred to have been ~230°. Lohmar et al. (1979) used foraminifera to estimate a paleodepth of 200–600 m. This places the sedimentary environment of the Ardath Shale in the outer shelf or upper slope.

The Ardath Shale at the Scripps locality is mostly covered by modern beach sand, but extends 5 m above the beach in places. The lowest part of the exposed unit has well-defined horizontal laminations with no observed deformation. Above this, there is a 1-m-thick zone of soft-sediment deformation inferred to have been caused by slump-

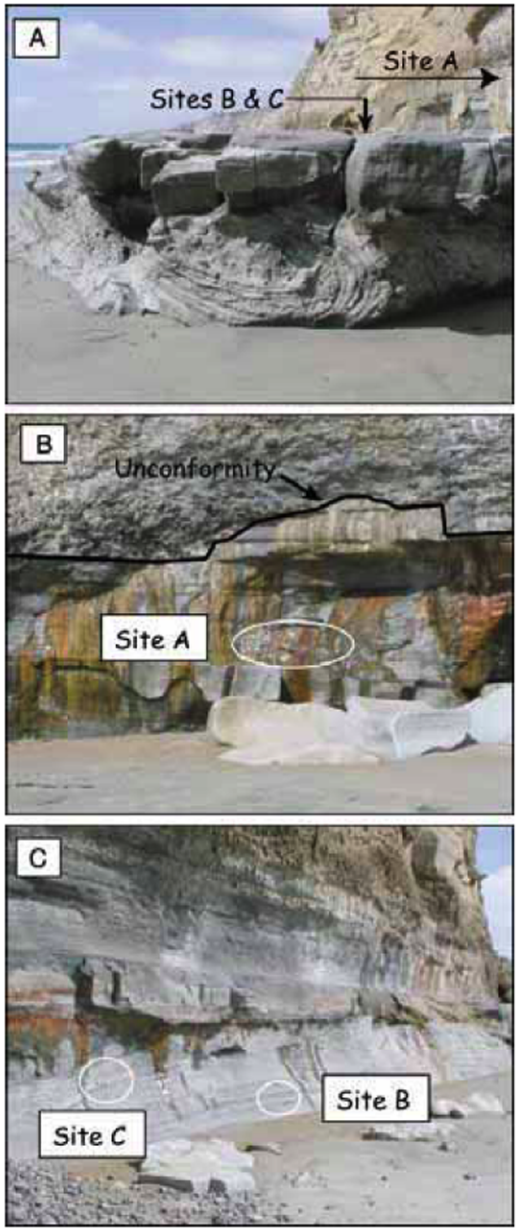

Figure 1. Photographs of slumped outcrop of Ardath Shale north of Scripps Pier at 32°52′05.6″N, 117°15′13.2″W. A: Prominent slump; view to north. B: Context of site A above slump; view to east. C: Context of sites B and C, within and below slump, respectively; view to east.

ing. There are overturned and recumbent folds as much as 1 m across (Fig. 1A). The overlying part of the Ardath Shale extends for another 2 m and is well laminated and apparently undisturbed. The top of the Ardath here is an erosional unconformity with an overlying conglomerate (Fig. 1B).

SAMPLING AND ANALYSIS

We sampled three sites within and surrounding a major slump in the Ardath Shale. The geologic context of the three sites is shown in Figure 1. Site A (Fig. 1B) is located 1 m above the slump in well-laminated and visually undeformed shale. Site B (Fig. 1C) is located 50 cm below the base of the slumped interval, and site C is located in the bottom 10 cm of the slump. The sampling site for site C is a less deformed region of the slump with bedding visibly deformed, but still within 10° of the bedding above and below the slump. Cores were drilled with a gasoline-powered drill and cut into nominal 1 inch (2.5 cm) specimens.

AMS Measurements

AMS measurements[1] were done at the Scripps Paleomagnetic Laboratory on a Kappabridge KLY-2 by using the 15 measurement scheme of Jelinek (1978). We calculated the best-fit tensor for each specimen by using Hext statistics (Hext, 1963; see also Tauxe, 1998). The directions of the eigenvectors for all specimens are shown in Figure 2A–2C. To assess the statistical distribution of these data, we used a variation of the bootstrap described by Constable and Tauxe (1990) and Tauxe (1998). The bootstrap eigenvectors for the data sets are shown in Figure 2D–2F, and the bootstrap eigenvalues are shown as histograms in Figure 2G–2I. The 95% confidence bounds for the minimum τ_3, intermediate τ_2, and maximum τ_1 eigenvalues are plotted above the each histogram.

In general, the eigenvectors associated with the minimum in magnetic susceptibility $\mathbf{V}_3$ are subvertical in all three sites. The intermediate and maximum susceptibility eigenvectors ($\mathbf{V}_2$ and $\mathbf{V}_1$, respectively) girdle the horizontal. The subtle differences in ellipsoid shape hold the key to our interpretation as to origin of the fabric.

The average eigenvector $\mathbf{V}_3$ for site A (Fig. 2A) is near vertical, but the distribution of the mean eigenvectors (Fig. 2D) shows that it is deflected an average of 12.7° toward 242.7°, in good agreement with the local paleocurrent indicators mentioned previously. The AMS (magnitude) ellipsoid is oblate, as indicated by the overlap of the 95% confidence bounds of τ_1 and τ_2 in Figure 2G.

The specimen (Fig. 2B) and the bootstrap eigenvectors (Fig. 2E) for site B both show that $\mathbf{V}_2$ and $\mathbf{V}_1$ are in two distinct groups. The histogram confidence intervals of eigenvalues (Fig. 2H) show that the intermediate and maximum axes are statistically distinct; therefore the ellipsoid is classified as a weak triaxial fabric. We conclude that this sediment has been deformed by the slumping of overlying sediments that occurred while they were still soft. Cronin et al. (2001) termed this kind of deformation "cryptoslumping."

The $\mathbf{V}_3$ directions from site C (Fig. 2C) are well grouped about the vertical. The $\mathbf{V}_1$ and $\mathbf{V}_2$ directions are also tightly grouped in the horizontal direction; $\mathbf{V}_1$ is oriented roughly perpendicular to the direction of inferred compression (east-west from the vergence of the slumps). The eigenvalues are distinctly triaxial (Fig. 2I).

Remanence Measurements

Measurements of the NRM of the specimens were made by using a three-axis CTF cryogenic magnetometer, located in a magnetically

[1]GSA Data Respository item 2003018, explanation of bootstrap method and raw AMS data, is available from Documents Secretary, GSA, P.O. Box 9140, Boulder, CO 80301-9140, editing@geosociety.org or at www.geosociety.org/pubs/ft2003.htm.

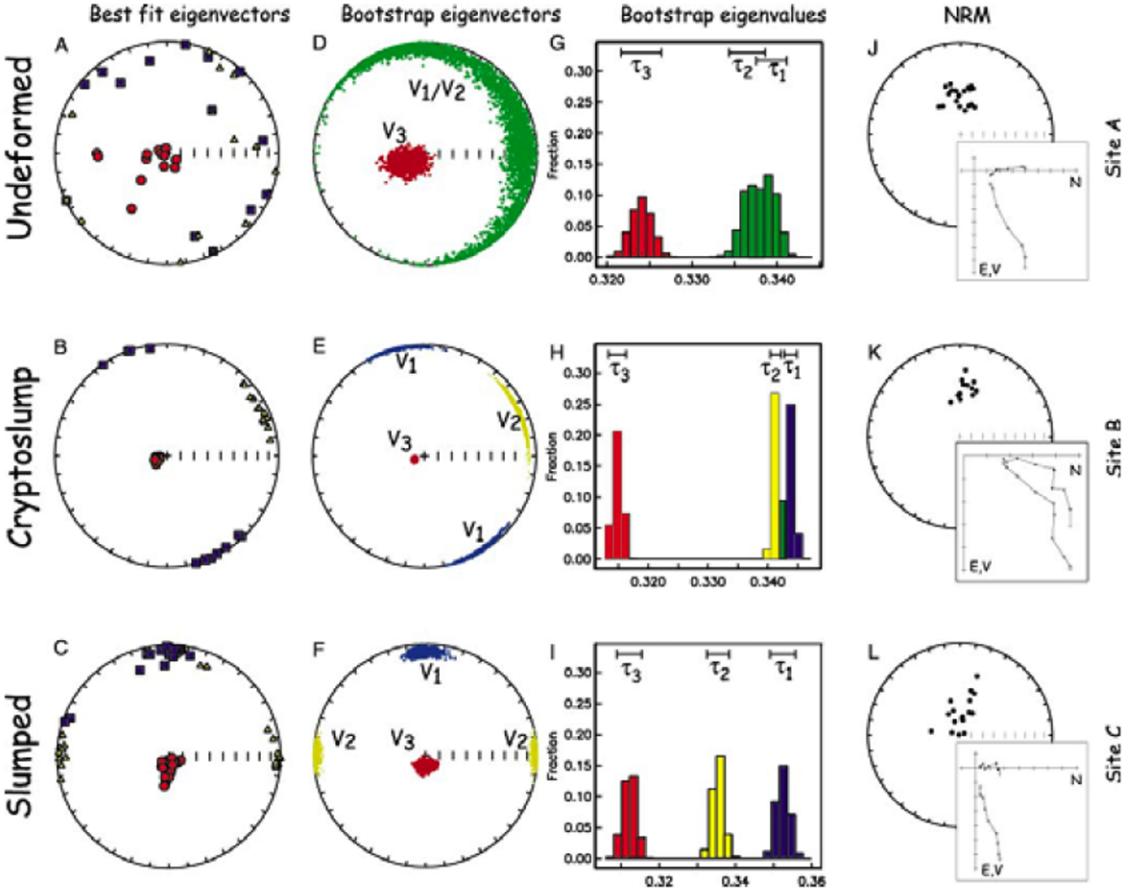

Figure 2. Anisotropy of magnetic susceptibility (AMS) and paleomagnetic data for three sites being studied. A–C: AMS eigenvector orientations. Squares are eigenvectors V_1 associated with maximum eigenvalues (τ_1). Triangles are eigenvectors V_2 associated with intermediate eigenvalues (τ_2), and circles are eigenvectors V_3 associated with minimum eigenvalues (τ_3). These are lower-hemisphere, equal-area projections for (A) site A (undeformed), (B) site B (cryptoslump), and (C) site C (slumped) specimens. D–F: Bootstrapped AMS eigenvector distributions (see text). G–I: Histograms of bootstrapped eigenvalues and 95% confidence bounds. Note that scales for histograms are different for each plot. J–L: Lower-hemisphere, equal-area projections of natural remanent magnetization (NRM) directions and representative vector–end-point diagrams for three sites.

shielded room. Alternating field (AF) demagnetizations were accomplished with an SI-4. NRM directions and representative vector–end-point diagrams for demagnetizations are shown in Figure 2J–2L. These samples were magnetically soft; measurements beyond 40 mT were highly scattered and are not shown. A typical Mr/Ms ratio for the Ardath Shale is 0.074.

TABLE 1. SUMMARY OF FISHER (1953) STATISTICS FOR NATURAL REMANENT MAGNETIZATION DIRECTIONS SHOWN IN FIGURE 2

Site	$\bar{D}$	$\bar{I}$	N	R	κ	α_{95}
Site A	0.0	54.9	22	21.54	45.3	4.7
Site B	6.0	46.4	12	11.81	57.5	5.8
Site C	1.9	70.3	18	17.22	21.8	7.6

Note: $\bar{D}$ is mean declination; $\bar{I}$ is mean inclination; N is number of specimens; R is length of resultant vector; κ is the Fisher (1953) precision parameter; and α_{95} is the estimate of the circle of 95% confidence.

The average NRM directions are summarized in Table 1. The average direction from the undeformed site (site A) is close to the expected direction for the Eocene at this locality (351.6° and 54.3°; Diehl et al., 1983). The site mean for the cryptoslump (site B) is significantly shallower than the undeformed site. That from the slump is on average steeper, but is much more scattered, with a κ of 21.8 as opposed to 45.3 for the undeformed site. Without further information, it would be tempting to interpret the data from the cryptoslump as genuine field behavior.

DISCUSSION AND CONCLUSIONS

AMS fabric is sensitive to strain even in small amounts on both regional and local scales. Such strain does not have to be visible for effects to be detectable in the AMS and NRM measurements. Several authors have devised tests for sediment deformation based on AMS fabric. Shor et al. (1984) used a strict test that discards all samples

with $f > 15°$, where f is the angular deviation of $\mathbf{V}_3$ from the pole to bedding defined in Crimes and Oldershaw (1967). Rosenbaum et al. (2000) developed a similar test that also relies on the $\mathbf{V}_3$ vector. They expect "good" samples to have a standard deviation of $\mathbf{V}_3$ inclination ($\sigma_{\mathbf{V}_3}$) of <6.5° and an inclination average of $\mathbf{V}_3$ ($I_{\mathbf{V}_3}$) of <6° from the vertical. Rosenbaum et al. (2000) found that for undisturbed sections, $\sigma_{\mathbf{V}_3}$ was <6.5° and the $I_{\mathbf{V}_3}$ was 84°. For our undisturbed site (site A), we calculated $\sigma_{\mathbf{V}_3}$ to be 18.3° and $I_{\mathbf{V}_3}$ to be 72.0°. For their deformed cores, Rosenbaum et al. (2000) calculated $\sigma_{\mathbf{V}_3}$ to be 26° and $I_{\mathbf{V}_3}$ to be 66.5°, whereas we found $\sigma_{\mathbf{V}_3}$ to be 5.0° and $I_{\mathbf{V}_3}$ to be 80.9° (site C). In short, we see a relationship that is opposite to that seen by Rosenbaum et al. (2000), whereby the disturbed intervals are actually more tightly grouped and more vertical than the undisturbed interval.

Although the method outlined in Rosenbaum et al. (2000) may be able to distinguish fluidized zones, it is perhaps not the best approach for several reasons. First, the mean inclination from a set having a near-vertical direction will always be biased too low (e.g., see Briden and Ward, 1966; Kono, 1980; McFadden and Reid, 1982). Second, eigenvectors are not independent, so the average minimum eigenvector should be estimated by using Hext (1963) statistics, not Fisher (1953) statistics. Furthermore, as discussed previously, there are many reasons why $\mathbf{V}_3$ could be deflected from the vertical other than postdepositional deformation. Finally, sediments can be severely deformed without deflecting $\mathbf{V}_3$ (see Fig. 2B–2C). The tests of Rosenbaum et al. (2000) and Shor et al. (1984) would not detect the deformation in sites B and C where $\mathbf{V}_3$ is near vertical. We propose that the eigenvalue test illustrated in Figure 2G–2I is much more sensitive to deformation than $\mathbf{V}_3$ deflection.

AMS fabric provides a way to distinguish between synsedimentary structures and subsequent deformation in situations where field observations are ambiguous. Many continental-slope regions show seismic signatures that have been interpreted as either retrogressive slope failure (Gardner et al., 1999) or as depositional features associated with hyperpycnal flows (N. Driscoll, 2000, personal commun.). The presence of a deformed sedimentary fabric would be strong evidence that a structure has undergone slumping.

ACKNOWLEDGMENTS

We thank M. Cronin, N. Driscoll, J. Gee, B.B. Radley, S.V. Raymond, P. Selkin, and J.P. Walsh for field assistance, comments, and discussion about this research. We thank B. Housen and J.M. Pares for their reviews. This research was partly supported by a grant from the National Science Foundation.

REFERENCES CITED

Briden, J.C., and Ward, M.A., 1966, Analysis of magnetic inclination in borecores: Pure and Applied Geophysics, v. 63, p. 133 152.

Chanpong, R.R., 1975, Depositional environment of the Ardath Shale [M.S. thesis]: San Diego, California, San Diego State University, 176 p.

Constable, C., and Tauxe, L., 1990, The bootstrap for magnetic susceptibility tensors: Journal of Geophysical Research, v. 95, p. 8383 8395.

Crimes, T.P., and Oldershaw, M.A., 1967, Palaeocurrent determinations by magnetic fabric measurements on the Cambrian rocks of Saint Tudwal's Peninsula, North Wales: Geological Journal, v. 5, p. 217 232.

Cronin, M., Tauxe, L., Constable, C., Selkin, P., and Pick, T., 2001, Noise in the quiet zone: Earth and Planetary Science Letters, v. 190, p. 13 30.

Diehl, J.F., Beck, M.E., Jr., Beske-Diehl, S., Jacobson, D., and Hearn, B.C., Jr., 1983, Paleomagnetism of the Late Cretaceous early Tertiary north-central Montana alkalic province: Journal of Geophysical Research, v. 88, p. 10,593 10,609.

Fisher, R.A., 1953, Dispersion on a sphere: Royal Society of London Proceedings, ser. A, v. 217, p. 295 305.

Gardner, J., Prior, D., and Field, M., 1999, Humboldt Slide A large shear-dominated retrogressive slope failure: Marine Geology, v. 154, p. 323 338.

Granar, L., 1958, Magnetic measurements on Swedish varved sediments: Arkiv for Geofysik, v. 3, p. 1 40.

Hext, G.R., 1963, The estimation of second-order tensors, with related tests and designs: Biometrika, v. 50, p. 353 357.

Housen, B.A., Richter, C., and van der Pluijm, B.A., 1993, Composite magnetic anisotropy fabrics: Experiments, numerical models, and implications for the quantification of rock fabrics: Tectonophysics, v. 220, p. 1 12.

Hrouda, F., and Hruskova, L., 1990, On the detection of weak strain parallel to the bedding by magnetic anisotropy: A mathematical model study: Studia Geophysica et Geodetica, v. 34, p. 327 341.

Ising, G., 1942, On the magnetic properties of varved clay: Arkiv For Matematik, Astronomi Och Fysik, v. 29, p. 1 37.

Jeffrey, G., 1922, The motion of ellipsoidal particles immersed in a viscous fluid: Royal Society of London Proceedings, ser. A., v. 102, p. 161 179.

Jelinek, V., 1978, Statistical processing of anisotropy of magnetic susceptibility measured on groups of specimens: Studia Geophysica et Geodetica, v. 22, p. 50 62.

Kanamatsu, T., Herrero-Ervera, E., and Taira, A., 2001, Magnetic fabrics of soft-sediment folded strata within a Neogene accretionary complex, the Miura group, central Japan: Earth and Planetary Science Letters, v. 187, p. 33 343.

Kennedy, M.P., 1975, Geology of the San Diego metropolitan area, California: California Division of Mines and Geology Bulletin, v. 200, 39 p.

Kono, M., 1980, Statistics of paleomagnetic inclination data: Journal of Geophysical Research, v. 85, p. 3879 3882.

Lohmar, J.M., May, J.A., Boyer, J.E., and Warme, J., 1979, Shelf edge deposits of the San Diego embayment, *in* Abbott, P.L., ed., Eocene depositional systems: Pacific Section, Society of Economic Paleontologists and Mineralogists, p. 15 27.

May, J.A., and Warme, J., 1991, Marine sedimentology of the early to middle Eocene La Jolla group, *in* Abbott, P.L., and May, J.A., eds., Eocene geological history, San Diego region: Pacific Section, Society of Economic Paleontologists and Mineralogists, Field Trip Guidebook, v. 68, p. 73 88.

McFadden, P.L., and Reid, A.B., 1982, Analysis of paleomagnetic inclination data: Royal Astronomical Society Geophysical Journal, v. 69, p. 307 319.

Owens, W.H., 1974, Mathematical model studies on factors affecting the magnetic anisotropy of deformed rocks: Tectonophysics, v. 24, p. 115 131.

Pares, J., van der Pluijm, B., and Dinares-Turell, J., 1999, Evolution of magnetic fabrics during incipient deformation of mudrocks (Pyrenes, northern Spain): Tectonophysics, v. 307, p. 1 14.

Rees, A.I., 1965, The use of anisotropy of magnetic susceptibility in the estimation of sedimentary fabric: Sedimentology, v. 4, p. 257 271.

Rosenbaum, J., Reynolds, R., Smoot, J., and Meyer, R., 2000, Anisotropy of magnetic susceptibility as a tool for recognizing core deformation: Reevaluation of the paleomagnetic record of Pleistocene sediments from drill hole OL-92, Owens Lake, California: Earth and Planetary Science Letters, v. 178, p. 415 424.

Shor, A.N., Kent, D.V., and Flood, R.D., 1984, Contourite or turbidite?: Magnetic fabric of fine-grained Quaternary sediments, Nova Scotia continental rise, *in* Stowe, D., and Piper, D., eds., Fine-grained sediments: Deep water processes and facies: Oxford, Blackwell Scientific Publications, p. 257 273.

Tauxe, L., 1998, Paleomagnetic principles and practice: Boston, Massachusetts, Kluwer Academic Publishers, 299 p.

Manuscript received 6 August 2002
Revised manuscript received 31 October 2002
Manuscript accepted 11 November 2002

Printed in USA

II.G Chapter Acknowledgment

Chapter 2, in full, is a reprint of the material as it appears in *Geology*, vol. 31, no. 3, p. 203-206, Characterization of soft-sediment deformation: Detection of cryptoslumps using magnetic methods, Schwehr, Kurt; Tauxe, Lisa; 2003.

I carried out all of the measurements used in the chapter, however the sampling of the cores was done by Matt Cronin, Peter Selkin, and Lisa Tauxe. Lisa Tauxe provided advice on the laboratory methods, data processing, and analysis. Tauxe also edited the paper in addition to teaching me how to use her PMAG software and the LaTeX document processing system. Neal Driscoll provided advice and discussion on interpretations of the paleoenvironment of the Ardath Shale.

Chapter III

Detecting Compaction Disequilibrium with Anisotropy of Magnetic Susceptibility

Detecting Compaction Disequilibrium with Anisotropy of Magnetic Susceptibility

Kurt Schwehr, Lisa Tauxe, Neal Driscoll

Scripps Institution of Oceanography, University of California, San Diego

Homa Lee

U.S. Geological Survey, Menlo Park, California

Abstract.
In clay-rich sediment, micro and macro structures influence how sediments deform when under stress. When lithology is fairly constant, anisotropy of magnetic susceptibility (AMS) can be a simple technique for measuring the relative consolidation state of sediment, which reflects the sediment burial history. AMS can reveal areas of high water content and apparent overconsolidation associated with unconformities where sediment overburden has been removed. Many other methods for testing consolidation and water content are destructive and invasive, whereas AMS provides a non-destructive means to focus on areas for additional geotechnical study. In zones where the magnetic minerals are undergoing diagenesis, AMS should not be used for detecting compaction state. By utilizing AMS in the Santa Barbara Basin, we were able to identify one clear unconformity, and eight zones of high water content in three cores. With the addition of susceptibility, anhysteretic remanent magnetization, and isothermal remanent magnetization rock magnetic techniques, we excluded 3 out of 11 zones from being compaction disequilibria. The AMS signals for these three zones are the result of diagenesis, coring deformation, and burrows. In addition, using AMS eigenvectors, we are able to accurately show the direction of maximum compression for the accumulation zone of the Gaviota Slide.

Introduction

Understanding and predicting when and where submarine landslides will occur is a still a challenge to the marine science community (e.g. *Kayen et al.* [1989], *Schlee and Robb* [1991], *Booth et al.* [1993], *Locat and Lee* [2002]). It is imperative to develop adequate techniques that allow insight into the pre- and post-failure stratigraphy.

Slope failure and creep may sometimes be imaged with multibeam and chirp data (e.g. *Edwards et al.* [1995], *O'Leary and Laine* [1996], *Eichhubl et al.* [2002], *Hill et al.* [2004]), but these techniques do not provide the full spectrum of information required to completely interpret these features. Layers with excess water create zones of weakness in the strata that may localize failure or slide surfaces (*Dugan and Flemings* [2000]), whereas unconformities may lead to apparent overconsolidation that record the past history of failures and erosion. *Mello and Karner* [1996] describe deviations from normal consolidation as compaction disequilibria. While many methods for exploring compaction disequilibria are destructive (*Lambe and Whitman* [1969]), anisotropy of magnetic susceptibility (AMS), the focus of this study, provides a minimally-invasive approach to quickly assess core sediments.

The ability to detect the two types of compaction disequilibria (underconsolidation and apparent overconsolidation) is another step in predicting the recurrence interval and size of submarine landslides that helps de-

termine the tsunamigenic potential of an area (*Driscoll et al.* [2000], *Ward* [2001]). Continental shelf and slope areas are becoming increasingly important for economic development of hydrocarbons, wave energy, and other resources. Slope stability is a critical engineering component to managing safe development.

In this paper, we will first discuss the types and causes of compaction disequilibria including high water zones that are underconsolidated and apparent overconsolidated zones associated with exhumation by landslides. We will then describe how AMS can be used to identify compaction disequilibria. Finally, we will apply AMS techniques to the Santa Barbara Basin margin, a region with known slope instabilities (e.g. *Fisher et al.* [2005]).

Compaction disequilibria

Underconsolidation

Bulk permeability of sediment is determined by a combination of local micro-structure, grain permeability and the degree of macro-scale permeability determined by material continuity. In Figure 1a, we show a schematic drawing of sediment undergoing consolidation. Clay particles tend to have positively charged edges and negatively charged faces. These electrostatic forces tend to cause clay particles to aggregate edge to face (EF) (*Bennett et al.* [1991]) as shown in the upper part of Figure 1. During consolidation, volume loss results in the collapse of the clay structure to the more compact face to face (FF) structure.

Overpressured zones are likely to occur in areas with high rates of sedimentation because the rate of pore fluid escape cannot keep pace with the accumulating overburden (*Mello and Karner* [1996]). Differences in permiability associated with small changes in consoldation, mineralogy, and bioturbation may retard upward migration of fluids. Zones of excess water content can develop below such layers. These high water content zones could inhibit the normal consolidation of the clay depositional structure, thus keeping the EF clay contacts from changing into FF contacts (Figure 1a). Under load, these open structures collapse to a stable book structure that can not re-inflate. This inability to re-inflate with increasing pore pressure implies that undercompacted horizons are primary depositional features created as the overlying layer is deposited.

Apparent overconsolidation

Overconsolidation is a reduction in the water content producing an apparent disequilibrium, where material is more consolidated than predicted for a given depth according to empirical compaction-loading curves. One factor leading to apparent overconsolidation is the existence of erosional unconformities. First, sediments are deposited and buried in an unperturbed compaction scenario. If overlying sediments are removed by slope failure or erosion, and the underlying material has undergone some component of inelastic deformation (as is the case for clays), then that inelastic strain will remain, resulting in an apparently overconsolidated zone.

Shock induced dewatering can also cause overconsolidation (*Lee et al.* [2004]). *Locat and Lee* [2002] summarized work showing that with repeated shake events, sediments that do not fail may lose water, compact, and become stronger. They term such events "seismic strengthening."

Magnetic fabrics

AMS is a well-established technique for studying fabrics of geologic materials (summarized in *Tarling and Hrouda* [1993] and *Tauxe* [1998]). AMS of clay-rich sediments is believed to be dominated by paramagnetic shape anisotropy of the clay minerals and small magnetic particles that are generally attached to the clay fabric (*Kodama and Sun* [1992]). When hemipelagic sediments are deposited in quiescent environments, elongate particles deposit with their long axes subparallel to the bedding plane. This mode of deposition produces weakly oblate to isotropic sediment fabrics.

Detection of underconsildation and unconformities is possible with non-magnetic techniques. However, the AMS magnetic fabric method complements the other data types and, more importantly, helps identify compaction disequilibria features when they are difficult to detect by other approaches. Other magnetic fabric methods include anisotropy of isothermal remanent magnetization (AIRM) and anisotropy of anhysteretic remanent magnetization (AARM) (*McCabe et al.* [1985]). Unlike AIRM and AARM, AMS is magnetically non-destructive (it does not affect the magnetic remanence) and is the fastest of the magnetic techniques to apply. AIRM and AARM both would yield additional insight into sediment deposition and deformation mechanisms, but are more time consuming to acquire. Moreover, AMS is strongly affected by the clay fabric, whereas remanent anisotropies are not directly

sensitive to the clays and it is the clay fabric that is of concern here.

Because AMS is sensitive to the compaction state of clay-rich sediments (e.g. *Housen et al.* [1996], *Kopf and Berhman* [1997], and *Kawamura and Ogawa* [2004]), it is a promising tool for exploring regions of rapid sediment loading. Accelerated deposition and sediment loading tend to lead to a higher occurrence of slope failures, because rapid sedimentation usually is associated with higher water content (*Schwab et al.* [1993]). The majority of compaction and dewatering occurs typically from the sediment-water interface down through the top 10's of meters of sediments, with the majority being completed by depths of around 150 meters (*Kawamura and Ogawa* [2004]). When loaded, clay sediments compact and compaction signatures can be observed with AMS measurements as an increasing oblate anisotropy with the V_3 direction (eigenvector associated with the minimum eigenvalue using the terminology of *Tauxe* [1998]) being near vertical. At depth, processes such as cementation and diagenesis begin to lock in the shape that is present and all of the "easy" compaction has been accomplished.

For deep-sea sediments, *Kawamura and Ogawa* [2004] found that the compaction process progresses in either a gradual manner, or a stepwise function. *Kawamura and Ogawa* [2004] suggest that low permeability in overlying layers that retard dewatering may lead to regions of excess pore pressure as evidenced by large void ratios. In rapidly depositing sediments, the degree of compaction should allow AMS to detect these underconsolidation zones.

According to *Kawamura and Ogawa* [2004], sedimentation rates have an influence on compaction, where water content remains higher to greater depths for faster sedimentation rates. The deep ocean cores used by *Kawamura and Ogawa* [2004] have sedimentation rates of 1.7 to 3.3 mm/kyr. Slow sedimentation rates allow pore fluids more time to diffuse through low-permeability layers. The conditions of faster rates found along continental margins preserve disequilibria to greater depths because there is less time for fluids to be expelled from the sediment column.

The AMS signature for apparent overconsolidation would be an abrupt increase in the degree of anisotropy of the fabric. The AMS signature predicted for overconsolidation is illustrated in Figure 1b. The overall anisotropy is defined as the difference between the eigenvalues τ_i (which are scaled to sum to unity with the maximum being τ_1 and minimum being τ_3). Changes in the degree of anisotropy under normal consolidation would be a gradual increase in anisotropy as shown in the top of the core. An abrupt change to an FF fabric because of overconsolidation would be accompanied by an abrupt increase in the degree of anisotropy reflected by the increase in the the separation of τ_1 and τ_3 (see Figure 1). Note that the relationship of τ_2 to the others (not shown) reflects the shape; where τ_2 is indistinguishable from τ_1, the shape is oblate. In contrast to overconsolidation, underconsolidation zones would be reflected by a decrease in degree of anisotropy as illustrated in Figure 1a.

If AMS is able to detect these zones of overcompaction (compared to the expected sediment overburden and time), then it could provide a quick method to detect regions where the overlying sediment has been removed. To test the AMS method for detection of compaction disequilibria, we need a well-studied area with a high deposition rate and reasonably well-defined failure history. The Santa Barbara Basin and the Gaviota Slide provide such an environment.

Geologic Setting

The Santa Barbara Basin (SBB) is located off the coast of Southern California (Figure 2) and is the northern-most basin in the California Borderland area. The basin is roughly 80 km by 32 km at its greatest extent. The northern end of the basin is blocked by the Santa Barbara coastline; the San Miguel, Santa Rosa, and Santa Cruz Islands delineate the southern extent of the basin. On the western side, the basin has a sill depth on the order of 460 m (located at approximately 120° 28' 27.06" W, 34.0° 15' 52.01" N) whereas on the eastern edge of the basin, the sill is shallower, being approximately 225 m. The maximum depth of the enclosed basin is 593 m (120° 01' 15.60" W, 34° 12' 19.44" N). The sills on the western and eastern boundaries inhibit the flushing of the bottom waters creating an anoxic basin. Typically, there are low oxygen concentrations starting at 470 m and the water column is depleted of oxygen by 570 m (*Edwards et al.* [1995]).

The sediment accumulation rates in the SBB are extremely high and have been estimated to be on the order of 1400 mm/kyr (*Hendy and Kennett* [2000]). The currents and sediment production in this particular region have been extensively studied (e.g. *Soutar and Crill* [1977], *Reimers et al.* [1990], *Bray et al.* [1999], *Dorman and Winant* [2000], *Oey et al.* [2004], *Warrick et al.* [2005]). During the winter months, sediment input is dominated by terrigenous input that corresponds to winter precipitation and erosion that occurs in Cal-

ifornia. At Ocean Drilling Project (ODP) site 893, the dominant terrigenous sources are the Santa Clara and Ventura Rivers (*Marsaglia et al.* [1995] and *Hein and Dowling* [2001]). The northern slope area of the SBB is more likely to have the terrigenous sediment sourced from the Santa Ynez Mountains. Spring months experience high biogenic productivity that is dominated by diatoms (*Thunell et al.* [1995]). The productivity is probably driven by upwelling of nutrient-rich waters.

The area around the SBB (Figure 2) is a tectonically active zone with frequent large earthquakes up to magnitude 7 (*Shaw and Suppe* [1994]). The SBB has a large number of slope failure features, which could have been triggered by local earthquakes.

The study area is the northern slope of the SBB bounded by the shelf break to the north, the basin floor to the south, the Goleta Slide to the east and the Conception Fan to the west. The Conception Fan appears to be inactive (*Fischer* [1998]).

The swath bathymetry (Figure 3) was collected by the Monterey Bay Aquarium Research Institute (MBARI) using a 30 kHz EM300 multibeam system (*Eichhubl et al.* [2002]). The soundings were gridded at 25 m cell spacing. The MBARI bathymetry gives an excellent view of the features in the basin that are on the scale of meters and larger (Figure 3).

Goleta

The most prominent deformation feature observed in the SBB is the large Goleta Slide on the northeastern corner of the basin. The aerial distribution of this large feature is 11 by 14 km with three main areas of runout. The center runout has the highest topography, whereas the western runout has the lowest with a difference of about 50 m. The head scarps are located at the edge of the shelf-slope break and are steep with heights up to 50 m that transition into a number of blocks with large amounts of drape. The toes of the slides extend out into the basin 9-12 km, reaching to within 970 m of ODP site 893 (see Table 1 for location).

Gaviota

The Gaviota Slide (Figure 3) is located to the west of the Goleta Slide and extends 3 km from the head scarp down to the bottom of the toe. The evacuation zone appears to have removed 6-8 meters of material (relief measured at the head scarp). The Gaviota Slide is a very recent feature as evidenced by the minimal pelagic drape mantling the slide scar. The slope break above the Gaviota head scarp is 100 meters below sea level (mbsl). The slope dips on average 3.6° down to the basin floor at 480 meters where the dip of the sea floor diminishes to about 0.5°. *Edwards et al.* [1995] estimated that the slide excavated 0.01-0.02 km^2 of sediment failing in two main stages. They report the details of the slide morphology and an event chronology.

It is likely that the December 21, 1812 earthquake (estimated $M_w \approx 7.2$) triggered the Gaviota Slide (*Borrero et al.* [2001]). *Borrero et al.* [2001] cite historical reports of a small tsunami observed along the coast just after the quake. *Edwards et al.* [1995] believe that the Gaviota Slide failed somewhere in the range of 1345 CE to 1871 CE with a best estimate of 1812 CE. The excavated scarp is covered by pelagic drape, which would constrain the age of the slide. However, these types of unconformities can be difficult to recognize in cores, especially after the horizons oxidize. Because of the contrast in the degree of compaction across the unconformity, it is possible that AMS fabric could be used to detect the unconformity.

Other small slides

The main difference between the smaller slide structures in the basin compared to the Goleta Slide is that the smaller slides have much less runout. There are three areas, or groups, of small slides: the northeastern side of the basin, the very steep slides on the southern wall (not studied in this paper), and the Gaviota Slide on the northern side of the basin. There are undoubtedly a large number of smaller slides that are below the resolution of the EM300 multibeam system available at the time of the study.

Two small slides on the northeastern corner of the basin lay between the Goleta Slide and the end of surface expression of the Mid-Channel trend anticline structure. These slides are on a shallow dipping slope and have well-defined head scarps. The slide just to the east of the Goleta has an evacuated zone at the top that is 0.6 km long with a slope of 1.4°, whereas the toe runs for 1.6 km on a slope of 1.2° with a maximum width of 0.97 km. The slide to the east has a double-humped slide scar and is difficult to see in the bathymetry. This structure has an overall slope of 1.4° and an total extent of 2.9 km from the headwall scarp to bottom of the toe.

On the western edge of the basin is a very subtle slide centered at 120° 18' 37.80" W, 34° 16' 24.06" N described by *Edwards et al.* [1995]. The upper deformed section of the slide is 4 km long and dips an average of 0.9°, whereas the lower surface is smooth and extends about 2.4 km at a slope of 0.6°. The material was able to fail at a slope of just 1°, that may be very similar

to the low-angle slide that *Field et al.* [1982] describe near the Klamath River, CA. It is possible that there was a wide spread underconsolidation zone or clay-rich layer that allowed for easier mechanical failure during an earthquake event.

Crack

A large crack (Figure 3) is evidence of recent deformation on the northern side of the basin. This crack extends 8 km, trending East-West between the Goleta and Gaviota slides from 120° 00' 17.55" W, 34° 22' 28.92" N at a depth of 355 meters on the east to 394 meters on the west at 120° 05' 34.75" W, 34° 22' 22.67" N. The slope across the crack ranges from 4.9° to 5.5°. The crack continues from the western edge of the Gaviota Slide another 2.4 km before dying out where the slope diminishes to 3.9°. The crack is less defined along its eastern extent and is overprinted by larger rills that exhibit up to 5 meters of relief. These rill features appear similar to those described by *Spinelli and Field* [2001] north of the Humboldt amphitheater in northern California.

Methods and Results

CHIRP Seismic data

Seismic lines covering the northern slope of the SBB were collected during August 2004 using the Scripps Institution of Oceanography subbottom unit (Figures 4 and 5). The CHIRP seismic system (*Schock et al.* [1989]) is a modified EdgeTech Xstar system with an ADSL link from the fish to the topside computers. The data were collected with a 50 ms sweep from 1 to 6 kHz. The Xstar SEG-Y records were processed with segy-py and SIOSEIS (*Henkart* [2005]), and were plotted with pltsegy. (The segy-py software is available from the authors upon request.)

Coring

Cores were acquired with the Scripps Institution of Oceanography "King Kong" gravity coring device using clear plastic core liner with an inner diameter of 8.26 cm. The core head was loaded with 136 kg and deployed at 30 m/minute into the sea floor. Table 1 summarizes the three cores collected for this study and the nearby ODP Site 893 (See Figure 2).

Biogenic gas could potentially disturb the fabric of the cores as they are brought up from depth. By using clear core liner, we were able to observe the sediment-water interface and overlying water clarity as soon as it was removed from the core barrel. On deck, we observed excellent preservation of the sediment-water interface complete with hummocky bioturbated sediments. We observed no evidence of deformation as a result of gas expulsion.

All cores were split, described, photographed, and x-rayed. Cores were then sampled with 8 cm^3 paleomagnetic cubes as densely as practical with a typical spacing of 3 cm. The 8 cm^3 specimens were weighed wet, dried by cooking at 50° C, and then weighed dry to determine weight percent water.

Core 1 (Figures 4 and 6) was collected from the accumulation zone of the Gaviota Slide at a water depth of 480 meters. The sediment was initially deposited in the oxygenated zone where bioturbators could potentially disturb depositional layering. The sediment was then transported by slope failure to the top of the low-oxygen zone. The top 20 cm of the core was disturbed (photo Figure 6) during transport and splitting. The feature at 40 cm is a section boundary. The rest of the core shows faint sediment layers with some mottling. The core is a dark gray color (Munsell 5Y/3/2).

Core 2 (Figures 4 and 7) was acquired in the evacuation zone of the Gaviota Slide. There is a very thin disturbed zone at the core top (< 7 cm) and a thin zone at 10 cm where the core was disturbed during splitting. There is a wavy surface at ~27 cm that we interpret to be an unconformity separating the sediments exhumed by the slide below from the more recent pelagic drape above. The pre-slide layer may be capped by a thin veneer of slide rubble. On the basis of the height of the head wall (Figure 4), it appears that the material below the slide scar had been buried to a depth of 6 to 10 meters before being exhumed. Below this unconformity, the sediment exhibits a marked increase in induration. Occasional burrows are observed, but the core is generally a monotonous gray sediment.

Core 4 (Figures 5 and 8) was collected above the crack to assess if deformation was occurring upslope. This 125 cm core is generally homogeneous in texture and color (dark gray). Slight core splitting disturbance is observed down to ~13 cm. The top 35 cm of sediments have a water-saturated, dark appearance and the bottom 25 cm have a slightly lighter color. There are a few zones that exhibit laminations (40-50 cm, 58 cm, 80-82 cm) and from 15 to 25 cm there are well preserved burrows (Figure 8). There are a few shells and shell fragments in the 18-22 cm interval and at 62 cm. This core was acquired in an area with continuous seismic reflectors that suggest little to no evidence for internal deformation (Figure 5).

Remanence Measurements

Magnetic remanence measurements were performed at the Scripps Paleomagnetic Laboratory using 3-axis CTF and 2-G cryogenic magnetometers. Alternating Field (AF) demagnetization was accomplished using a Sapphire Instruments SI-4 in steps up to 40-180 mT depending on the particular specimen's demagnetization curve. Specimens were demagnetized along all three axes with Z being last. Double or triple demagnetizations were not used. Representative Zijderveld diagrams are shown in Figure 9.

There are two styles of demagnetization behavior. The first (Figure 9: Core 4 - 012 cm) is characterized by smooth decay to the origin with median destructive fields (MDF) of around 30 mT. The second is characterized by low MDF values (~10 mT) and a tendency to deviate from the origin, behavior often associated with greigite (Fe_3S_4; *Snowball* [1997], *Hu et al.* [1998]; Figure 9: Core 4 - 063 and 108 cm). The "greigite" signal is characterized by a gyroremanent magnetization (GRM) which is defined as the magnetization acquired during AF that is perpendicular to the applied AF field (*Stephenson* [1993]).

We plot MDF values for the cores in Figures 6-8 in column b. Also shown in Figure 6 and 8 are regions with the "greigite"-like behavior. Core 2 (Figure 7) has no "greigite" signal in the AF demagnetization curves. For comparison, an example of AF demagnetization of a greigite sample (identified with xray-defraction; *Hu et al.* [1998]) is shown in Figure 9: Greigite.

Principle component analysis (PCA) was applied to the set of AF demagnetization vectors for each specimen to generate best fit directions (*Kirschvink* [1980]). Fisher statistics (*Fisher* [1953]) were used to calculate an overall best fit declination for each core. These directions were used to orient all cores ($\bar{D}$, Table 3).

AMS

Specimens were measured on a Kappabridge KLY-2 magnetic susceptometer, using the 15 position scheme of *Jelinek* [1978]. Eigenparameters were calculated using Hext statistics (*Hext* [1963]) with PMAG-1.7 (software available at $http://sorcerer.ucsd.edu/software/$; *Tauxe* [1998]; *Tauxe* [2005]). We followed the convention of *Tauxe* [1998] by referring to eigenvalues as $\tau_{1...3}$, with τ_1 being the largest and τ_3 being the smallest, and the associated eigenvectors as V_1-V_3. Eigenvalues are normalized such that they sum to unity.

In all cores, there is a general increase in anisotropy with depth (measured by the difference between τ_1 and τ_3). The overall trends are interrupted by brief intervals (labeled in Figures 6-8) of decreased anisotropy. Some of these zones appear to be related to core processing disturbances, unconformities or other sedimentological features (e.g. burrows and shell zones). These are labeled with letters in Figures 6-8. Others are not clearly sedimentological in origin. These are numbered in Figures 6-8. These numbered features could be compaction disequilibrium. We will return to this topic later.

Eigenvectors for these cores are plotted in Figure 10 after being oriented assuming the average declinations are approximately North. Also shown are the bootstrapped mean eigenvectors (*Constable and Tauxe* [1990]) which show the mean contour enclosing the 95% confidence bounds. All of these cores show vertical V_3 directions (associated with the minimum eigenvalues and plotted as red circles) as expected in sedimentary environments. Cores 2 and 4 show the oblate fabric with no preferred alignment of V_1, typical of quiet water deposition. Core 1 shows a significant alignment of V_1 in the NW-SE direction, suggesting poste-depositional compression. The compressional direction predicted from bathymetry (Figure 3) is shown as arrow "a" in Figure 10. The preferred orientation from the AMS data is consistent with the 95% confidence level for compression along the axis (labeled "b" in Figure 10).

χ_{lf}, ARM, and IRM

To help constrain the origin of the AMS signatures, we measured low field bulk susceptibility (χ_{lf}), ARM, and IRM. ARM acquisition was accomplished with a SI-4 using a 100 mT alternating field and a 40μT bias field. IRM's were imparted with an ASC impulse magnetizer with a field of 1 tesla. Mass normalized data used the dry specimen mass after drying at 50° C.

King et al. [1983] suggested that different slopes on a bi-plot of χ_{lf} and susceptibility of ARM can show different magnetic grain size fractions. In Figure 11, we plot ARM and IRM against χ_{lf}. These plots show two end members (Group 1 plotted in red pluses and Group 2 as blue stars). According to *King et al.* [1983], the red end member would have smaller grain size compared to the blue end member. Features within either end member are more likely to be caused by fabric, whereas features transitional between the two could well be diagenetic in origin or represent a mixture of the end members.

We plot χ_{lf} and IRM in Figures 6-8 columns c and d respectively. We have not plotted ARM because it is similar to the IRM behavior. Group 1, with high IRM and χ_{lf} values are at the tops of all three cores. The transition to Group 2 with lower IRM and χlf is defined

by the break in slope after the rapid decrease in IRM (marked with a dashed line in Figures 6-8).

Hysteresis parameters

To constrain the magnetic composition of the material in the cores, we measured hysteresis loops for a subset of the specimens (Figure 12) using a MicroMag alternating gradient force magnetometer (AGFM). The high field susceptibility (χ_{hf}) is dominated by the paramagnetic grains, while the low field bulk susceptibility (χ_{lf}), (derived from the Kappabridge measurements) is a combination of ferro-magnetic and paramagnetic grains. The χ_{hf}/χ_{lf} ratio gives a rough estimate of the fraction of paramagnetic and ferro-magnetic grains contributing to the low field magnetic susceptibility measurements (hence the AMS). The χ_{hf}/χ_{lf} ratios are all below unity indicating that susceptibility is most strongly controlled by the high field, or paramagnetic, susceptibility (Table 2). The paramagnetic susceptibility is, in turn, largely controlled by the clays. Hence, to a first order, the AMS signal reflects clay fabric in these sediments.

The specimens plot in the "multi-domain" and "vortex" remanent state region of the graph (Figure 12) based on the magnetic simulations of *Tauxe et al.* [2002]. These results predict that the magnetite grains should be about 115-120 nm in width and somewhat elongate. The two specimens labelled 4-081 and 4-120 are from the "greigite zone" in core 4, hence cannot be easily interpreted in terms of micromagnetic modeling of magnetite. As expected from the bi-plots, the Group 1 specimens appear to be finer grained than these in Group 2.

From the foregoing, the numbered zones in Figures 6-8 do not appear to be related to changes in composition or to visible disturbance of the cores. It is possible that these zones reflect compaction disequilibria. As hypothesized, such disequilibria would be reflected in the relative water content of the sediment. To investigate further, we measured water content in the cores.

Water content

Specmens were weighed after sampling and then dried to calculate an approximate weight percent water. To look for anomalous water content, the weight percent water data were fit with an exponential curve (*Dugan and Flemings* [2000]) using a nonlinear least-squares (NLLS) Marquardt-Levenberg algorithm. Fitting an exponential is not appropriate for core 2 because there is a clear discontinuity at approximately 27 cm and the core length is not long enough to yield the required number of measurements for a stable fit. We split the fit into two sections at the unconformity and a best fit was approximated.

We coregistered the AMS fabric with the deviation from the exponential fit to determine zones of interest. Lettered zones are reserved for regions that we are confident are caused by diagenesis (core 1), coring deformation (core 2), or bioturbation and burrows (core 4). Locations in the core that show both a decrease in anisotropy and an increase in water content have been numbered from 1 to n going down core.

Discussion

If sediments are homogeneous, they will compact progressively with depth accompanied by a gradual loss of fluid. It is rare for sediment on the continental slope to be completely homogeneous because there are almost always variations in permeabilities, densities, etc. The dominant internal causes of differences arise from changes in lithology, clay fabric, and bioturbation. Processes such as dissolution of grains, precipitation of cements, and grain breaking are unlikely to be important factors when considering young near surface sediments.

In the cores, there are general trends in compaction as reflected by an overall increase in anisotropy down core. The trends are not uniform, but are punctuated by a large transformation associated with the Group 1/2 transition and smaller features associated with visible deformation (lettered zones) and excess water content zones (numbered zones). We will address each of these features in turn in the following section.

Group 1/2 transition

The Group 1/2 transition is indicated by a dashed line in Figures 6-8. This horizon corresponds to an increase in the degree of anisotropy (column a) in all cores with Group 2 specimens having higher anisotropy than Group 1 specimens. All of the numbered zones of decreased anisotropy are within Group 2 and do not appear to be associated with changes in magnetic mineralogy.

The transition in core 2 is associated with the largest jump in anisotropy of any core. Moreover, in this core the Group 2 average anisotropy is the highest of any core. Starting at 23 cm below sea floor, core 2 has a total anisotropy that increases much faster than observed in the other two cores. The transition to a larger total anisotropy occurs from 23 to 33 cm where anisotropy plateaus to a large relatively constant value.

Core 2 was taken from the evacuation zone above the Gaviota Slide (Figure 3). The transition region shows visible evidence of deformation (Figure 7: core photo) with watery, weak material inter-fingering with highly indurated sediments. We interpret this abrupt shift as the transition from young unconsolidated drape, down through a thin veneer of slide rubble overlying the slide surface. The material beneath the slide scar apparently was buried 6-8 meters before the slide occurred. At that depth the consolidation curve had progressed to the point where there is little change with additional loading. Therefore the degree of anisotropy appears essentially constant over short depth intervals.

Our best estimate for the unconformity is at approximately 23 cm. Assuming sediment accumulation rates ranging from 0.8 m/kyr (*Marks et al.* [1980]) to 1.4 m/kyr (*Duncan et al.* [1971]), consistent with rates derived by *Eichhubl et al.* [2002], we estimate the age of the slide to be between 1715 to 1840 CE, which brackets the 1812 Santa Barbara earthquake.

The transitions in cores 1 and 4 are quite different from that observed in core 2. In these cores, the transition between groups 1 and 2 is not associated with a physical discontinuity. Rather, the transition appears to be a diagenetic front.

A large number of studies have found high χ_{lf}, ARM, and IRM in surficial sediments that shift to lower values between 0.2 to 10 m depth from around the world. For example, *Geiss et al.* [2004] and *Pan et al.* [2005] describe such transitions in lacustrine sediments; *Kumar et al.* [2005] in the eastern Arabian Sea; *Tarduno* [1994] and *Rowan and Roberts* [2006] in the Pacific; *Karlin* [1990], *Liu et al.* [2004] and *Riedinger et al.* [2005] on continental margins; and *Leslie et al.* [1990b] focus on the California Borderland in basins just to the south and east of the Santa Barbara Basin. In these studies, χ_{lf}, ARM, and IRM shift together, however, χ_{lf} often does not decay until slightly farther down core.

There are a number of postulated causes for these observed shifts: 1) changes in sediment supply (possibly on glacial time scales), 2) changes in production and destruction of biogenic magnetite, or 3) pore-water chemistry and biogenic activity that consume a fraction of the magnetic grains.

Pore-water chemistry driving the change is the most likely scenario and is the model favored by *Leslie et al.* [1990b]. The process (detailed in *Leslie et al.* [1990a]) is driven by changes from an oxic environment at the sediment-water interface where sediments go to anoxic conditions as they are buried. This process preferentially consumes the smallest magnetite grains, as magnetite is transformed into iron sulfides. *Karlin* [1990] concluded that magnetic mineral diagenesis is likely to occur in rapidly deposited, sulfidic sediments. Based on the AF demagnetization curves, we suspect that a minor amount of greigite may have formed in the base of cores 1 and 4, well below the transition from Group 1 to 2 (Figure 9). Therefore we interpret the Group 1/2 transition in cores 1 and 4 to be caused by a loss of fine grained magnetite with small amounts of iron sulfide production occurring deeper down.

The implications for magnetic anisotropy through diagenesis have not been explored in detail in previous studies. Here we find that the finer grained magnetite (Group 1) is likely to be carrying a nearly isotropic fabric. The larger magnetic grains (Group 2) and the paramagnetic minerals carry a fabric that tends to follow the compaction and deformation of the bulk sediment.

Group 2 sediments

Below the dashed line in all cores (in the Group 2 layers) are several zones of decreased anisotropy, accompanied by increased water content (labeled as zones 1-4). These zones have a relatively lower anisotropy, and relatively higher water content than the surrounding sediments (as illustrated by Figure 1a in the zone of excess water content). These zones could be caused by either compaction disequilibria, or by mineralogic changes. It appears unlikely in cores 1 and 2 that these are mineralogic changes because neither bi-plots (Figure 11) nor the χ_{lf} and IRM down core (Figures 6 and 7) show major changes in magnetic mineralogy.

The anisotropy and IRM signatures in core 4 show subtle changes associated with zones 1-4. At the base of zone 2, the increase in χ_{lf} and IRM and anisotropy is associated with a shell fragment.

In the regions of low water content, the EF fabric collapses to FF fabric yielding the observed increase in anisotropy. Grain size analysis in core 4 from the top of zone 2 through the area of increased anisotropy show little to no grain size variability nor a marked change in minerological composition. A slight increase in muscovite and biotite in the coarse silt fraction is observed in the region of increased anisotropy between zones 2 and 3, which might account for the subtle increase in χ_{lf} (Figure 8). Detailed examination across this increase in anisotropy using xray and visual examination show a minor change in fine scale laminations with an increase of layering at 40-50, 58, and 80-82 cm. This subtle increase in layering might be accompanied by an increase in permiability that limits upward migration of fluids.

Core 1 was acquired within the accumulation zone of the slide, and it is the only core to exhibit a compressional signature in the eigenvectors. The bootstrap mean V_1 trends approximately 30° (shown as arrow b in Figure 10). Despite the compressional signal, core 1 is the most "normal" of all the cores in its compaction signal. The anisotropy shows a general monotonic increase down core as expected from ordinary compaction, punctuated by several excess water content zones. The Group 1/2 transition is the least abrupt in terms of anisotropy of all the cores.

There are several spikes in the water content for core 1 that are observed in the deviation from the exponential fit of weight percent water, two of which coincide with low anisotropy zones. Zone 1 has a decrease in total anisotropy with a minor increase in water content, overlying another short interval of lower water content. Zone 2 is more dramatic than zone 1, with an increase of 7% water content over the general trend. The four specimens in zone 2 also exhibit the strongest decrease in total anisotropy.

In terms of the compaction disequilibrium scenarios outlined in the Introduction, it is possible that zones 1 and 2 are underlying less permeable intervals that act as barriers to fluid migration.

In core 2, as observed in the other cores, the areas of high water content are observed in group 2. Zone b appears to be associated with the unconformity and might record a small layer of slide deposit with small clasts above the unconformity. Zones 1 and 2 appear to be regions of underconsolidation with little to no change in magnetic characteristics as observed in χ_{lf} and IRM.

Core 4 has the most unusual Group 2 of all three cores. From 20 to 50 cm, the anisotropy increases and the water content generally matches the exponential curve. Below this interval of "normal" compaction behavior, there are two main regions that have inverted trends in anisotropy: 57-63 cm and 87-96 cm (zones 1 and 2 respectively). Both of these regions have high water content determined from the weight percent water deviating from the exponential fit. Between these two regions is an area of low water content. Below zone 2, compaction increases slightly and then anisotropy drops again in the excess water zone 3. An increase in anisotropy is observed below zone 3 and might be an impermeable layer preventing upward migration of pore fluid causing excess water content and a slight increase in water down core. Note that the there is little to no corresponding shift of χ_{lf} or IRM at the top of zone 4.

Conclusions

The principle results of our rock magnetic and seismic study may be summarized as follows:

1. AMS, when combined with water content, χ_{lf}, ARM and IRM may add additional information about the compaction history of the sedimentary sequence revealing subtle compaction disequilibria in sediments of relatively uniform composition.
2. Zones with excess water are associated with less compacted AMS signals (relatively lower anisotropy).
3. Abrupt change in the degree of anisotropy can reveal unconformities caused by evacuation of slumped material, and exhumation of underlying sediment. These sediments had generally higher anisotropies than equivalent levels in other cores (apparent overconsolidation).
4. AMS eigenvectors detected the slump with principle strain axis consistent with that expected from the slide morphology.

In summary, anisotropy of magnetic susceptibility is a tool for first order exploration of sediment consolidation state. The approach is able to identify the location of unconformities that have apparent overconsolidation, and can point to horizons that are likely to be underconsolidated. None of the methods for detecting compaction disequilibrium works for every possible situation, but AMS complements the arsenal of techniques used for detecting compaction disequilibria. When looking at AMS signatures, it is important to recognize major lithological changes because a change from clay-rich to sand-rich sediment could be misinterpreted as a major change in sediment compaction, or pore pressure. AMS cannot be used in zones where rapid diagenesis of the magnetic fraction is occurring. Caution should be used when fitting exponentials to the sediment water content as only small regions of spiking or dipping of water content will be detected.

In addition to underconsolidation, there are other mechanisms for destabilizing sediments on a slope such as zones of weakness associated with certain lithologies or bioturbation, storm wave loading, bubble-phase gas, and oversteepening. Enhancing our understanding of where underconsolidated zones are likely to occur in near surface sediments is helpful for evaluating risk factors associated with slope failure. Excess water content does not necessarily result in slope failure, but it does reduce the normal force of the overlying sediment thus

allowing the ratio of shear stress to normal stress to increase. These zones of weakness may be nucleation sites for failures.

Acknowledgments

We would like to thank NSF (grant OCE-04-25919), ONR (grant N00014-03-1-0272), and BP for funding this research. We would also like to thank the crew of the R/V Sproul, the SIO Geological Collections, and the SIO Analytical Facility. Jeff Gee provided invaluable discussion and produced fabulous new software for the magnetometers and Kappabridge.

References

Bennett, R., N. O'Brien, and M. Hulbert, Determinants of Clay and Shale Microfabric Signatures: Processes and Mechanisms, in *Microstructure of Fine-Grained Sediments, From Mud to Shale*, edited by R. Bennett, N. O'Brien, and M. Hulbert, p. 582, Springer-Verlag, New York, 1991.

Booth, J., D. O'Leary, P. Popenoe, and W. Danforth, U.S Atlantic Continental Slope Landslides: Their Distribution, General Attributes, and Implications, *Submarine Landslides: Selected Studies in the U.S. Exclusive Economic Zone*, pp. 14–22, 1993.

Borrero, J. C., J. F. Dolan, and C. E. Synolakis, Tsunamis Within the Eastern Santa Barbara Channel, *GRL*, *28*, 643–646, 2001.

Bray, N. A., A. Keyes, and W. Morawitz, The California Current system in the Southern California Bight and the Santa Barbara Channel, *Journal of Geophysical Research*, *104*, 76957714, 1999.

Constable, C., and L. Tauxe, The bootstrap for magnetic susceptibility tensors, *J. Geophys. Res.*, *95*, 8383–8395, 1990.

Dorman, C. E., and C. D. Winant, The Structure and Variability of the Marine Atmosphere around the Santa Barbara Channel, *Monthly Weather Review*, *128*, 261–282, 2000.

Driscoll, N. W., J. K. Weissel, and J. A. Goff, Potential for large-scale submarine slope failure and tsunami generation along the U.S. mid-Atlantic coast, *Geology*, *28*, 407–410, 2000.

Dugan, B., and P. Flemings, Overpressure and fluid flow in the New Jersey continental slope: Implications for slope failure and cold seeps, *Science*, *289*, 288–291, 2000.

Duncan, J., R. Hoover, C. Pflum, J. Widmier, and C. Daetwyler, Near-surface geology of the Santa Ynez Unit m Santa Barbara Channel, California, *Esso Production Reseach Company Report*, pp. 1–58, 1971.

Edwards, B., H. Lee, and M. Field, Mudflow Generated by Retrogressive Slope Failure, Santa Barbara Basin, California Continental Borderland, *Journal of Sedimentary Research*, *A65*, 57–68, 1995.

Eichhubl, P., H. G. Greene, and N. Maher, Physiography of an active transpressive margin basin: high-resolution bathymetry of the Santa Barbara basin, Southern California continental borderland, *Marine Geology*, *184*, 95–120, 2002.

Field, M., J. V. Gardner, A. E. Jennings, and B. Edwards, Earthquake-Induced Sediment Failures on a 0.25-Degree Slope, Klamath River Delta, California, *Geology*, *10*, 542–546, 1982.

Fischer, P. J., Neogene-Quaternary evolution of the Santa Barbara Basin, California, in *AAPG Bulletin*, vol. 82 of *AAPG Pacific Section meeting*, pp. 846–847, Ventura, CA, USA, 1998.

Fisher, M. A., W. Normark, H. G. Greene, H. J. Lee, and R. Sliter, Geology and tsunamigenic potential of submarine landslides in Santa Barbara Channel, Southern California, *Marine Geology*, *224*, 1–22, 2005.

Fisher, R. A., Dispersion on a sphere, *Proc. Roy. Soc. London, Ser. A*, *217*, 295–305, 1953.

Geiss, C. E., S. K. Banerjee, P. Camill, and C. E. Umbanhowar, Sediment-magnetic signature of land-use and drought as recorded in lake sediment from south-central Minnesota, USA, *Quaternary Research*, *62*, 117–125, 2004.

Hein, J. R., and J. S. Dowling, Clay Mineral Content of Continental Shelf and River Sediments, Southern California, *U.S. Geological Survey Open-File Report*, *01*, 1–26, 2001.

Hendy, I., and J. Kennett, Dansgaard-Oeschget cycles and the California Current System: Planktonic foraminiferal response to rapid climate change in Santa Barbara Basin, Ocean Drilling Program hole 893A, *Paleoceanography*, *15*, 30–42, 2000.

Henkart, P., SIOSIES, http://sioseis.ucsd.edu, 2005.

Hext, G. R., The estimation of second-order tensors, with related tests and designs, *Biometrika*, *50*, 353–357, 1963.

Hill, J. C., N. W. Driscoll, J. K. Weissel, and J. A. Goff, Large-scale elongated gas blowouts along the U.S. Atlantic margin, *J. Geophys. Res.*, *109*, 14, 2004.

Housen, B., et al., Strain decoupling across the decollement of the Barbados accretionary prism, *Geology*, *24*, 127–130, 1996.

Hu, S., E. Appel, V. Hoffmann, W. W. Schmahl, and S. Wang, Gyromagnetic remanence acquired by greigite (Fe_3S_4) during static three-axis alternating field demagnetization, *Geophys J Int*, *134*, 831–842, 1998.

Jelinek, V., The statistical theory of measuring anisotropy of magnetic susceptibility of rocks and its application, *Geophysika*, pp. 1–88, 1978.

Karlin, R., Magnetite Diagenesis in Marine Sediments From the Oregon Continental Margin, *J. Geophys. Res.*, *95*, 4405–4419, 1990.

Kawamura, K., and Y. Ogawa, Progressive change of pelagic clay microstructure during burial process; examples from piston cores and ODP cores, *Marine Geology*, *207*, 131–144, 2004.

Kayen, R. E., W. C. Schwab, H. J. Lee, M. E. Torresan, J. R. Hein, P. J. Quinterno, and L. A. Levin, Morphology of sea-floor landslides on Horizon Guyot: application of steady-state geotechnical analysis, *Deep Sea Research Part A. Oceanographic Research Papers*, *36*, 1817–1839, 1989.

King, J., S. K. Banerjee, and J. Marvin, A new rock-magnetic approach to selecting sediments for geomagnetic paleointensity studies: application to paleointensity for the last 4000 years., *J. Geophys. Res.*, *88*, 5911–5921, 1983.

Kirschvink, J. L., The least-squares line and plane and the analysis of paleomagnetic data, *Geophys. Jour. Roy. Astron. Soc.*, *62*, 699–718, 1980.

Kodama, K. P., and W. Sun, Magnetic anisotropy as a correction for compaction-caused paleomagnetic inclination shallowing, *Geophys. J. Int.*, *111*, 465–469, 1992.

Kopf, A., and J. H. Berhman, Fabric Evolution and Mechanisms of Diagenesis in Fine-Grained Sediments from the Kita-Yamato Trough, Japan Sea, *Journal of Sedimentary Research*, *67*, 590–600, 1997.

Kumar, A. A., V. P. Rao, S. K. Patil, P. M. Kessarkar, and M. Thamban, Rock magnetic records of the sediments of the eastern Arabian Sea: Evidence for late Quaternary climatic change, *Marine Geology*, *220*, 59–82, 2005.

Lambe, T. W., and R. V. Whitman, *Soil Mechanics*, John Wiley, New York, 1969.

Lee, H. J., K. Orzech, J. Locat, and E. Boulanger, Seismic strengthening, a conditioning factor influencing submarine landslide development, in *Canadian Geotechnical Conference*, vol. 57, p. 7, Quebec, 2004.

Leslie, B. W., D. E. Hammond, W. M. Berelson, and S. P. Lund, Diagenesis in anoxic sediments from the California continental borderland and its influence on iron, sulfur, and magnetite behavior, *J. Geophys. Res.*, *95*, 4453–4470, 1990a.

Leslie, B. W., S. P. Lund, and D. E. Hammond, Rock magnetic evidence for the dissolution and authigenic growth of magnetic minerals within anoxic marine sediments of the California continental borderland, *J. Geophys. Res.*, *95*, 4437–4452, 1990b.

Liu, J., R. Zhu, A. P. Roberts, S. Li, and J.-H. Chang, High-resolution analysis of early diagenetic effects on magnetic minerals in post-middle-Holocene continental shelf sediments from the Korea Strait, *J. Geophys. Res.*, *109*, doi:10.1029/2003JB002,813, 2004.

Locat, J., and H. Lee, Submarine landslides: advances and challenges, *Can Geotech J.*, *39*, 193–212, 2002.

Marks, J., A. Marianos, F. Gonzaga, and C. Pflum, Foraminiferal correlation of Quaternary sediments in the Santa Barbara Channel, California, *Cushman Foundation Special Publication*, *19*, 127–133, 1980.

Marsaglia, K. M., K. C. Rimkus, and R. J. Behl, Provenance of Sand Deposited in the Santa Barbara Basin at Site 893 During the Last 155,000 Years, in *Proceedings of the Ocean Drilling Program, Scientific Results*, edited by J. Kennet, J. Baldauf, and M. Lyle, vol. 146(2), pp. 61–75, Ocean Drilling Program, College Station, 1995.

McCabe, C., M. Jackson, and B. B. Ellwood, Magnetic anisotropy in the Trenton Limestone: results of a new technique, anisotropy of anhysteretic susceptibility, *GRL*, *12*, 333–336, 1985.

Mello, U. T., and G. D. Karner, Developement of Sediment Overpressure and Its Effect on Thermal Maturation: Application to the Gulf of Mexico Basin, *AAPG Bulletin*, *80*, 1367–1396, 1996.

Oey, L., C. Winant, E. Dever, W. Johnson, and D.-P. Wang, A model of the near-surface circulation of the Santa Barbara Channel: comparison with observations and dynamical interpretation, *J. Phys. Oceanogr*, *34*, 23–43, 2004.

O'Leary, D., and E. Laine, Proposed criteria for recognizing intrastratal deformation features in marine high resolution seismic reflection profiles, *Geo-Marine Letters*, *16*, 305–312, 1996.

Pan, Y., N. Petersen, A. F. Davila, L. Zhang, M. Winklofer, Q. Liu, M. Hanzlik, and R. Zhu, The detection of bacterial magnetite in recent sediments of Lake Chiemsee (southern Germany), *Earth Planet. Sci. Lett.*, *232*, 109–123, 2005.

Reimers, C. E., C. Lange, M. Tabak, and J. Bernhard, Seasonal spillover and varve formation in the Santa Barbara Basin, California, *Limnol. Oceanogr.*, *35*, 1577–1585, 1990.

Riedinger, N., K. Pfeifer, S. Kasten, J. F. L. Garmin, C. Vogt, and C. Hensen, Diagenetic Alteration of Magnetic Signals by Anaerobic Oxidation of Methane Related to a Change in Sedimentation Rate, *Geochimica et Cosmochimica Acta*, *69*, 4117–4126, 2005.

Rowan, C. J., and A. P. Roberts, Magnetite dissolution, diachronous greigite formation, and secondary magnetizations from pyrite oxidation: Unravelling complex magnetizations in Neogene marine sediments from New Zealand, *Earth Planet. Sci. Lett.*, *241*, 119–137, 2006.

Schlee, J. S., and J. M. Robb, Submarine processes of the middle Atlantic continental rise based on GLORIA imagery, *GSA Bulletin*, *103*, 1090–1103, 1991.

Schock, S. G., L. R. LeBlanc, and L. A. Mayer, Chirp subbottom profiler for quantitative sediment analysis, *Geophysics*, *54*, 445–450, 1989.

Schwab, W. C., H. J. Lee, and D. C. Twichell (Eds.), *Submarine landslides; selected studies in the U.S. Exclusive Economic Zone*, vol. 2002, USGS, 1993.

Schwehr, K., and L. Tauxe, Characterization of soft-sediment deformation: Detection of cryptoslumps using magnetic methods, *Geology*, *31*, 203–206, 2003.

Shaw, J. H., and J. Suppe, Active faulting and growth folding in the eastern Santa Barbara Channel, California, *GSA Bulletin*, *106*, 607626, 1994.

Snowball, I. F., Gyroremanent magnetization and the magnetic properties of greigite-bearing clays in southern Sweden, *Geophys J Int*, *129*, 624–636, 1997.

Soutar, A., and P. Crill, Sedimentation and climatic patterns in the Santa Barbara Basin during the 19th and 20th centuries, *GSA Bulletin*, *88*, 1161–1172, 1977.

Spinelli, G. A., and M. Field, Evolution of Continental Slope Gullies on the Northern California Margin, *Journal of Sedimentary Research*, *71*, 237–245, 2001.

Stephenson, A., Three-axis static alternating field demagnetization of rocks and the identification of NRM, gyroremanent magnetization, and anisotropy, *J. geophys. Res*, *98*, 373–381, 1993.

Tarduno, J. A., Temporal trends of magnetic dissolution in the pelagic realm: Gauging paleoproductivity?, *Earth Planet. Sci. Lett.*, *123*, 39–48, 1994.

Tarling, D. H., and F. Hrouda, *The Magnetic Anisotropy of Rocks*, Chapman and Hall, London, 1993.

Tauxe, L., *Paleomagnetic Principles and Practice*, Kluwer Academic Publishers, Dordrecht, 1998.

Tauxe, L., *Lectures in Paleomagnetism*, http://earthref.org/MAGIC/books/Tauxe/2005/, Magnetics Information Consortium, 2005.

Tauxe, L., H. Bertram, and C. Seberino, Physical interpretation of hysteresis loops: Micromagnetic modelling of fine particle magnetite, *Geochem., Geophys., Geosyst.*, *3*, DOI 10.1029/ 2001GC000,280, 2002.

Thunell, R., E. Tappa, and D. Anderson, Sediment fluxes and varve formation in Santa Barbara Basin, offshore California, *Geology*, *23*, 1083–1086, 1995.

Ward, S. N., Landslide tsunami, *Journal of Geophysical Research*, *106*, 11,201–11,216, 2001.

Warrick, J., L. Washburn, M. Brzezinski, and D. Siegel, Nutrient contributions to the Santa Barbara Channel, California, from the ephemeral Santa Clara River, *Estuarine, Coastal and Shelf Science*, *62*, 559–574, 2005.

K. Schwehr*, Scripps Institution of Oceanography, La Jolla, CA 92093-0220, USA (e-mail: schwerhr@gmail.com); L. Tauxe, Scripps Institution of Oceanography, La Jolla, CA 92093-0220, USA (e-mail: ltauxe@ucsd.edu); N. Driscoll, Scripps Institution of Oceanography, La Jolla, CA 92093-0220, USA (e-mail: ndriscoll@ucsd.edu); H. Lee, US Geological Survey, MS 937, 345 Middlefield Rd, Menlo Park, CA 94025-3561,(e-mail: hjlee@usgs.gov) * New Address: Center for Coastal and Ocean Mapping, Chase Ocean Engineering Lab, 24 Colovos Road, Durham, NH 03824, (e-mail: schwehr@ccom.unh.edu)

Core	Latitude	Longitude	Depth(m)	Length(m)
1	34° 21' 40.2"	-120° 06' 28.8"	480	1.68
2	34° 22' 12.0"	-120° 06' 27.0"	439	0.73
4	34° 22' 44.4"	-120° 03' 25.8"	322	1.25
ODP 893	34° 17' 15.0"	-120° 02' 12.0"	577	187.00

Table 1. Locations and lengths of the cores collected on the R/V Sproul during August 2004. Ocean Drilling Project (ODP) Leg 146 Hole 893A is included as it is near the study area.

Core	Depth(m)	Figure	χ_{lf} μSI	χ_{hf} μSI	χ_{lf}/χ_{hf}
1	0.635	12a	182.4	82.7	0.45
2	0.270	12b	133.1	123.1	0.93
3	0.810	12c	162.9	82.0	0.50

Table 2. Specimen susceptibility measurements. A MicroMag 2900 Alternating Gradient Force Magnetometer (AGFM) was used for high field susceptibility (χ_{hf}) and a KLY-2 Kappabridge for low field susceptibility (χ_{lf}) results.

Core	Section	$\bar{D}$	$\bar{I}$	N	R	κ	α_{95}	Depth (m)
1	1	134.3	50.4	6	5.8591	35	11.4	0.00-0.37
1	2	343.4	45.5	40	34.7466	7	8.9	0.37-1.68
2	1	344.7	56.0	23	20.7940	9	10.1	0.00-0.73
4	1	62.4	52.5	39	36.0973	13	6.6	0.00-1.25

Table 3. Fisher statistics (*Fisher* [1953]) of alternative field (AF) demagnetization of the natural remanent magnetization (NRM) by core sections. The declination is in the core section local frame before reorientation to geographic north. Based on a Geocentric Axial Dipole (GAD) model, the expected inclination for these cores is 53.8°. *Note* : $\bar{D}$ is mean declination; $\bar{I}$ is mean inclination; N is number of specimens; R is the length of resultant vector; κ is the *Fisher* [1953] precision parameter; and α_{95} is the estimate of the circle of 95% confidence.

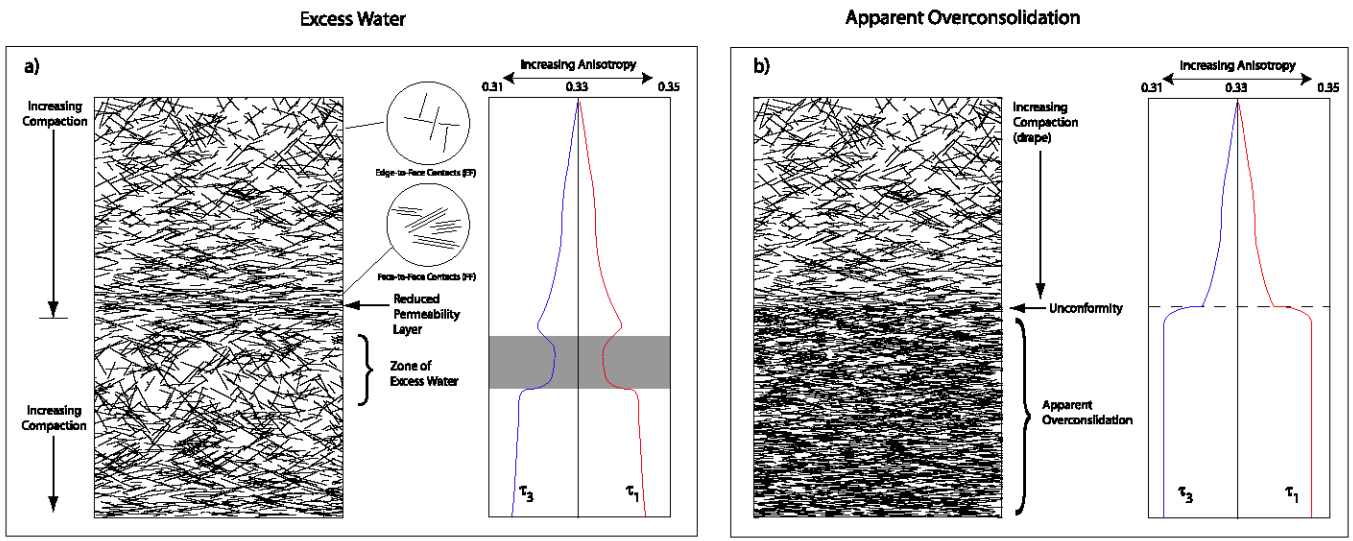

Figure 1. Schematic of compaction disequilibriums. a) Clay particles in sediment undergoing compaction. Particles compact and create a reduced permeability layer. Below this layer, excess water content can in turn retard compaction. The excess is generated by the low permeability layer that temporarily reduces upward migration of pore fluids. Below the zone of excess water, compaction increases down section. The graph on the right is an idealized model of how compaction e?ects the anisotropy of magnetic susceptibility (AMS) fabric. As compaction progresses, overall anisotropy increases. Zones of excess water are detected by regions of reduced anisotropy (marked with a gray band). b) Platy clay particles in sediment undergoing compaction with a zone of apparent overconsolidation created by an unconformity.

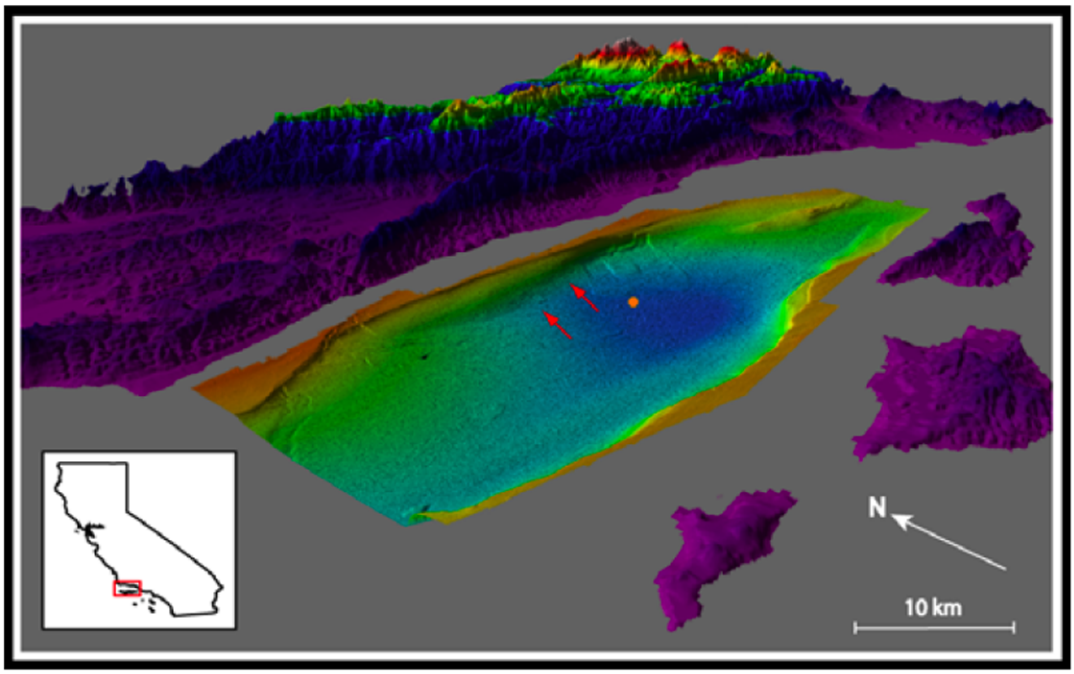

Figure 2. The Santa Barbara Basin (red box in the inset) is a part of the California Borderlands and is located south of the Transverse Ranges in California. The motion on the San Andreas Fault System has created a closed basin that is partially shielded from the flushing action of the California Current. Rapid deposition on steep slopes combined with frequent large earthquakes have resulted in a number of slides in the recent Holocene sediments. The study areas are marked with red arrows: the Gaviota slide on the left, and the slope crack on the right. The bathymetry is from the MBARI EM300 multi-beam survey (*Eichhubl et al.* [2002]). Also shown is the location of ODP Site 893 (orange circle).

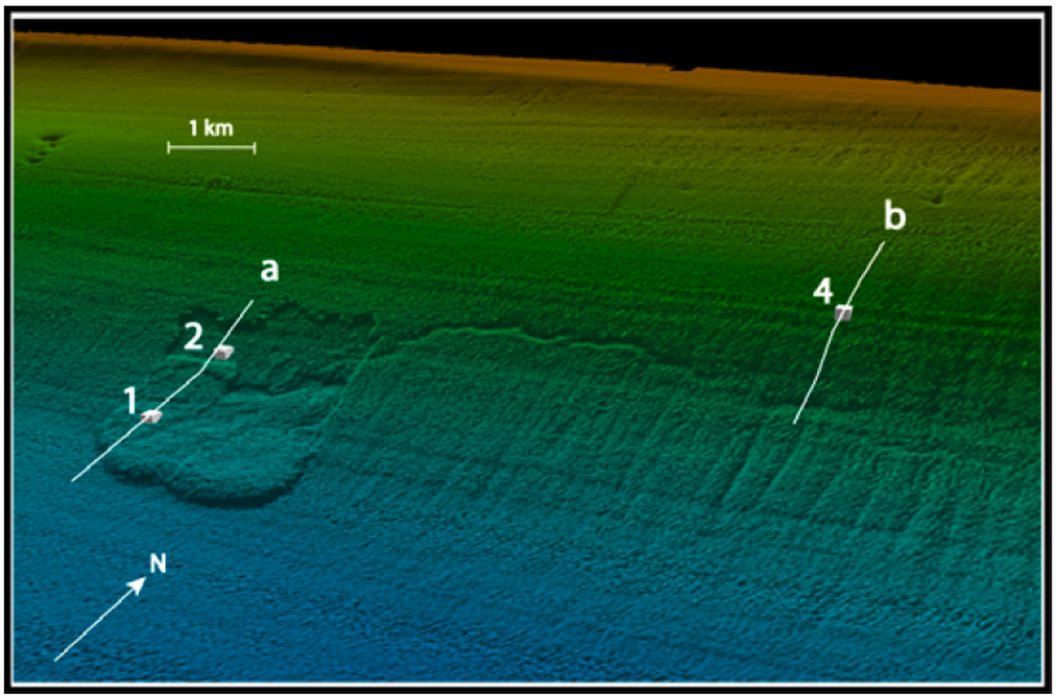

Figure 3. Enlargement of the Gaviota Slide on the northern slope of the Santa Barbara Basin shows a well imaged underwater landslide. Two gravity cores were acquired within the slide boundaries; core 1 is in the accumulation zone (toe) of the slide. Core 2 is in the evacuation zone. A large crack on the right is connected to the Goleta Slide to the East. The crack extends East-West along the slope between the Gaviota and Goleta Slides for 8 km. It is between 5 and 20 meters wide and appears to cut the many rills that run down slope. Core 4 is located 780 meters up-slope from the crack. The bathymetry is shown with a vertical exaggeration of 6x. CHIRP seismic lines a and b are shown in Figures 4 and 5 respectively.

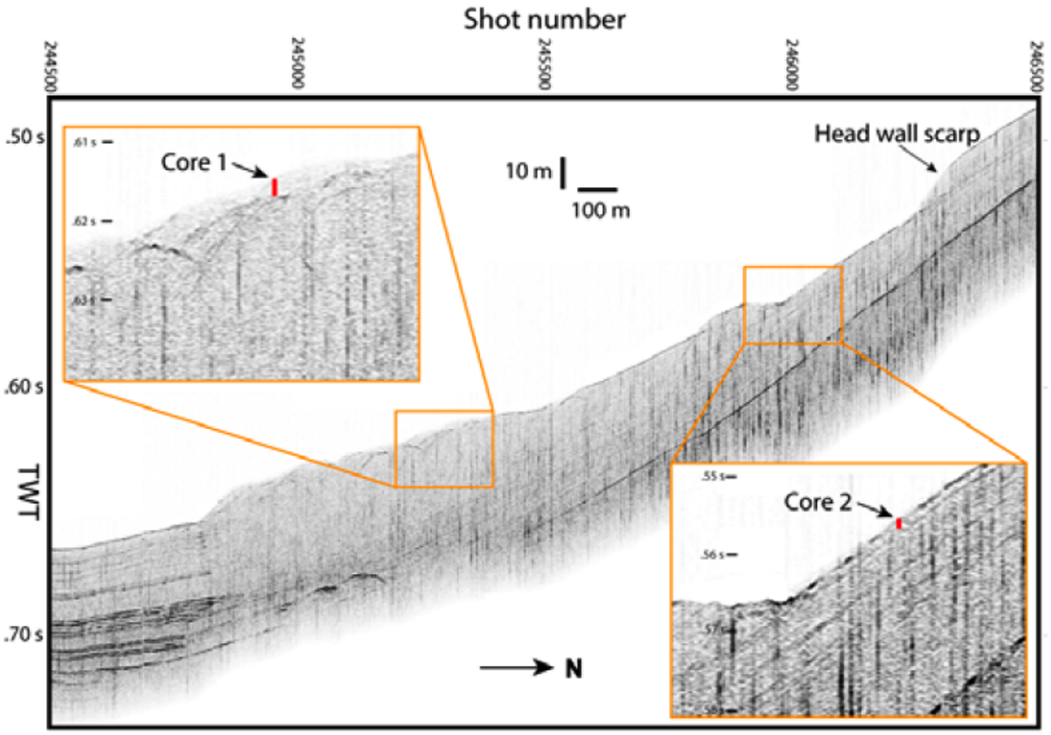

Figure 4. CHIRP seismic line imaging the western half of the Gaviota Slide. Line extends 2.5 km from 509 mbsl (120° 06' 30.00" W, 34° 21' 09.00" N) up slope to 377 mbsl (120° 06' 29.00" W, 34° 22' 31.00" N; line a in Figure 3). Cores 1 and 2 are marked in red on the figure insets with length scaled to a velocity of 1500 m/s. The vertical axis is two way travel time (TWT) in seconds. The horizontal axis is in shot numbers and the scale bar is based on the average number of shots per 100 m. Note that the the CHIRP firing rate varies with water depth. Core 1 is located in the accumulation zone of the Gaviota Slide in an area of disrupted reflectors. Core 2 was collected in the evacuation zone of the slide and penetrates the overlying drape into the material below the slide surface.

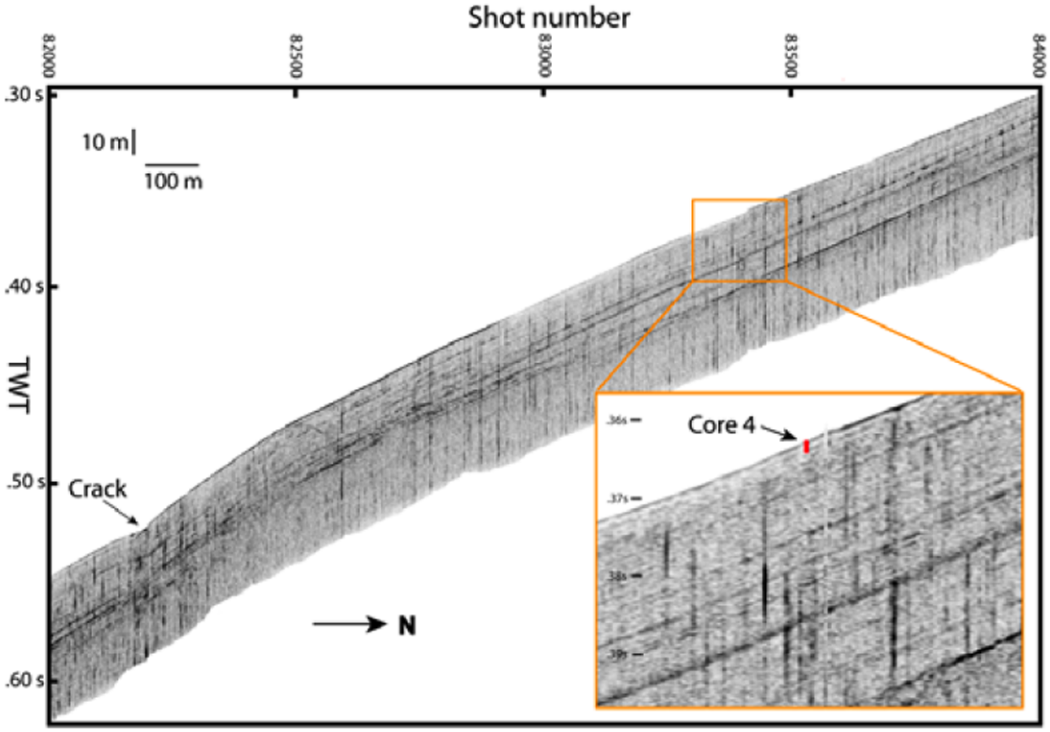

Figure 5. CHIRP seismic line across the crack between the Gaviota and Goleta slides. This line extends 1.9 km from 420 mbsl (120° 03' 30.00" W, 34° 22' 09.00" N) up slope to 247 mbsl (120° 03' 20.00" W, 34° 23' 09.00" N; line b in Figure 3). Core 4 is marked in red on the figure with length scaled to a velocity of 1500 m/s. (See also caption in Figure 4)

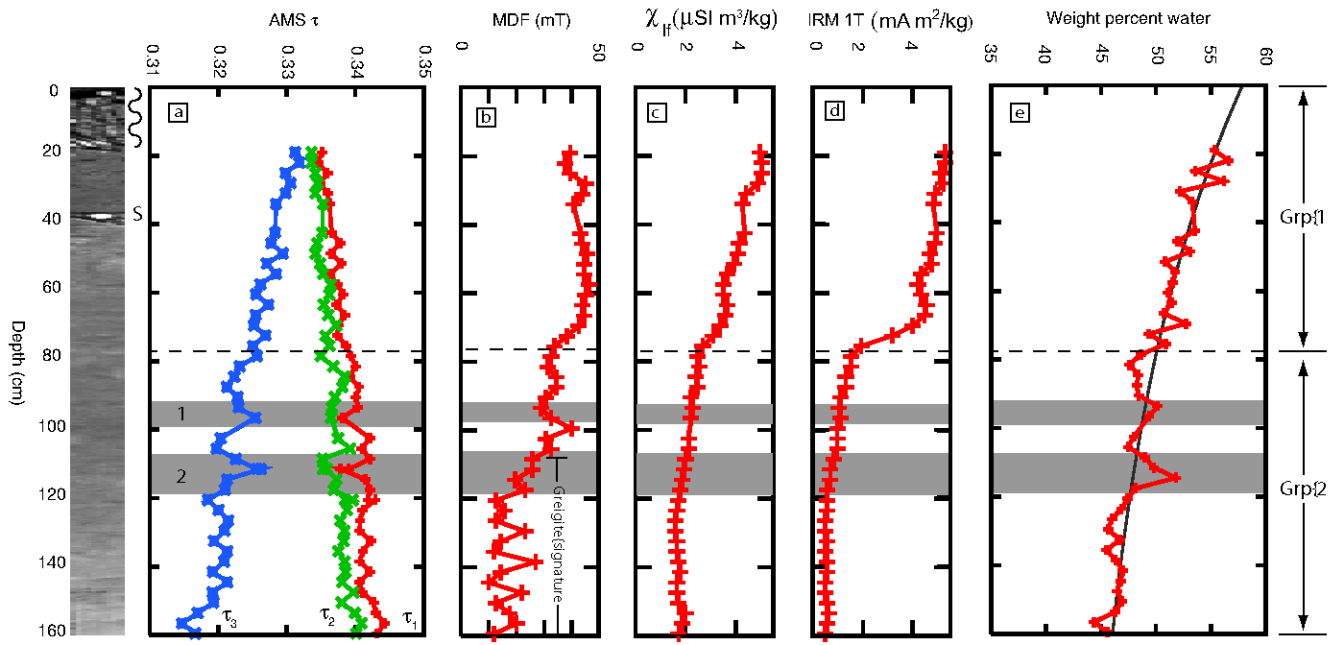

Figure 6. Core 1 is located in the toe of the Gaviota Slide (Figures 3 and 4). On the left is the core photograph. To the right of the core photograph are the major core features. The top 20 cm of the core is disturbed (wavy region) and the discontinuity at 40 cm is a section boundary (S). a) AMS eigenvalues. τ_1 is the maximum eigenvector, while τ_3 is the minimum, and $\tau_1 + \tau_2 + \tau_3 = 1$. The core has a general trend down core of increasing anisotropy with a more oblate fabric. b) Median destructive field (MDF) c) Bulk susceptibility (χ_{lf}) shows a gradual decrease down through the core. d) Isothermal remanent magnetization (IRM) shows an abrupt transition at the dashed line. Greigite like behavior is mark for the bottom region of the core. e) Exponential fit to water content data. Core 1 has two zones of high water content that are marked as 1 and 2. These zones correlate to areas of lower anisotropy. The weight percent water is calculated by dividing the weight of 8 cm^3 of dried material from the wet weight. On the right are indicated the extent of groups 1 and 2. Group 1 has high MDF, χ_{lf}, and IRM. Group 2 is the transition to Group 2 which has low MDF, χ_{lf}, and IRM.

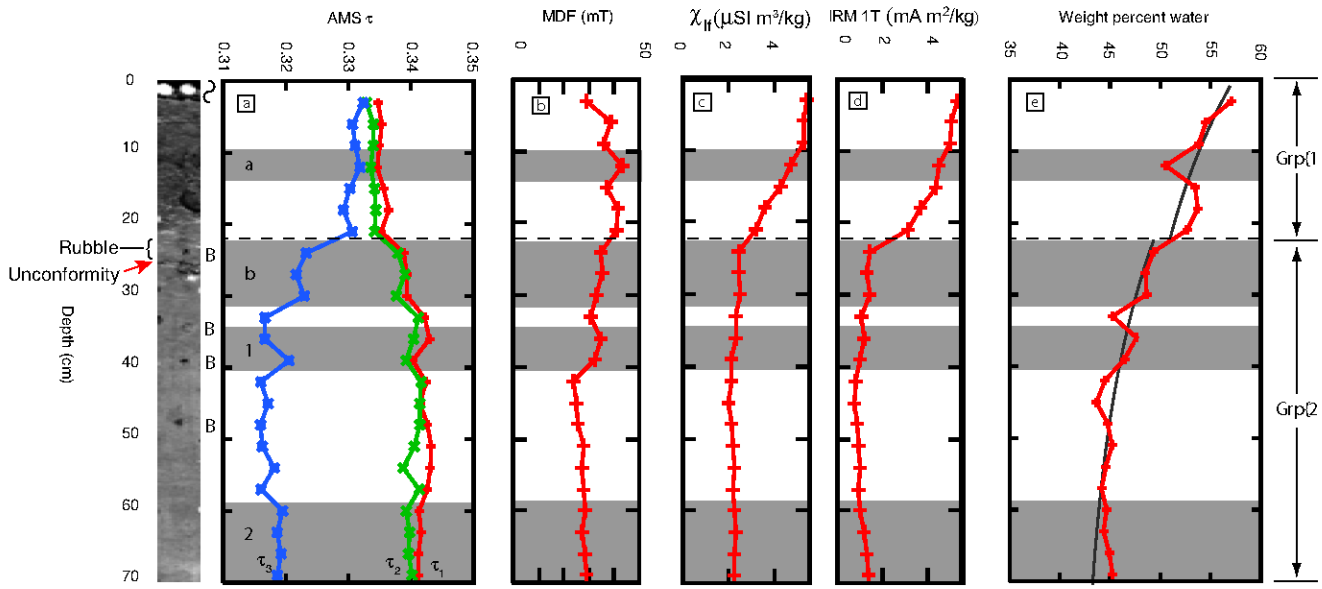

Figure 7. Core 2 is located in the evacuation zone of the Gaviota Slide (Figures 3 and 4). Features are denoted on the right of the core photo. D is the unconformity and B are the locations of burrows. There is a zone of disturbed material 7 cm from splitting. The red arrow marks the unconformity on the core photograph. a) The AMS eigenvectors show a strong jump to a more anisotropic fabric for the specimens at 24, 27, and 30 cm below the sediment water interface. Below 33 cm in the core, the AMS signature is more constant. b) MDF c) χ_{lf} d) IRM e) Exponential fit to water content data. The fit is not robust because of the low number of data points and the presence of a large unconformity. The weight percent water shows a transition to a constant value at 42 cm depth. Zone a is soft material which was damaged by the coring process. The dashed line line shows the Group 1 to Group 2 transition.

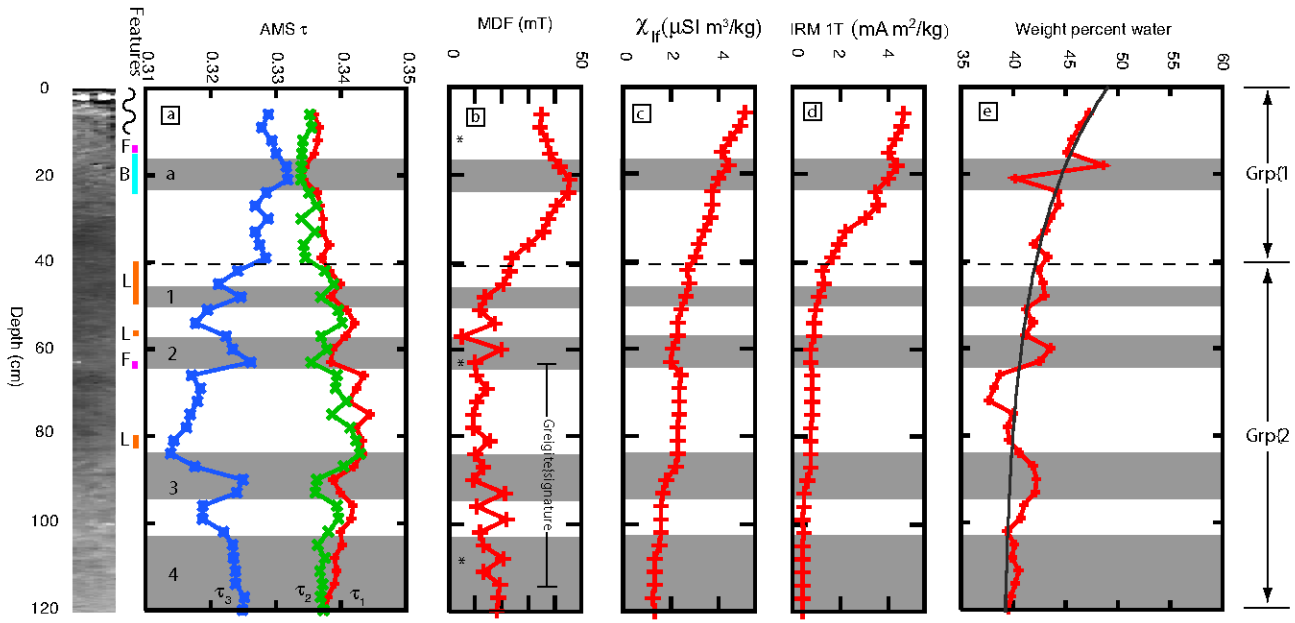

Figure 8. Core 4 is located above the above the crack between the Gaviota and Goleta slides (See Figures 3 and 5). On the left, important core features are marked: shell fragments in magenta, burrows in cyan, and layering in orange. Zone a is caused by burrows that was identified in an x-radiograph. The dashed line line shows the IRM transition. a) Anisotropy shows a systematic trend increasing down to 84 cm. Zones 1, 2 and 3 deviate from this trend of compaction. b) The median destructive field reaches a constant baseline by 48 cm depth. Vector end point diagrams for three AF demagnetizations (located by '*') are shown in Figure 9). c) χ_{lf} d) IRM e) The exponential fit to the water content data show increased water content for the three gray zones. Between layers 1 and 2 is a zone of lower water content (down to 38%). The exponential fit was only applied down to 84 cm because of the size of zones 2 and 3.

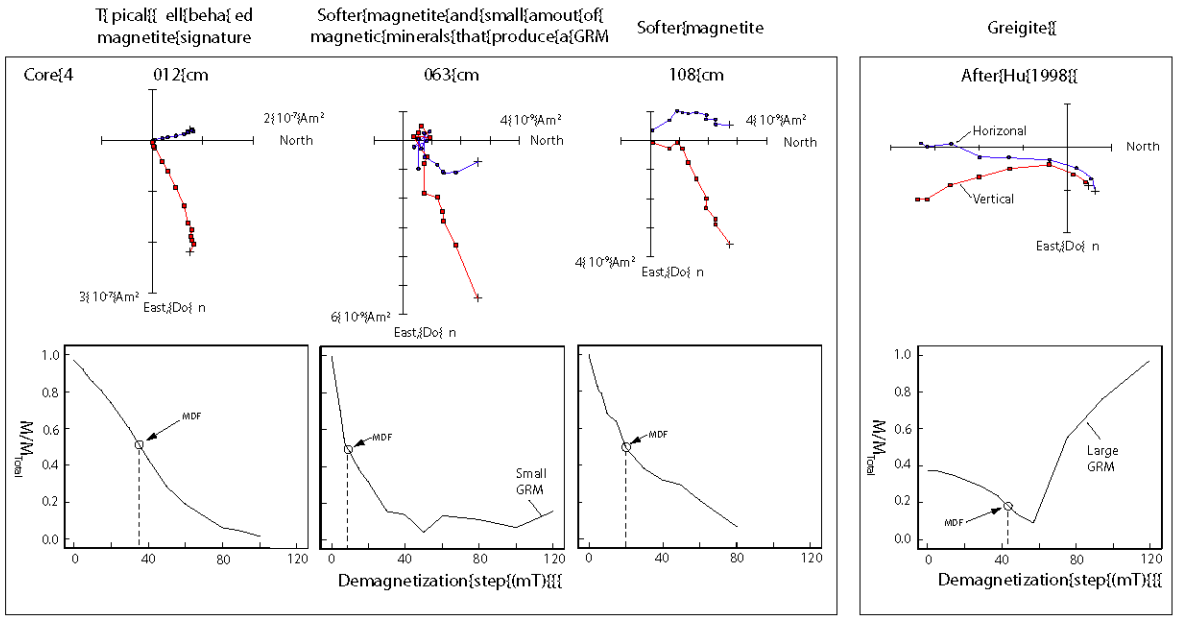

Figure 9. Zijderveld plots showing examples AF demagnetization data. Horizontal projection, blue circles, and vertical component(north-down), red squares, are shown in the top of the figure. The greigite sample (*Hu et al.* [1998]) exhibits demagnetization vectors that diverges away from the origin as it acquired a gyro-remanent magnetization (GRM). The bottom plot shows that the intensity increases for demagnatizations above 60 mT. The locations of these samples from core 4 are shown in Figure 8b.

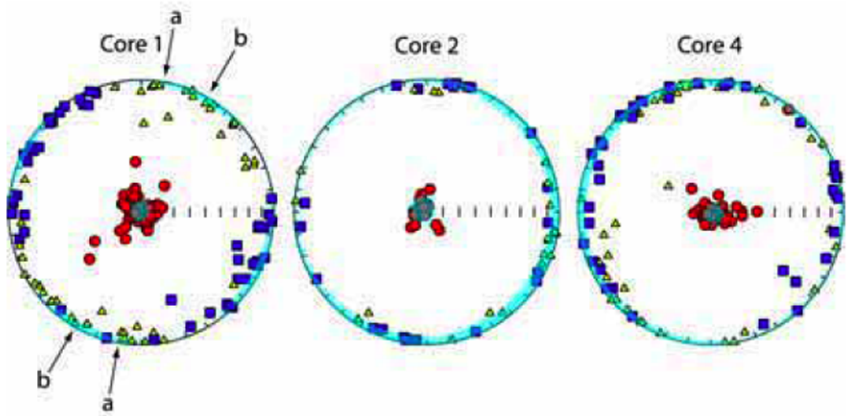

Figure 10. Best fit eigenvectors with the minimum eigenvectors (V_3) as red circles, the maximum eigenvectors (V_1) are blue squares and intermediate eigenvectors (V_2) are yellow triangles. Cores have been rotated to match the best estimate from principle component analysis (PCA) of alternating frequency (AF) demagnetization of the remanent magnetization. Arrow (a) on Core 1 shows the direction of compression determined from morphology observed in the multi-beam data (Figure 3). Arrow (b) shows the predicted compression direction based on the best fit perpendicular to the V_1 vectors (*Schwehr and Tauxe* [2003]). Bootstrap eigenvectors enclosing the 95% confidence bounds are shown in cyan. Note the well defined confidence intervals for the V_1 in core 1. In contrast, core 2 and 4 show no prefered orientation of the V_1.

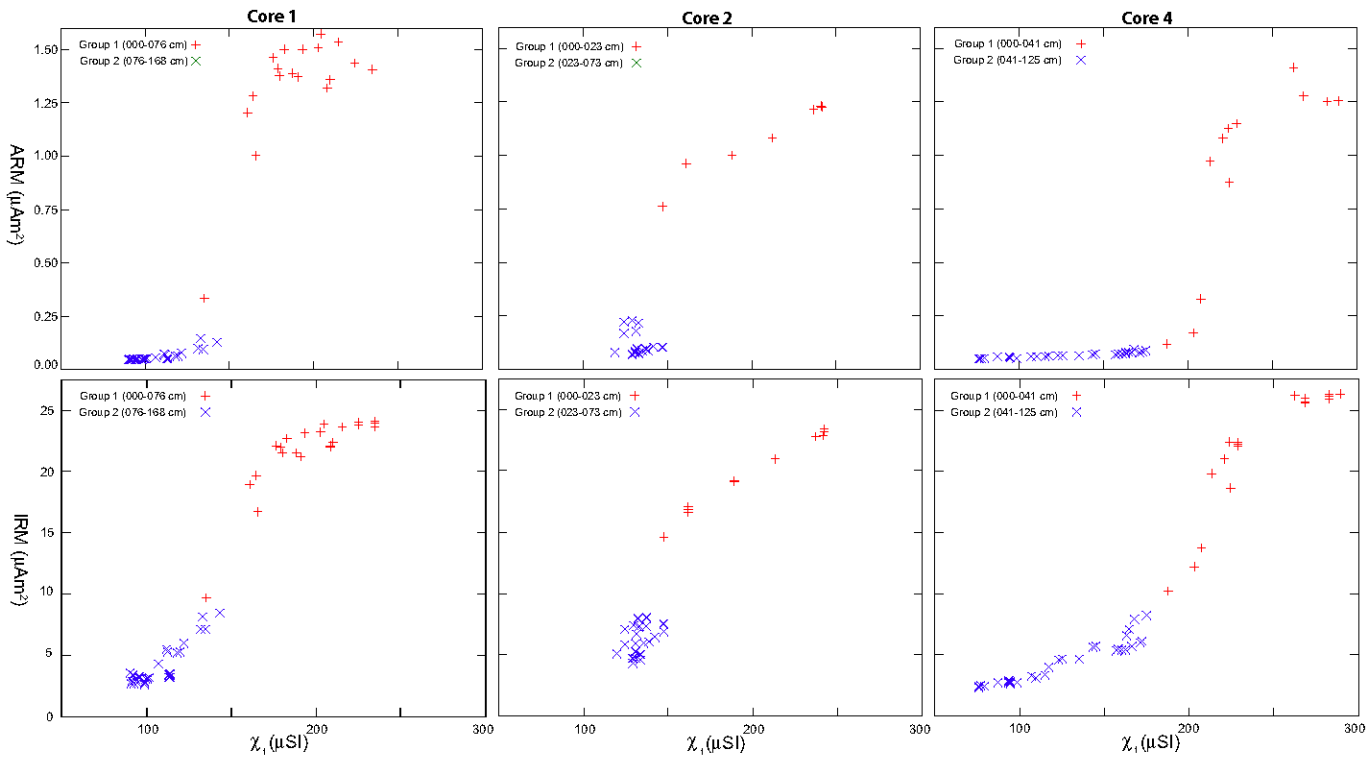

Figure 11. Bi-plots of ARM or IRM versus susceptibility. There are two modal groups of magnetic compositions indicated by pluses and crosses, which are stratigraphically controlled, pluses being core tops.

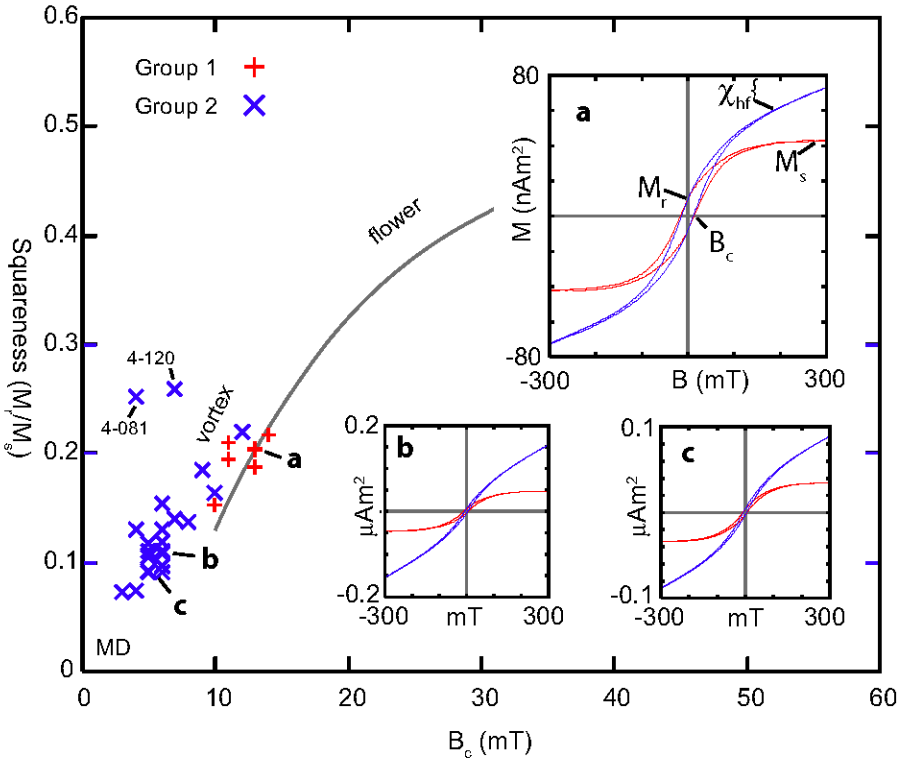

Figure 12. Squareness versus coercive field plot after *Tauxe et al.* [2002]. Insets a-c show representative hysteresis loops for points on the graph. Inset a is enlarged to show the definitions of the hysteresis parameters. The blue loop is the uncorrected measurements of the magnetization (M) induced by an applied field (B). The slope of the blue raw loops where they converge is used to calculate the high field susceptibility (χ_{hf}). The rest of the parameters are calculated from the red slope, that is created by removing the blue high field slope. The bulk coercivity (B_c) is a measure of how stable the magnetic grains are and is the point where the red curve crosses the x-axis. M_s is the saturation magnetization. M_r is the saturation remanence where the red loop intersects the y-axis as the applied field is lowered from M_s.

III.M Chapter Acknowledgment

Chapter 3, in full, is the material as submitted to *Geochemistry, Geophysics, Geosystems*, Detecting Compaction Disequilibrium with Anisotropy of Magnetic Susceptibility, Schwehr, Kurt; Tauxe, Lisa; Driscoll, Neal; Lee, Homa; 2006.

The CHIRP seismic data and cores were collected on the BPSIO-2004 cruise with Jeff Dingler and Kurt Schwehr as Co-Chief Scientists for that portion of the cruise. I was responsible for all of the core processing, CHIRP processing, analytical work, and data analysis. The data interpretation was done in conjunction with Lisa Tauxe, Neal Driscoll, and Homa Lee. Jeff Gee provided valuable advice and discussion. Lisa Tauxe, Neal Driscoll, and Homa Lee edited the text.

Chapter IV

Origin of continental margin morphology: submarine-slide or downslope current-controlled bedforms, a rock magnetic approach

Origin of continental margin morphology: submarine-slide or downslope current-controlled bedforms, a rock magnetic approach

Kurt Schwehr, Neal Driscoll, Lisa Tauxe

Scripps Institution of Oceanography, University of California, San Diego

Abstract.
Morphological features observed in both swath bathymetry and seismic reflection data are not unique, which introduces uncertainty as to their origin. The origin of features observed in the Humboldt Slide has generated much controversy because the same features have been interpreted as a submarine failure deposit versus current-controlled sediment waves. It is important to resolve this controversy because similar structures are observed on many continental margins and the origin of these features needs to be understood. Anisotropy of magnetic susceptibility (AMS) measurements on sediment samples acquired from the Humboldt Slide reveal that the top ~8 m have not experienced post-depositional deformation. This suggests that these features are formed by primary deposition associated with downslope currents. Using the same AMS technique on a core acquired *north* of the Humboldt Slide in a region with no geophysical evidence for post-depositional deformation, we were able to identify a ~1 m thick deposit that appears to be a small slump.

Introduction

Landslides on continental margins can have a devastating effect on the coastal environment because of the possibility of tsunamis and the ensuing coastal erosion. Accurate risk assessment demands that we know the probability of large landslides occurring. This in turn requires knowledge of the frequency of landslide events in the past. To assess frequency, it is necessary to identify, with some certainty, features that are products of slope failure. Given the controversy surrounding identification of features such as the Humboldt Slide, the development of criteria for positive identification of post-depositional deformation gains urgency.

Seismic and outcrop stratigraphic studies have shown that margin sedimentary successions are pervaded by physical discontinuities which occur over a wide range of scales and are generated by various processes acting separately or in concert (*Christie-Blick and Driscoll* [1995]). Geologists have long appreciated the importance of submarine landslides and failures in the development of unconformities (*Embley and Jacobi* [1986]; *Booth et al.* [1993]; *Evans et al.* [1996]). Recently there has been much debate concerning the identification of submarine landslides and rotational slumps in seismic reflection data (*Dillon et al.* [1993]; *Gardner et al.* [1999]; *Holbrook* [2001]; *Holbrook et al.* [2002]; *Lee et al.* [2002]; *Trincardi et al.* [2004]). The controversy arises, in large part, because the stratal geometry of many deposits, previously identified as retrogressive slumps, is not unique and could equally be generated from down- or along-slope currents (e.g. Blake-Bahama collapse structure, *Holbrook et al.* [2002]; Humboldt Slide in the Eel River basin, Figure 1). Deposition and erosion of the slope may be caused by a number of different processes (e.g., slope failure, incision and overbank deposits, bottom currents, shelf-edge deltas). Understanding how these processes sculpt the continental slope is critical to generating quantitative geologic models of continental slope evolution (*Pratson and Coakley* [1996]; *Driscoll and Diebold* [1999]). Developing a test to discriminate between these alternative scenarios (i.e., retrogressive slumps versus current-controlled deposits) would provide valuable new insights into the origin of these deposits and their relative importance in the construction and evolution of continental margins.

Gardner et al. [1999] interpret the Humboldt Slide as having been formed by retrogressive failure and rotation of blocks above a shear zone. *Lee et al.* [2002] reinterpreted the Humboldt Slide complex as sediment waves emplaced by downslope gravity flows and argued that sediment waves infill a slide scar. The differing interpretations of the structure by *Gardner et al.* [1999] and *Lee et al.* [2002] highlight the ongoing controversy regarding the origin of this type of morphological feature around the globe (of which the Humboldt Slide complex is only one such example). These two interpretations (primary depositional features versus retrogressive faulting and internal deformation) are based on the same Huntec (*Dodds* [1980]) seismic data set.

Can the origin of these deposits be resolved from seismic data alone? Possibly, but at great expense. For example, *Holbrook* [2001] reinterpreted existing USGS data from the Blake-Bahama outer ridge and refined the previous interpretation of *Dillon et al.* [1993] that certain features were normal faults associated with a gas-hydrate collapse structure. By examining the stratal geometry, *Holbrook* [2001] suggested the structures were growth faults recording several events, not just one event as suggested by *Dillon et al.* [1993]. Subsequently, *Holbrook et al.* [2002] then conducted an expensive 3D seismic survey to define the nature of the collapse structures and identify potential Ocean Drilling Project (ODP) drilling targets to understand gas hydrate systems. After acquiring the seismic data set, *Holbrook et al.* [2002] concluded that the features were in fact not growth faults, but were actually sediment waves.

In this paper, we apply a test based on sedimentary fabric as characterized by anisotropy of magnetic susceptibility (AMS) for assessing the origin of these ambiguous features. The test is based on magnetic fabrics to determine the extent of post-depositional deformation, a prediction of the faulting hypothesis. The AMS method has the potential to distinguish between internal deformation and primary sedimentary fabrics at a fraction of the cost of a 3D seismic survey. AMS can also provide additional insight into the burial history of sediments (e.g. *Kopf and Berhman* [1997]; *Kawamura and Ogawa* [2004]; *Schwehr et al.* [submitted]). We will outline the AMS test that we applied on core samples obtained from the Humboldt Slide (Figure 2) and describe the results.

Geologic Setting

The ongoing deformation, uplift, and erosion of the Californian hinterland provide vast amounts of sediment to the U.S. Pacific continental margin (*Field and Barber* [1993]; *Clarke* [1987]). The relatively high rate of sedimentation and recurrence of earthquakes (*Couch* [1980]) makes the Eel River Basin an ideal locale to examine slope failure and consequent slide deposits. In addition to strong forcing functions, vast amounts of data have been acquired in the Eel Basin as part of the ONR STRATAFORM project (*Nittrouer* [1999]). This background allows us to place our results into a well-defined geological framework.

The mouth of the Eel River (*Nittrouer* [1999]), located at 40° 39'N, 124° 19'W, delivers sediment from a relatively small rugged catchment, with a drainage area of 8,640 km^2 and a maximum elevation of ~2000 m. Both the Eel and the Mad Rivers, the latter being to the north, occupy subsiding synclines striking NNW across the Gorda-North American convergent plate margin. The Eel River has the highest sediment yield in the contiguous United States, when normalized by its drainage area (*Milliman and Syvitski* [1992]). The Eel River is a storm dominated system where most sediment is discharged during short duration winter floods (*Sommerfield and Nittrouer* [1999]). For example, the 1995 Eel River flood alone delivered 23 Tg of suspended sediment, which is about one eighth of the annual total suspended sediment (TSS) discharge from the Mississippi River (*Milliman and Syvitski* [1992]). Sediment bypass and rapid accumulation on the slope are common along the California margin because of the narrow continental shelf. High pore pressures are commonly associated with rapid sediment accumulation and frequent earthquakes are potential triggers for slope failure.

The Humboldt Slide deposit mantles a bowl-shaped depression that extends from the outer shelf, to the middle slope on the Eel Margin (Figure 2). The depression is bounded to the north by a plunging anticline (Little Salmon Anticline), and to the south by a bathymetric ridge. The internal geometry and bedforms of the Humboldt Slide deposit display many similarities with current-controlled deposits identified in other ocean basins (e.g., *Heezen and Hollister* [1964]; *Lonsdale and Spiess* [1977]; *Flood* [1980]; *Laine et al.* [1994]; *Driscoll and Laine* [1996]; *Lee et al.* [2002]). On the basis of the internal geometry and surficial morphology, two competing hypotheses have emerged: (1) The Humboldt Slide deposit and internal geometry were formed by retrogressive failure and rotation above a shear zone

(i.e., detachment) with minimal lateral translation of the deformed sediment carapace (*Gardner et al.* [1999]), and (2) The deposit records primary deposition by density currents (hyperpycnal flows) cascading down a pre-existing slide scar (*Lee et al.* [2002]). In the primary deposition scenario, previous slope failure and evacuation of the failed material over-steepened the local slope and created the Humboldt Slide scar. Acceleration of the density flows in response to the locally over-steepened slope gives rise to current-controlled bedforms in this region.

Other portions of the continental slope along the Pacific North-West margin exhibit only slightly lower sediment accumulation rates compared to those observed off of the Eel River (*Wheatcroft and Sommerfield* [2005]). This poses a problem given that the Eel River has substantially higher suspended sediment discharge (averaging $18Tg/yr$, *Wheatcroft and Sommerfield* [2005]) than the other river systems in the area. The Eel River basin has a narrow shelf (22 km from the Eel River to the shelf break above the Humboldt Slide) such that sediment can potentially escape over the shelf break onto the shelf slope and beyond (*Alexander and Simoneau* [1999]). The typical winter swell can re-suspend sand in 50-80 m of water, whereas large storms can rework sand on the middle to outer shelf, and perhaps down to the upper slope (*Alexander and Simoneau* [1999]). Deposition rates derived from ^{210}Pb and ^{137}Cs reveal high sediment accumulation rates (SAR) on the shelf, and on the slope in the area of the Humboldt Slide (*Alexander and Simoneau* [1999]).

Methods

Sedimentary AMS fabrics

Early workers such as *Ising* [1942], *Rees* [1961], and *Marino and Ellwood* [1978] suggested the use of AMS to test the reliability of natural remanent magnetism (NRM) measurements from sediments. From these measurements, they concluded that "normal" (oblate) AMS fabrics should generally yield robust results for paleomagnetic field studies. They found poor or incorrect results from samples that showed distorted magnetic fabrics and suggested a wide range of possible causes, including slumping.

Kanamatsu et al. [2001] summarized the potential ways that AMS fabric could be altered by internal (mineralogical) changes and physical reorientation of magnetic grains. Internal changes may be from magnetostriction, growth or dissolution, and brittle or plastic deformation of individual grains. Physical reorientation can be non-coaxial (simple) shear or compaction, which does not alter the fabric within each grain, however the strain will still alter the overall magnetic fabric.

A range of laboratory experiments have been conducted to examine the depositional controls on magnetic fabrics. For example, *Rees and Woodall* [1975] investigated a variety of materials using both running-water deposition and deposition from slurries slumping. The experimental results suggest a systematic variation in the AMS fabric with changes in the critical shear stress in the bottom boundary layer (i.e., increasing water current velocity). Additional experiments with plaster mixtures found that the eigenvector associated with the maximum eigenvalue can align either parallel or perpendicular to flow direction depending on flow conditions (*Rees* [1983]).

Several authors have recognized the effects of sediment deformation on NRM (see *Tarling and Hrouda* [1993] and *Tauxe* [1998] for summaries). For example, *Rosenbaum et al.* [2000] examined a core (OL-92) from Owens Lake, CA that contains sediments ranging from 800 ka to the present. The original interpretation of the OL-92 magnetic record was that there were a number of geomagnetic excursions in the Brunhes Chron (*Glen and Coe* [1997]). *Rosenbaum et al.* [2000] found that sediment deformation was associated with a number of these "excursions" and that the eigenvector associated with the minimum magnetic susceptibility (here called V_3) could be used as an indicator for deformation. If the direction of V_3 is significantly deflected from vertical, that portion of the core might have been deformed, and therefore should not be used for field direction or field intensity. *Rosenbaum et al.* [2000] arrived at the conclusion that the deformation observed in the OL-92 core was a result of fluidization. A seismic survey conducted after coring shows that the OL-92 core is located in the Owens Valley Fault Zone (*Brooks and Johnson* [1997]) and the deformation could result from a combination of drilling and faulting.

Given that AMS is extremely sensitive to strain (*Housen et al.* [1996]; *Kanamatsu et al.* [2001]), magnetic fabric has recently been used to detect subtle deformation of sediments and to distinguish geomagnetic features from deformational artifacts (e.g., *Rosenbaum et al.* [2000]; *Cronin et al.* [2001]). *Cronin et al.* [2001] suggested that AMS could be used to detect slumps not otherwise obvious from the geologic field evidence (so-called "crypto-slumps", *Schwehr and Tauxe* [2003]). These studies show that AMS can distinguish between post-deposition deformation and primary depositional features. Although AMS has long been used to detect

deformation in a variety of geological applications, our aim is to determine the geological origin of a continental margin deposit. AMS may provide a powerful method that can be used in a number of geological settings to detect post-depositional deformation where existing data are equivocal.

There is always the possibility that there might be complications in the AMS results caused by diagenetic effects on the magnetic mineralogy. Such changes can be detected using rock magnetic methods such as anhysteretic remanent magnetization (ARM), isothermal remanent magnetization (IRM), low field bulk susceptibility (χ_{lf} or sometimes written just χ) and high field susceptibility χ_{hf} (e.g. *Banerjee et al.* [1981]; *King et al.* [1982]; *Karlin* [1990a]; *Leslie et al.* [1990a]; *Tauxe et al.* [2002]; *Egli* [2004]).

Development of magnetic fabric in sediments

Here we summarize decades of research on AMS fabric in sediments in a variety of current regimes (see Figure 3; *Tarling and Hrouda* [1993]). In quiet water conditions (Figure 3a), there is a tendency for elongate particles to lie sub-parallel to the bedding plane. As the magnetic susceptibility is usually at a maximum parallel to the long axis of particles, the direction of maximum magnetic susceptibility (V_1) will tend to lie close to the plane of the bedding. However, there is no preferred direction within the bedding plane, therefore V_2 and V_1 will be indistinguishable as will the associated eigenvalues (τ_2 and τ_1). Hence, the magnetic fabric will be oblate with a vertical V_3 direction.

In moderate water currents (Figure 3b), especially on inclined bedding planes, particles may be slightly deflected, resulting in off-vertical V_3 directions. Here too, we expect the fabric to be characterized by an oblate AMS ellipsoid, but the V_3 direction will be deflected in the direction of the paleocurrent.

What happens to the magnetic fabric during post-depositional deformation is more complex. Initial theoretical work on the relationship between magnetic fabrics and actual grain fabrics with respect to strain was conducted by *Owens* [1974], *Hrouda and Hruskova* [1990], and *Housen et al.* [1993]. Most studies using AMS fabric to determine strain have been applied on tectonic scales and have examined weakly metamorphosed rocks (e.g. *Kanamatsu et al.* [2001]; *Pares et al.* [1999]). Studies on such low-grade metamorphic rocks are complicated because chemical changes during metamorphism may affect the magnetic minerals to some degree. It is difficult to separate physical from chemical effects on magnetic fabrics, nonetheless, research shows that strain alters magnetic fabric and can have effects such as deflecting the minimum susceptibility vector from vertical, and aligning the maximum eigenvector perpendicular to the axis of compression (see Figure 3c). Additionally, by working with sediments that have not experienced diagenesis from deep burial and heating, these chemical changes should be minimal.

AMS and slumping

Cronin et al. [2001] investigated a section of limestone in Italy to define the paleomagnetic field in the Cretaceous Normal Supercron. The paleomagnetic data displayed several intervals in which the direction deviated significantly from the expected normal direction. Such data are often interpreted as excursions of the geomagnetic field. In order to rule out slumping as a possible cause, they used AMS fabrics to characterize the "ordinary" and "deviant" intervals. The deviant intervals were triaxial, while the ordinary intervals were oblate. These results strongly suggest that the deviant directions were the result of "crypto-slumping", which is soft sedimentary slumping sub-parallel to bedding that leaves little to no visible record in the outcrop.

As suggested by *Rosenbaum et al.* [2000] and *Cronin et al.* [2001], it appears that even minor amounts of soft sediment deformation can have a profound effect on the paleomagnetic record. Such deformation, however, can be extremely difficult to detect based on visual observations alone, hence the term "crypto-slump" (*Schwehr and Tauxe* [2003]).

Schwehr and Tauxe [2003] pursued the idea that soft sediment deformation can be detected through the use of AMS by investigating both crypto-slumped sediments from a marine environment, along with the sediments from within and above the slump to confirm observations of *Cronin et al.* [2001]. They found a "crypto-slump" in a shale that can be traced laterally to a slumping event observed in the outcrop. Without the excellent exposure and lateral continuity along the outcrop, its slumped nature would not be easily detected. *Schwehr and Tauxe* [2003] then developed a test for post-depositional deformation based on the AMS characteristics of slumped versus undeformed sediments.

In essence, the test assesses whether the V_3 directions are vertical and distinct from V_1 and V_2, and whether the fabric is oblate (as expected for undisturbed sediment), or triaxial or prolate (as expected for disturbed fabrics). They used a statistical bootstrap approach to perform this test (see *Constable and Tauxe* [1990] and *Tauxe* [1998] for more details).

The example from *Schwehr and Tauxe* [2003] shows that AMS is able to distinguish between sedimentary structures and deformation in situations where field observations are ambiguous. However, the AMS bootstrapping technique developed by *Cronin et al.* [2001] and *Schwehr and Tauxe* [2003] may not be easily applicable to cores such as those collected in the Eel River Basin because of different compaction and deformation states. Bootstrapping conducted by *Cronin et al.* [2001] and *Schwehr and Tauxe* [2003] grouped samples into stratigraphic layers, however such sampling is not currently possible with today's coring technology. For each stratigraphic layer there may be different magnetic grain distributions and concentrations in addition to the possibility of different flow regimes and directions. We employ bootstrap statistics on sediment zones in this study, but the results should be used with caution.

AMS applied to the Humboldt Slide

The two alternative hypotheses for the formation of the Humboldt Slide deposit (slope failure and sediment waves) predict very different fabrics that can be measured using AMS. The deformational hypothesis of *Gardner et al.* [1999] predicts a triaxial fabric with the maximum axes of susceptibility (the V_1 eigenvectors) being either poorly grouped, perpendicular to the most compressive stress (see Figure 3c), or approximately North-South. The density current hypothesis of *Lee et al.* [2002] predicts oblate fabrics with the minimum axis of susceptibility (projected into the lower hemisphere) deflected in the direction of paleocurrent flow (see Figure 3b), or approximately westward. The center region of the core should display oblate AMS fabric if the features are depositional, whereas broad deformation will show dominantly triaxial fabric throughout.

Seismic data

Seismic lines covering the top half of the Humboldt Slide were acquired during August 1999 as part of the ONR STRATAFORM project (cruise TTN-096). The CHIRP seismic system (e.g. *Schock et al.* [1994]; *Quinn et al.* [1998]; *Gutowski et al.* [2002]) is a modified EdgeTech XStar system with an ADSL link from the fish to the topside computers. The data were collected with a 50 ms sweep from 1 to 6 kHz. The XStar SEG-Y records were processed with segy-py and SIOSEIS (*Henkart* [2005]), and were plotted with pltsegy. Figure 4 shows the section of the cruise data relevant to this study.

The Huntec data presented in Figure 5 were collected during August 1995 on cruise W-2-95-NC. The data were processed with a combination of Sonarweb and segy-py. A hydrophone (channel 2) is mounted on a tail behind the fish, which experienced a large amount of motion, so we processed only channel 1 (*Galway* [2000]). Huntec data from cruises W-2-95-NC and W-1-96-NC have been presented in *Gardner et al.* [1999] and *Lee et al.* [2002].

Coring

In November 2001, large-diameter piston cores were acquired using the Oregon State University Coring Facility onboard the R/V Thompson. The core sites were selected based on CHIRP seismic data (Figure 4) and on EM-1000 swath bathymetry (Figures 2). P-code differential GPS was used to locate the core sites and yielded 10 m, or better, accuracy of the core location. Core locations and lengths are summarized in Table 1. The lengths of the piston cores range from 5.9 to 7.8 m. The piston cores have an inner diameter of 10.2 cm which minimizes deformation associated with coring allowing undisturbed samples for AMS analysis to be acquired away from the liner effects.

Core 5 (Figures 2 and 6), collected north of the Humboldt Slide, serves as a control because it is located in an area with minimal deformation based on the seismic and bathymetric data. Core 5 was collected at a depth similar to that of cores 1, 2, and 7 and is located in the slope gullies (referred to as rills) described by *Spinelli and Field* [2001]. We predicted that the AMS results for the control core would show a normal sedimentary fabric, perhaps with a signature of current flow down or across slope (i.e., gravity sheet flows or slope-parallel contourites).

Cores 1, 2, and 7 were acquired in the primary study site within the Humboldt Slide (Figures 4 and 7-9). These cores sampled through the crest of one sedimentary structure located in the center of the Humboldt Slide at a water depth of 460 m. This feature has a wavelength of about 150 m and an amplitude of approximately 6 m. Given fish layback uncertainty (as marked in Figure 4), it is not possible to determine exactly where on these structures each core was acquired, however, it *is* clear that the three cores have sampled both the upslope and downslope components of the slide on feature c.

Paleomagnetics

From the cores, we collected 8 cm^3 paleomagnetic sample cubes with a typical sampling interval of 10 cm. The down core AMS measurements provide the

key data for interpreting the Humboldt Slide as either a retrogressive failure or a downslope current-controlled deposit (i.e., sediment waves) infilling a slide scar. Magnetic measurements were performed at the Scripps Paleomagnetic Laboratory. NRM measurements were conducted on 3-axis CTF and 2-G cryogenic magnetometers (designated Bubba and Flo respectively), located in a magnetically shielded room. Alternating Field (AF) demagnetizations were accomplished using an SI-4. After best fit directions for each sample were found, the Fisher statistics (*Fisher* [1953]) were applied to each core section to get a best fit declination ($\bar{D}$, Table 2). $\bar{D}$ was then applied to each core section such that the AMS eigenvectors are geographically oriented. AMS was measured on a Kappabridge KLY-2 using the same approach as is outlined in *Schwehr and Tauxe* [2003]. ARM acquisition was accomplished with a SI-4 using a 100 mT alternating field and a 40μT bias field. IRM's were imparted with an ASC impulse magnetizer with a field of 1 tesla.

A best fit tensor is derived from the 15 measurements made on the KLY-2 Kappabridge as a part of the AMS acquisition. A bulk susceptibility (χ_{bf}) is calculated, and the eigenvalues presented are normalized to sum to 1. To determine the fabric shape, we use the F statistics of *Hext* [1963] (see also *Tauxe* [1998]). The F test checks for overall significance of anisotropy. If F_{ij} is below the 95% threshold for significance, the eigenvalues τ_i and τ_j are considered indistinguishable. Isotropic samples fail the F_{12} and F_{23} tests, therefore, all three eigenvalues are indistinguishable (Figure 6: Shapes 1st sub-column - colored green). If the sample is anisotropic, then the F_{12} test checks for significance of the maximum and intermediate eigenvalues and F_{23} for the intermediate and minimum eigenvalues. Oblate samples (2nd sub-column - colored blue) have τ_2 and τ_3 that are significantly different, whereas prolate samples (3rd sub-column - colored yellow) have τ_1 and τ_3 being significantly different. If the sample passes both F_{12} and F_{23}, then all three eigenvalues are distinct and the sample is termed triaxial (4th sub-column - colored red).

The V_1 declination (D_{V_1}) shows the direction of the eigenvector associated with the maximum eigenvalue. This direction is only meaningful if the τ_1 eigenvalue is statistically distinguishable from τ_2. Therefore, the V_1 directions marked as prolate (cyan) and triaxial (red) in the Shapes column are significant. V_1 tends to be associated with the long axis of the magnetic grains. The V_3 inclination is meaningful when the fabric shape is either oblate or triaxial (τ_3 distinct from τ_2). The inclination of V_3 (I_{V_3}) is often used as a proxy for detection of bed rotation (e.g. *Rosenbaum et al.* [2000]; *Kanamatsu et al.* [2001]; *Housen and Kanamatsu* [2003]).

After magnetic measurements were made, the samples were wet sieved to remove the clay and fine and medium silt fraction using a 47μm screen. Finally, a range of grain size separates were sieved to determine silt, sand, and organic debris fractions; the organic debris included branches, twigs, seeds, etc.

Results

Cores 1, 2, and 7 were collocated with CHIRP seismic data to constrain the geometry and stratigraphy of the three prominent highs being studied (marked a-c in Figure 4). The seismic reflection data were used to determine where to sample the features because in certain areas the deformed features are mantled by a pelagic drape. The thickness of the drape varies systematically from the top of the slide complex to the base (Figure 5). At the top of the slide structure, there is little to no detectable pelagic drape overlying the deformed features at the locations of cores 1, 2, and 7 as observed in the CHIRP and Huntec seismic lines (Figures 4 and 5a). Examination of our core locations (Figure 4) and co-registered seismic data reveal that all three cores penetrated through any pelagic drape into the underlying sedimentary features.

The CHIRP system imaged faint seaward dipping reflectors with high-amplitude landward dipping reflectors. There is a marked asymmetry with the landward dipping sequences being much thicker than the seaward dipping units. In fact, across some features only the landward dipping sequences are observed with individual horizons outcropping at the sea floor on the seaward wall (Figure 4:a).

The first test to determine if post-deposition deformation occurred is to examine the NRM directions for evidence of rotation. The seaward and landward limbs of these features (Figure 4:a-c) exhibit a range of dips from 2.1° to 4.1° (Figure 4 inset table). Cores 1, 2 and 7 penetrate structure c which has a landward dip of 2.2° and a seaward dip of 4.1°. If there is E-W compression or rotation with a northerly fold axis, there should be a shallowing of approximately 0.5° in the NRM inclination compared to the expected geocentric axial dipole (GAD) inclination of 60.0°. Given that the α_{95} confidence values range from 8-26° (Table 2: cores 1, 2, and 7), such small rotations are below the resolution of this approach, and therefore, we must rely on the AMS technique for detecting post-depositional deformation.

The AMS results are shown in Figures 6-9. Core 5

(Figure 6) was collected as a control for this study and as such, it is located outside of the Humboldt Slide. Cores 1, 2, and 7 were acquired within the slide feature to access whether the sediment carapace has experienced rotation and deformation. Based on the observation of the AMS fabric observed in the cores, four distinct zones termed α, β, β', and γ were identified. Core 5 is used as the "type section" because it exhibits all four zones. Here we will describe the characteristics that define the four zones.

α - alpha

The first zone, α, is characterized by high susceptibility and high anisotropy observed in the AMS data. Individual samples exhibit a predominantly triaxial AMS fabric type with near-vertical orientation of the minor eigenvector (see Figures 6-9:I_{V_3}). The Hext (*Hext* [1963]) average inclination of V_3 for a group of samples is recorded in Table 3 as $\bar{I}$. The V_1 eigenvectors, as observed in the equal-area projection (Figure 10), have no preferred orientation (Figures 6-9:D_{V_1}). The confidence ellipses and best fits derived by bootstrap statistics for the different zones are reported in Table 3. The α zone is also characterized by large ARM, IRM and χ_{lf} (we plot only χ_{lf} in Figures 6-9). An increase in the coarse silt fraction correlates with the boundary between α and β' in core 2 (Figure 11:grain size). When plotting IRM verses χ_{lf}, the different zones can be delineated as shown in Figure 12. α exhibits high and transitional χ_{lf}, ARM, and IRM, whereas low χ_{lf}, ARM, and IRM, are characteristic of the other zones (Figure 12).

β' - beta prime

The β' zone is observed in cores 2 and 5 and is characterized by rotation of the V_3 eigenvectors away from vertical determined for the individual sample measurements (Figures 6 and 8: I_{V_3}). The deflection of V_3 away from the vertical is also observed in the equal area projections (Figure 13). A marked decrease in total anisotropy as evidenced by the eigenvalues is also characteristic of the β' zone. (Figures 6 and 8). V_1 exhibits slightly more grouping in β' than the in the overlying α zone, nevertheless a strong preferred orientation is not observed (Figure 13). The AMS fabrics for individual samples are predominately triaxial for the β' zone.

β - beta

Underlying the β' zone in cores 2 and 5, there is a pronounced shift to more oblate fabric for individual samples in the β zone. However, the transition from β' to β is not well defined by either the eigenvalues or χ_{lf}. In cores 2 and 5, the β zone is defined by near vertical V_3 orientation with tight clustering. Note that in core 7, even though the eigenvalues by sample show some scatter, the bootstrap vectors show a tight cluster near vertical (Figure 14).

In cores 1 and 7, β' is not observed and the α zone mantles β. When α directly overlies β, the zones are delineated by a marked shift in χ_{lf} (Figures 7 and 9). In core 7, a marked decrease in overall anisotropy appears to correlate with the boundary between α and β. In core 1, the decrease in overall anisotropy is more subdued for the transition between α and β (Figure 7). In the β zone, V_1 for all cores shows weak grouping, however there does not appear to be a preferred orientation for β. As mentioned before, β is characterized by low χ_{lf}, ARM, and IRM (Figures 11 and 12).

In all four cores, only small zones of bioturbation are observed. In general, the layering is clearly visible, and undisturbed as revealed by the core photos. The boundaries between layers are sharp, and mottling and smearing of layer boundaries is not commonly observed. A large number of organic-rich layers are clearly visible in the cores with a maximum thickness of 30 cm (core 2 from 568-589 cm for the vascular planet material deposit; Figure 6).

The core photos show a reciprocal relationship for the β zone and the occurrence of dark, organic-rich layers depending on whether the cores were acquired within or outside the slide region. Cores 1, 2, and 7 show an increase in occurrence and thickness of dark organic-rich layers in the β zone compared to the α zone. The dark organic-rich layers are comprised mostly of vascular plant matter (Figure 15). In core 5, the α, β', upper β zones are characterized by dark organic-rich layers, while the lower beta zone is largely devoid of such layers. In core 5, the thickest dark, organic-rich layers occur in the γ zone (Figure 6 and 16).

γ - gamma

The γ zone is only observed in core 5, which was acquired to the north of the Humboldt Slide. γ is characterized by a marked deflection of V_3 from vertical in both the individual and group samples (Figures 6 and 17). In core 5, the β zone above and below the γ zone is characterized by oblate fabric, with γ being predominately triaxial. The γ zone is indistinguishable from β based on χ_{lf}, eigenvalues, ARM and IRM. Within the γ zone, the sediments appear to show signs of post-depositional deformation as a dark, organic-rich horizon may have been folded (Figure 16: inset).

Discussion

In order to fully understand a marine slump, it is helpful to review the features that are typically expected. Figure 18 is a CHIRP seismic image of the Gaviota Slide from the Santa Barbara Basin that exhibits features typical for many slides and provides valuable insights for the expected sedimentary structures and morphology (*Schwehr et al.* [submitted]). For the Gaviota slide, the failed material has not moved far downslope with minimal translation from the evacuation to accumulation zone. If the failure is retrogressive in origin, then after initiation, the failure propagates upslope from the point of initial failure, and terminates at a head-wall scarp. Along the seaward extent of the slide complex, the toe often exhibits signs of compressional deformation (Figure 18). The V_1 eigenvalues showed a preferred orientation as a result of downslope compression (Figure 18:inset). Between the upper head-wall scarp and the toe, there is an evacuation zone, where the material has vacated, or a zone of thinned and extended material.

According to *Gardner et al.* [1999], the Humboldt Slide is thin skinned, however little or no accommodation zone for this slide is observed. This does not match the model for other slides where either a catastrophic failure mobilizes the sediment into a turbidity current, or sediment is removed from an evacuated zone to an accumulations zone downslope (Figure 18).

The morphology of the Humboldt Slide suggests minimal translation downslope because there is no downslope thickening or upslope thinning. Furthermore, the MCS data acquired across the region images individual layers that thicken and diverge toward the margin. The divergence of the horizons and the diminished dip up section may reflect long-term tectonic control in the region, suggesting fault-controlled accommodation (e.g., *Driscoll and Hogg* [1995]). Onlap and thinning are observed across the Little Salmon Anticline. *Lee et al.* [2002] presented numerous lines of evidence based on stratal geometry and morphology that the Humboldt Slide features were current-controlled bedforms. Nevertheless, based on the same internal geometry and morphology *Gardner et al.* [1999] argued that theses features are the consequence of post-depositional deformation. As previously mentioned, morphology is not unique and thus, the debate concerning the origin of these features continues. AMS measurements provide additional constraints on the origin of these features and are discussed below.

α - alpha

The high χ_{lf}, ARM and IRM characteristic of the α zone is different than the other underlying zones observed in the cores. Given that the high ARM and IRM values are only observed in the upper sections of the cores, Figures 11 and 12 suggest that the base of α is either (1) a diagenetic front delineating the top of the sulphate reduction zone, where biomediation consumes a fraction of the ferro magnetic grains; or (2) a mineralogical change reflecting a change in sediment discharge from the Eel River system. Diagenetic signatures in rock magnetic parameters (e.g. χ_{lf}, ARM, IRM) have been reported by numerous authors from a wide range of environments around the world (e.g. *Tarduno* [1994]; *Karlin* [1990b]; *Leslie et al.* [1990b]; *Liu et al.* [2004]; *Geiss et al.* [2004]; *Kumar et al.* [2005]; *Pan et al.* [2005]; *Riedinger et al.* [2005]; *Rowan and Roberts* [2006]). These transitions are typically attributed to a sulfate reduction in sediments that preferentially consume magnetites with large surface area to volume ratios (e.g., smaller grain size). *Karlin* [1990b] concluded that magnetic mineral diagenesis is likely to occur in rapidly deposited, sulfidic sediments. The process may shutdown after the initial reactions, not because of the complete removal of magnetite, but from the magnetites becoming covered in a protective coating of pyrite (*Egli* [2004]).

The ARM versus χ_{lf} bi-plots show that α zone is separate from the other zones that have moderate or low ARM and IRM values (Figure 12). *King et al.* [1983] reported that for a line passing through the origin and through a group of measurements on an ARM versus χ_{lf} plot (χ_{ARM} is a normalized form of ARM), the slope of the line is related to the size distribution of the magnetites in the samples. Steeper slopes are indicative of finer grained magnetites, whereas shallower slopes are evidence for coarser grained magnetites. If this relationship holds for the sediments in this study, then the most recently deposited sediments (the tops of the cores, α zone) have a finer grained fraction of magnetites than the underlying zones. These magnetites are consumed in the reaction front and are no longer present in the deeper sediments. This hypothesis implies that the finer grained magnetite population is situated in such a fashion as to generate a triaxial fabric. Below the diagenetic front where the finer-grained magnetites have been consumed, an oblate anisotropy is observed for the individual samples (Figures 6, 7, and 8). It is difficult to to explain why the fine-grained magnetites have such strong anisotropy and thus it is not our preferred hypothesis. Unfortunately, dissolution of the finer grained

fraction makes no prediction of the source of this easily reduced magnetite.

The second hypothesis is that α correlates with a shift in sediment provenance. There is a higher weight percent fraction of 63-300μm grains in the α zone with respect to the underlying zones (Figure 11). The Eel River area is undergoing a number of changes that could have caused such a shift. The shift may correlate with the 1955 transition to an increase in frequency of large floods on the Eel River and the widening of the Eel River channel observed by *Sloan et al.* [2001] and *Sommerfield et al.* [2002]. High flow conditions can cause sediments deposited to have triaxial fabrics (e.g. *Kopf and Berhman* [1997]), which may explain the triaxial samples in α. If the density flows associated with these floods exhibit different flow directions through the Humboldt slide amphitheater, then they might produce the signature observed in Figure 10 where the triaxial samples girdle the horizontal plane giving an overall group signature of oblate sediment fabric.

In rapidly depositing sediments, it is possible that the rate of deposition and sediment composition control the location of a diagenetic front. Therefore, we can not rule out the possibility that the local shift in the Eel River sediment delivery system may play a role in governing the location of the transition from high to low χ_{lf}, ARM, and IRM.

The results for the α zone show conflicting model interpretations based on that presented in Figure 3 and are difficult to interpret. The α zone bootstrap inclinations (Table 3:$\bar{I}$) range from 83.1° to 88.1°. This tight vertical V_3 implies quiet water deposition as illustrated in Figure 3a. Cores 2 and 5 show the strongest evidence for flow directions of 306° and 180° respectively based on V_3 $\bar{D}$ (Table 3).

On the other hand, with the majority of samples being triaxial, one might be tempted to classify the sediments as deformed based on the triaxial histogram shown in Figure 3c. It is important to distinguish the difference between sample level anisotropy (Figures 6-9) and group level anisotropy (Figure 3: bootstrapped eigenvalues). A group level bootstrap histogram tests for coherent deformation, whereas sample level anisotropy test for the statistical distinguishability of the eigenvectors for one specimen. A triaxial sample can imply a number of sediment histories including deformation or deposition under moderate flow conditions. Based on the observations, we interpret alpha to be indicative of deposition in moderate flow conditions.

β' - beta prime

The β' zone is only observed in cores 2 and 5 and is characterized by V_3 deviating from vertical. β' has relatively stable χ_{lf}, ARM, and IRM. The individual samples are predominantly triaxial, but there are several samples that are prolate. Nevertheless, the V_1 orientation shows no preferred direction in the bootstap. We interpret this to be moderate to strong flow conditions and core 2 may be on the apex of the feature which may have exposed this location to slightly greater currents and/or erosion. Conversely in core 5, the V_3 does not exhibit as much deflection, which may be indicative of more moderate flow. Core 2 sampled high flow conditions that appear to be centered on 325° (Table 3), which would be consistent with predicted flow directions. The observation that cores 1 and 7 do not exhibit β' zones implies that the β' zone observed in core 2 is a local feature with little lateral extent.

β - beta

The marked shift to more oblate sample and group shape fabric defines the β zone, which implies quiet water deposition. This conclusion is a bit surprising considering the size and frequency of large organic-rich layers within the zone (e.g. Figures 8:β and 15). This may be caused by how flows attach and detach from the bottom as they travel over an undulating sea floor.

This is the zone where the best evidence should be found for the deformation predicted by the slope failure model (*Gardner et al.* [1999]). The geometry observed in CHIRP and Huntec seismic data (Figures 4 and 5) predict thickening of 2:1 or greater on the upslope limbs. This amount of compression is expected to create fabric like that illustrated in Figure 3c. However, the eigenvectors plotted on stereonets with bootstrap eigenvectors for β most closely resemble Figure 3a. Core 7 is the least like Figure 3a, but the bootstrap eigenvectors are tightly clustered near vertical. The scatter in the eigenvectors can be traced to samples in 4 discrete regions located at ~167, 261-282, 420-430, and 572 cm. These layers with V_3 deflected from the vertical might correspond to periods of higher flow. Because the V_1 eigenvalues shows no preferred orientation for β in Core 7, it does not appear to be recording post-depositional deformation.

γ - gamma

γ stands out as the largest region of deflected V_3. The I_{V_3} has a saw toothed pattern indicating deformation that may not be coherent. This observation is

supported by visual inspection of the core photograph, which shows a folded organic-rich layer (Figure 16). Given the extent of the deformation, it is difficult to assess the direction of compression for this slump. The bootstrap $\bar{D}$ for V_1 is 330°, but this value has an associated ζ of 90°. However, the lack of preferred orientation of V_1 in the bootstrap test is consistent with highly deformed and folded sediment (e.g., recumbent folding). Such a deformation pattern exhibits fabrics in the AMS that are similar to deposition under moderate to high flow conditions. Note that γ looks very different from Figure 18 and much more like β' in core 2. Nevertheless, visual examination of the core indicates that the fabric is associated with folding and deformation (Figure 16).

The Humboldt Slide as a sediment wave field

We interpret the magnetic and sedimentological data presented here to indicate that there is little to no post-depositional deformation in the Humboldt Slide region. On the basis of the AMS data, we have identified four types of sediment. There is evidence for moderate to strong flow events and small crypto-slump events (usually occurring as a number of events in a restricted region). These crypto-slump events may represent periods of rapid sea level change, high sediment accumulation rates and loading, or increased seismic activity, but currently there is insufficient evidence to test these hypotheses.

The rill area to the north of the Humboldt Slide shows greater evidence for deformation in comparison to the material in the Humboldt Slide amphitheater. The overlying several meter sediment package may be creeping over the underlying sediments.

We observe no evacuation zone or downslope thickening toward the toe of the slide. The units observed in the MCS data (Figure 19a; described in *Burger et al.* [2003]) thin seaward down the slide. Individual layers exhibit divergence and thickening towards the margin that may reflect long-term tectonic control in the region (Figure 19b). The stratal geometry imaged in the MCS data is not consistent with the geometry predicted by the retrogressive failure model.

There is a geometric problem with this feature being interpreted as a slide deposit as it exhibits no thinning in the evacuation zone and no thickening in the accumulation zone. This implies that all deformation is accommodated by in-situ rotation and thickening of beds, with little to no translation. We are unable to identify any signature of such processes beyond occasional thin layers that appear to be deposited in moderate to high flow conditions. The orientation of the V1 eigenvalues are not suggestive of post-depositional deformation as observed in the Gaviota Slide region (Figure 18).

These observations support the hypothesis that these features are sediment waves with preferential deposition on the upslope limbs. The sediment waves are composed of both hemipelagic deposits and event beds. Near the base of core 1, 2, and 7, (Figures 7-9) there is an increase in frequency and thickness of layered units down-core. Wood and plant material occurs more frequently down core with some layers being >20 cm thick. This suggests a change in the style and/or type of flood deposits as compared to the present.

Conclusions

The main results of our rock magnetic and seismic reflection study are summarized as follows:

1. The upper ~8 m of the Humboldt Slide sediments are not undergoing post-depositional deformation and folding.
2. The upper section sampled in this study appears to be the result of primary deposition and thus we interpret the features to be downslope current-controlled bedforms.
3. Based on MCS data, the thickness and dip of the subsurface sequences are not consistent with the features being a slide deposit. The sediment structures within the Humboldt Slide appear to be sediment waves that may mantle an older slide.
4. We identified a ~1 m thick slump layer located to the north of the Little Salmon Anticline in the region with extensive rills.
5. The change in how much and what fraction of material is delivered to the Humboldt Slide area (versus that north of the Little Salmon Anticline and down the Eel Canyon to the south) may have undergone a recent shift caused by the increasing frequency of combined large storm and flood events from 1955 to the present. This possibility requires further research.

Magnetic measurements allow us to test between the alternative hypotheses of slope failure, and sediment waves for the origin of the Humboldt Slide. Specifically, we are able to discern whether the morphology and internal geometry results from soft-sediment deformation and retrogressive slumping, or downslope current-controlled deposition. The former predicts a triaxial

AMS fabric with essentially north-south oriented maximum axes (Figure 3c); the latter predicts an oblate fabric with a possible westward deflection of the minimum axes (Figure 3a,b).

The morphology and internal architecture of the Humboldt Slide are not unique; there are numerous examples along other continental margins with similar morphology and ongoing debates regarding their origin (see examples in *Lee et al.* [2002]). Magnetic methods for the detection of post-depositional deformation provides a new approach to determine the origin of such features on other continental margins.

Acknowledgments

We would like to thank NSF (grant OCE-04-25919), ONR (grant N00014-03-1-0272), and CalIT^2 for funding this research. Additionally we appreciate the support of the crew of the R/V Thompson, the OSU Coring Group, the Nittrouer lab and the SIO Geologic Collections. J. Borgeld and his students from Humboldt State University for helping out with the cruise. H. J. Lee and J. Gardner for numerous comments and discussions. J. Gardner provided support in processing the Huntec seismic data. The MCS images (IDs: 4213 and 4226) were acquired from *http* : *//www.ig.utexas.edu/sdc/cruise.php?cruiseIn = w9605b*, courtesy of C. Fulthorpe and G. Mountain.

References

Alexander, C. R., and A. M. Simoneau, Spacial variability in sedimentary processes on the Eel continenal slope, *Marine Geology*, *154*, 243–254, 1999.

Banerjee, S. K., J. King, and J. Marvin, A rapid method for magnetic granulometry with applications to environmental studies, *Geophys. Res. Lett.*, *8*, 333–336, 1981.

Booth, J., D. O'leary, P. Popenoe, and W. Danforth, U.S. Atlantic continental slope landslides: Their distribution, general attributes, and implications, *US Geological Survey Bulletin*, *2002*, 14–22, 1993.

Brooks, T., and K. Johnson, Final Report, Phase 3 and Phase 4 Seismic Program, Ownes Lake, Inyo Country, California, p. 146, 1997.

Burger, R. L., C. S. Fulthorpe, and J. A. Austin, Jr., Effects of triple junction migration and glacioeustatic cyclicity on evolution of upper slope morphologies, offshore Eel River Basin, northern California, *Marine Geology*, *199*, 307–336, 2003.

Christie-Blick, N., and N. Driscoll, Sequence Stratigraphy, *Annual Review of Earth and planetary Sciences*, *23*, 451–478, 1995.

Clarke, S. J., Geology of the California continental margin north of Cape Mendocino, in *Geology and Resources Ptential of the Continental Margin of Western North America and Adjacent Ocean Basins - Beufort Sea to Baja California*, edited by D. Scholl, A. Grantz, and J. Vedder, vol. 6 of *Earth Science Series*, pp. 337–351, Circum-pacific Council for Energy and Mineral Resources, 1987.

Constable, C., and L. Tauxe, The bootstrap for magnetic susceptibility tensors, *J. Geophys. Res.*, *95*, 8383–8395, 1990.

Couch, R., Seismicity and crustal structure near the north end of the San Andreas Fault system, in *Studies of the San Andreas Fault Zone in northern California*, edited by R. Streitz and R. Sherbourne, vol. 190 of *Special Reports*, pp. 13–30, Calif. Div. Mines Geol., 1980.

Cronin, M., L. Tauxe, C. Constable, P. Selkin, and T. Pick, Noise in the quiet zone, *Earth Planet. Sci. Lett.*, *190*, 13–30, 2001.

Dillon, W., M. Lee, K. Fehlhaber, and D. Coleman, Gas hydrates on the Atlantic continetal magin of the United States–controls on concentration, in *The future of energy gasses*, edited by d. Howell, vol. 1570 of *US Geological Survey Professional Paper*, pp. 313–330, 1993.

Dodds, D. J., Attenuation Estimates from High Resolution Subbottom Profiler Echoes, in *Saclant Asw Research Conference on Ocean Acoustics Influienced by the Sea Floor*, vol. 907, p. 19, Plenum Press, La Spezia, Italy, 1980.

Driscoll, N., and J. Diebold, Tectonic and stratigraphic development of the Caribbean: New constraints from multichannel seismic data, in *Caribbean Basins. Sedimentary Basins of the World*, edited by P. Mann, vol. 4, pp. 591–627, Elsevier Science B. V., Amsterdam, 1999.

Driscoll, N., and E. Laine, Abyssal Circulation Influence on the Southwest Bermuda Rise and Surrounding Region, *Marine Geology*, *130*, 231–263, 1996.

Driscoll, N. W., and J. R. Hogg, Stratigraphic response to basin formation: Jeanne d'Arc Basin, off shore Newfoundland, *Geological Society Special Publication*, *80*, 1995.

Egli, R., Characterization of individual rock magnetic components by analysis of remanence curves. 3. Bacterial magnetite and natural processes in lakes,

Physics and Chemistry of the Earth, *29*, 869–884, 2004.

Eichhubl, P., H. G. Greene, and N. Maher, Physiography of an active transpressive margin basin: high-resolution bathymetry of the Santa Barbara basin, Southern California continental borderland, *Marine Geology*, *184*, 95–120, 2002.

Embley, R., and R. Jacobi, Mass wasting in the western North Atlantic, in *The Western North Atlantic region*, edited by P. Vogt and B. Tucholke, vol. M, pp. 479–490, Boulder Colorado, Geological Society of America, 1986.

Evans, D., E. King, N. Kenyon, C. Brett, and D. Wallis, Evidence for long-term instability in the Storrega Slide region off western Normay, *Marine Geology*, *130*, 281–292, 1996.

Field, M., and J. Barber, A submarine landslide associated with shallow sea-floor gas and gas hydrates off northern California, in *Submarine Landslides: Selected Studies in the U.S. Exclusive Economic Zone*, edited by W. Schwab, H. Lee, and D. Twitchell, vol. 2002 of *Unites States Geological Survey Bulletin*, 1993.

Fisher, R. A., Dispersion on a sphere, *Proc. Roy. Soc. London, Ser. A*, *217*, 295–305, 1953.

Flood, R., Deep sea sedimentary morphology: Modelling and inerpretation of echo-sounding profiles, *Marine Geology*, *38*, 77–92, 1980.

Galway, R. S., The Integration of Multibeam Sonar Data with Huntec Sub-bottom Profile Data into a Marine GIS, Masters of science in engineering, University of New Brunswick, 2000.

Gardner, J., D. Prior, and M. Field, Humboldt Slide - a large shear-dominated retrogressive slope failure, *Marine Geology*, *154*, 323–338, 1999.

Geiss, C. E., S. K. Banerjee, P. Camill, and C. E. Umbanhowar, Sediment-magnetic signature of land-use and drought as recorded in lake sediment from south-central Minnesota, USA, *Quaternary Research*, *62*, 117–125, 2004.

Glen, J., and R. Coe, Paleomagnetism and magnetic susceptibility of Pleistocene sediments from drill hole OL-92, Owens Lake, California, in *An 800,000-year Geologic and Climatic record from Owens Lake, California: Core OL-92*, edited by G. Smith and J. Bischoff, pp. 67–78, Geological Society of America, 1997.

Gutowski, M., J. M. Bull, T. Henstock, J. K. Dix, P. Hogarth, T. Leighton, and P. White, Chirp sub-bottom profiler source signature design and field testing, *Marine Geophysical Researches*, *23*, 481–492, 2002.

Heezen, B. C., and C. D. Hollister, Deep-sea current evidence from abyssal sediments, *Marine Geology*, *1*, 141–174, 1964.

Henkart, P., SIOSIES, p. http://sioseis.ucsd.edu, 2005.

Hext, G. R., The extimation of second-order tensors, with related tests and designs, *Biometrika*, *50*, 353–357, 1963.

Holbrook, W., Seismic Studies of the Blake Ridge: implications for Hydrate Distribution, Mathane Expulsion, and Free Gas Dynamics, in *Natural Gas Hydrates: Occurrence, Distribution, and Detection*, edited by C. Paull and W. Dillon, vol. 124 of *Geophysical Monograph*, AGU, 2001.

Holbrook, W., D. Lizarralde, I. Pecher, A. Gorman, K. Hackwith, M. Hornbach, and D. Saffer, Escape of methane gas through sediment waves in a large methane hydrate province, *Geology*, *30*, 467–470, 2002.

Housen, B. A., and T. Kanamatsu, Magnetic fabrics from the Costa Rica margin: sediment deformation during the initial dewatering and underplating process, *Earth Planet. Sci. Lett.*, *206*, 215–228, 2003.

Housen, B. A., C. Richter, and B. van der Pluijm, Composite magnetic anisotropy fabrics: experiments, numerical models, and implications for the quantification of rock fabrics, *Tectonophys.*, *220*, 1–12, 1993.

Housen, B. A., et al., Strain decoupling across the decollement of the Barbados accretionary prism, *Geology*, *24*, 127–130, 1996.

Hrouda, F., and L. Hruskova, On the detection of weak strain parallel to the bedding by magnetic anisoropy: a mathematical model study, *Studia Geophys. et geol.*, *34*, 327–341, 1990.

Ising, G., On the magnetic properties of varved clay, *Arkiv. For. Mate., Astr., Och Fys.*, *29*, 1–37, 1942.

Kanamatsu, T., E. Herrero-Bervera, and A. Taira, Magnetic fabrics of soft-sediment folded strata within a Neogene accretionary complex, the Miura group, central Japan, *Earth Planet. Sci. Lett.*, *187*, 333–343, 2001.

Karlin, R., Magnetic mineral diagenesis in suboxic sediments at Bettis Site W-N, NE Pacific Ocean, *J. Geophys. Res.*, *95*, 4421–4436, 1990a.

Karlin, R., Magnetite Diagenesis in Marine Sediments From the Oregon Continental Margin, *J. Geophys. Res.*, *95*, 4405–4419, 1990b.

Kawamura, K., and Y. Ogawa, Progressive change of pelagic clay microstructure during burial process; examples from piston cores and ODP cores, *Marine Geology*, *207*, 131–144, 2004.

King, J., S. K. Banerjee, J. Marvin, and O. Ozdemir, A comparison of different magnetic methods for determining the relative grain size of magnetite in natural materials: some results from lake sediments, *Earth Planet. Sci. Lett.*, *59*, 44–419, 1982.

King, J., S. K. Banerjee, and J. Marvin, A new rock-magnetic approach to selecting sediments for geomagnetic paleointensity studies: application to paleointensity for the last 4000 years., *J. Geophys. Res.*, *88*, 5911–5921, 1983.

Kopf, A., and J. H. Berhman, Fabric Evolution and Mechanisms of Diagenesis in Fine-Grained Sediments from the Kita-Yamato Trough, Japan Sea, *Journal of Sedimentary Research*, *67*, 590–600, 1997.

Kumar, A. A., V. P. Rao, S. K. Patil, P. M. Kessarkar, and M. Thamban, Rock magnetic records of the sediments of the eastern Arabian Sea: Evidence for late Quaternary climatic change, *Marine Geology*, *220*, 59–82, 2005.

Laine, E., W. Gardner, M. Richardson, and M. Kominz, Abyssal currents and advection of resuspended sediment along the northeastern Bermuda Rise, *Marine Geology*, *119*, 159–171, 1994.

Lee, H. J., J. P. M. Syvitski, G. Parker, D. Orange, J. Locat, E. W. H. Hutton, and J. Imran, Distinguishing sediment waves from slope failure deposits: field examples, including the "Humboldt slide", and modelling results, *Marine Geology*, *192*, 79–104, 2002.

Leslie, B. W., D. E. Hammond, W. M. Berelson, and S. P. Lund, Diagenesis in anoxic sediments from the California continental borderland and its influence on iron, sulfur, and magnetite behavior, *J. Geophys. Res.*, *95*, 4453–4470, 1990a.

Leslie, B. W., S. P. Lund, and D. E. Hammond, Rock magnetic evidence for the dissolution and authigenic growth of magnetic minerals within anoxic marine sediments of the California continental borderland, *J. Geophys. Res.*, *95*, 4437–4452, 1990b.

Liu, J., R. Zhu, A. P. Roberts, S. Li, and J.-H. Chang, High-resolution analysis of early diagenetic effects on magnetic minerals in post-middle-Holocene continental shelf sediments from the Korea Strait, *J. Geophys. Res.*, *109*, doi:10.1029/2003JB002,813, 2004.

Lonsdale, P., and F. Spiess, Abyssal bedforms explored with a deeply towed instrument package, *Marine Geology*, *23*, 57–75, 1977.

Marino, R., and B. Ellwood, Anomalous magnetic fabric in sediments which record an apparent geomagnetic field excursion, *Nature*, *274*, 581–582, 1978.

Milliman, J., and P. Syvitski, Geomorphic/tectonic control of sediment transport to the ocean: the importance of small mountainous rivers, *J. Geology*, *100*, 525–544, 1992.

Nittrouer, C., STRATAFORM: Overview of its design and synthesis of its results, *Marine Geology*, *154*, 3–12, 1999.

Owens, W. H., Mathematical model studies on factors affecting the magnetic anisotropy of deformed rocks, *Tectonophys.*, *24*, 115–131., 1974.

Pan, Y., N. Petersen, A. F. Davila, L. Zhang, M. Winklofer, Q. Liu, M. Hanzlik, and R. Zhu, The detection of bacterial magnetite in recent sediments of Lake Chiemsee (southern Germany), *Earth Planet. Sci. Lett.*, *232*, 109–123, 2005.

Pares, J., B. van der Pluijm, and J. Dinares-Turell, Evolution of magnetic fabrics during incipient deformation of mudrocks (Pyreness, northern Spain), *Tectonophysics*, *307*, 1–14, 1999.

Pratson, L. F., and B. J. Coakley, A model for the headward erosion of submarine canyons induced by downslope eroding sediment flows, *Geological Society of America Bulletin*, *108*, 225–234, 1996.

Quinn, R., J. M. Bull, and J. K. Dix, Optimal processing of marine high-resolution seismic reflection (Chirp) data, *Marine Geophysical Researches*, *20*, 13–20, 1998.

Rees, A., Experiments on the production of transverse grain alignment in a sheared dispersion, *Sedimentology*, *30*, 437–448, 1983.

Rees, A. I., The effect of water currents on the magnetic remanence and anisotropy of susceptibility of some sediments, *Geophys. J. R. Astr. Soc.*, *6*, 235–251, 1961.

Rees, A. I., and W. A. Woodall, The magnetic fabric of some laboratory deposited sediments, *Earth Planet. Sci. Lett.*, *25*, 121–130, 1975.

Riedinger, N., K. Pfeifer, S. Kasten, J. F. L. Garmin, C. Vogt, and C. Hensen, Diagenetic Alteration of Magnetic Signals by Anaerobic Oxidation of Methane Related to a Change in Sedimentation Rate, *Geochimica et Cosmochimica Acta*, *69*, 4117–4126, 2005.

Rosenbaum, J., R. Reynolds, J. Smoot, and R. Meyer, Anisotropy of magnetic susceptibility as a tool for recognizing core deformation: reevaluation of the paleomagnetic record of Pleistocene sediments from

drill hole OL-92, Owens Lake, California, *Earth Planet. Sci. lett.*, *178*, 415–424, 2000.

Rowan, C. J., and A. P. Roberts, Magnetite dissolution, diachronous greigite formation, and secondary magnetizations from pyrite oxidation: Unravelling complex magnetizations in Neogene marine sediments from New Zealand, *Earth Planet. Sci. Lett.*, *241*, 119–137, 2006.

Schock, S. G., L. R. LeBlanc, and S. Panda, Spatial and temporal pulse design considerations for a marine sediment classification sonar, *IEEE Journal of Oceanic Engineering*, *19*, 406–415, 1994.

Schwehr, K., and L. Tauxe, Characterization of soft sediment deformation: dectection of crypto-slumps using magnetic methods, *Geology*, 2003.

Schwehr, K., L. Tauxe, N. Driscoll, and H. Lee, Detecting Compaction Disequilibrium with Anisotropy of Magnetic Susceptibility, *Geochem., Geophys., Geosyst.*, *??*, ??, submitted.

Sloan, J., J. R. Miller, and N. Lancanster, Response and recovery of the Eel River, California, and its tributaries to floods in 1955, 1964, and 1997, *Geomorphology*, *36*, 129–154, 2001.

Sommerfield, C., and C. Nittrouer, Modern accumulation rates and a sediment budget for the Eel shelf: A flood dominated depositional environment, *Marine Geology*, *154*, 227–242, 1999.

Sommerfield, C., D. E. Drake, and R. A. Wheatcroft, Shelf record of climatic changes in flood magnitude and frequency, north-coastal California, *Geology*, *30*, 395–398, 2002.

Spinelli, G., and M. Field, Evolution of continental slope gullies on the northern California margin, *Journal of Sedimentary Research*, *71*, 237–245, 2001.

Tarduno, J. A., Temporal trends of magnetic dissolution in the pelagic realm: Gauging paleoproductivity?, *Earth Planet. Sci. Lett.*, *123*, 39–48, 1994.

Tarling, D. H., and F. Hrouda, *The Magnetic Anisotropy of Rocks*, Chapman and Hall, London, 1993.

Tauxe, L., *Paleomagnetic Principles and Practice*, Klewer Academic Publishers, 1998.

Tauxe, L., H. Bertram, and C. Seberino, Physical interpretation of hysteresis loops: Micromagnetic modelling of fine particle magnetite, *Geochem., Geophys., Geosyst.*, *3*, DOI 10.1029/ 2001GC000,280, 2002.

Trincardi, F., A. Cattaneo, A. Correggiari, and D. Ridente, Evidence of soft sediment deformation, fluid escape, sediment failure and regional weak layers within the late Quaternary mud deposits of the Adriatic Sea, *Marine Geology*, *213*, 91–119, 2004.

Wheatcroft, R. A., and C. Sommerfield, River sediment flux and shelf sediment accumulation rates on the Pacific Northwest margin, *Continental Shelf Research*, *25*, 311–332, 2005.

K. Schwehr*, Scripps Institution of Oceanography, La Jolla, CA 92093-0220, USA (e-mail: schwerhr@gmail.com); N. Driscoll, Scripps Institution of Oceanography, La Jolla, CA 92093-0220, USA (e-mail: ndriscoll@ucsd.edu); L. Tauxe, Scripps Institution of Oceanography, La Jolla, CA 92093-0220, USA (e-mail: ltauxe@ucsd.edu); * New Address: Center for Coastal and Ocean Mapping, Chase Ocean Engineering Lab, 24 Colovos Road, Durham, NH 03824, (e-mail: schwehr@ccom.unh.edu)

Core	Latitude	Longitude	Depth (m)
1	124° 30” 09.96’ W	40° 50” 20.16’ N	460
2	124° 30” 07.62’ W	40° 50” 19.86’ N	460
5	124° 27” 12.08’ W	40° 59” 00.30’ N	419
7	124° 30” 05.84’ W	40° 50” 19.87’ N	461

Table 1. Cores 1, 2, and 7 were collected in the center of the Humboldt Slide. Core 5 was collected to the North of the slide.

Core	Section	$\bar{D}$	$\bar{I}$	N	R	κ	α_{95}	Depth (cm)
1	1	217.2	67.5	6	5.3555	7	25.7	69
1	2	335.6	56.3	12	11.4192	18	10.2	216
1	3	319.3	49.5	12	10.8026	9	15.1	363
1	4	338.6	55.4	12	11.4111	18	10.3	508
2	1	85.0	58.7	4	3.9492	59	12.1	62
2	2	322.7	70.8	13	12.5929	29	7.8	209
2	3	279.3	62.0	11	10.4484	18	11.0	358
2	4	251.1	64.3	9	8.8349	48	7.5	507
2	5			0				525
2	6	293.5	68.0	5	4.8824	34	13.3	642
2	7	124.8	49.2	7	6.8468	39	9.8	783
5	1	132.1	36.8	13	12.8963	115	3.9	57
5	2	208.2	49.9	19	16.8045	8	12.5	207
5	3	225.9	49.9	3	2.9145	23	26.1	356
5	4	220.9	68.8	3	2.9699	66	15.2	505
5	5	254.9	66.8	7	4.7290	02	46.4	624
7	1	17.6	58.1	5	4.8088	20	17.1	87
7	2	39.7	63.5	7	6.7688	25	12.1	182
7	3	38.2	71.3	13	12.0803	13	11.9	330
7	4	67.8	58.5	13	11.5771	8	15.2	481
7	5			0				502
7	6	214.1	63.7	10	9.1058	10	16.0	610
7	7	224.8	57.4	8	7.7080	23	11.5	755

Table 2. Fisher statistics (*Fisher* [1953]) of alternative frequency (AF) demagnetization of the natural remanent magnetization (NRM) listed by core sections. The declination is in the core section local frame before reorientation to geographic north. Based on a Geocentric Axial Dipole (GAD) model, the expected inclination for these cores is 60.0°. $Note:$ $\bar{D}$ is mean declination; $\bar{I}$ is mean inclination; N is number of specimens; R is the length of resultant vector; κ is the *Fisher* [1953] precision parameter; and α_{95} is the estimate of the circle of 95% confidence. The α_{95} values are too large to detect rotations smaller than 4.1° (2.1 - 4.1° observed in CHIRP seismic data - Figure 4). Depth is the distance below the core top to the bottom of the core section.

Core	Zone	V	$\bar{D}$	$\bar{I}$	η	D_η	I_η	ζ	D_ζ	I_ζ
1p	α	V_1	191.3	1.7	4.4	78.0	85.6	90.0	281.5	4.0
2p	α	V_1	169.1	5.1	9.0	309.9	83.5	90.0	78.7	4.1
5p	α	V_1	296.0	2.7	5.9	179.3	84.0	90.0	26.3	5.4
7p	α	V_1	213.4	1.9	10.3	355.8	87.7	77.5	123.3	1.4
1p	α	V_3	81.9	84.8	3.3	172.2	0.0	4.8	262.2	5.2
2p	α	V_3	306.1	83.1	6.3	86.6	5.4	7.5	177.0	4.4
5p	α	V_3	180.0	83.9	5.0	304.9	3.5	6.0	35.2	5.0
7p	α	V_3	18.5	88.1	9.2	198.1	1.9	10.8	288.1	0.0
2p	β'	V_1	154.8	24.4	40.0	316.6	64.5	90.0	61.6	7.0
5p	β'	V_1	52.3	3.6	23.3	302.6	79.3	90.0	142.9	10.0
2p	β'	V_3	325.1	65.3	40.7	155.3	24.4	90.0	63.5	3.9
5p	β'	V_3	302.5	79.4	16.5	89.4	8.9	21.0	180.3	5.7
1p	β	V_1	271.0	2.5	5.6	70.1	87.3	90.0	181.0	1.0
2p	β	V_1	154.3	11.4	9.3	353.5	78.0	90.0	245.1	3.8
5p	β	V_1	25.2	1.4	5.4	270.4	86.7	90.0	115.3	3.0
7p	β	V_1	161.9	0.0	7.6	252.0	83.9	74.6	71.9	6.1
1p	β	V_3	71.3	87.4	4.7	222.5	2.3	5.4	312.6	1.3
2p	β	V_3	347.7	78.3	8.5	171.8	11.7	9.0	81.6	0.8
5p	β	V_3	266.0	87.2	4.2	72.5	2.8	4.8	162.5	0.7
7p	β	V_3	252.0	84.6	6.8	343.2	0.1	8.3	73.3	5.4
5p	γ	V_1	329.8	0.5	40.8	236.7	80.7	90.0	59.9	9.3
5p	γ	V_3	233.2	85.5	36.3	138.3	0.4	42.5	48.3	4.5

Table 3. Bootstrap statistics for each zone type. η and ζ are the angle of major and minor axis for the ellipse of 95% confidence. D_η and I_η are the major axis direction, whereas D_ζ and I_ζ are the minor axis direction.

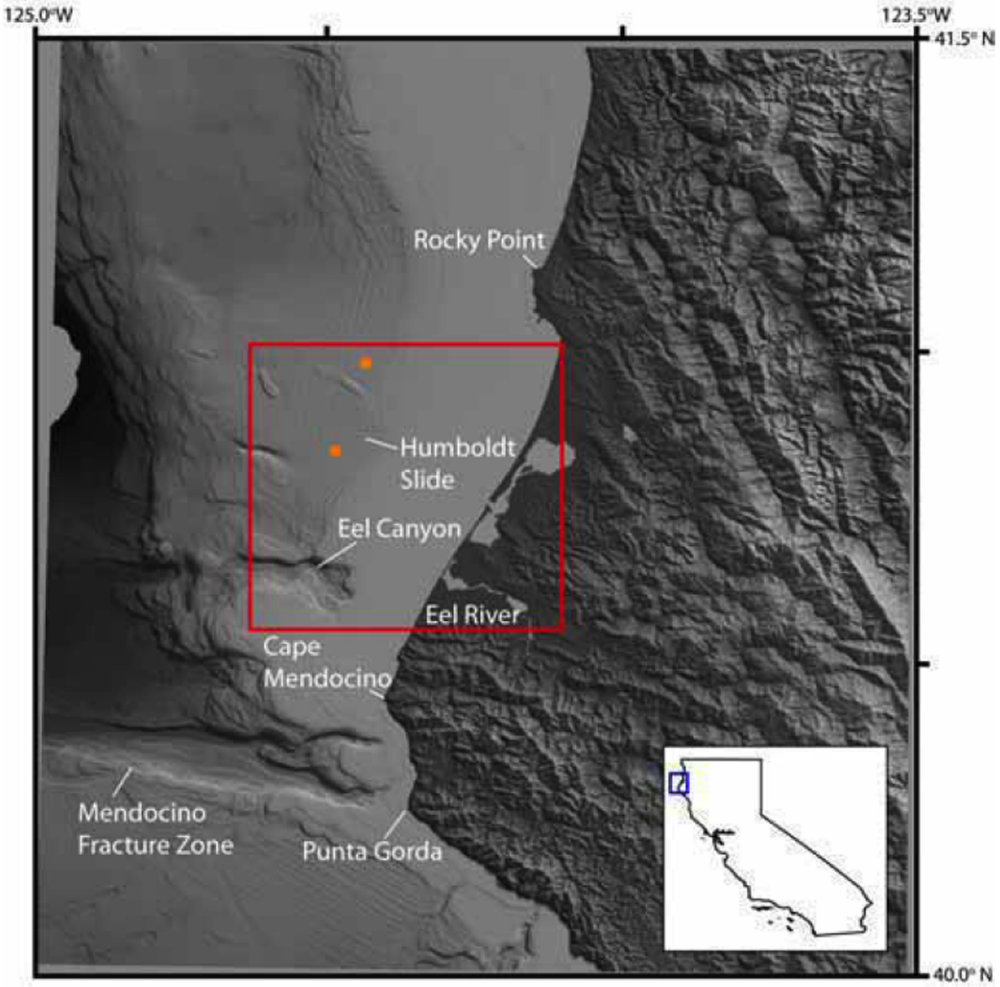

Figure 1. The Eel River Basin is located in Northern California, just north of the Mendocino Triple Junction. The Eel River enters the ocean south of Humboldt Bay. The slide is bounded by the Little Salmon Fault Zone to the north, the Eel Canyon to the south and up dip is delineated by the shelf break. The bathymetry is a compilation of the STRATAFORM EM1000, MBARI EM300 and the NOAA coastal relief 3 second data. The red inset shows the location of the study area (Figure 2) with the core locations marked with orange circles.

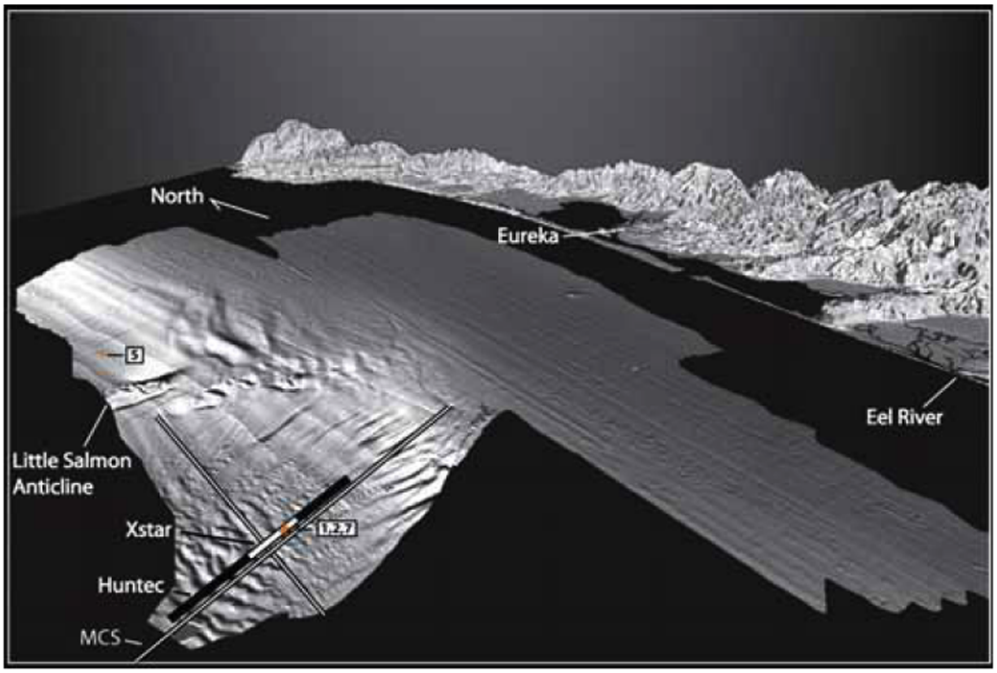

Figure 2. Location of XStar CHIRP (Figure 4), Huntec (Figure 5), and multi-channel seismic (MCS; Figure 19) lines on the Humboldt Slide amphitheater. The core locations are marked with orange dots. Cores 1, 2 and 7 are coincident with the Chirp, Huntec, and MCS E-W lines. Core 5, which was acquired outside of the Humboldt Slide, was used as a control core for the study. Image courtesy United States Geological Survey.

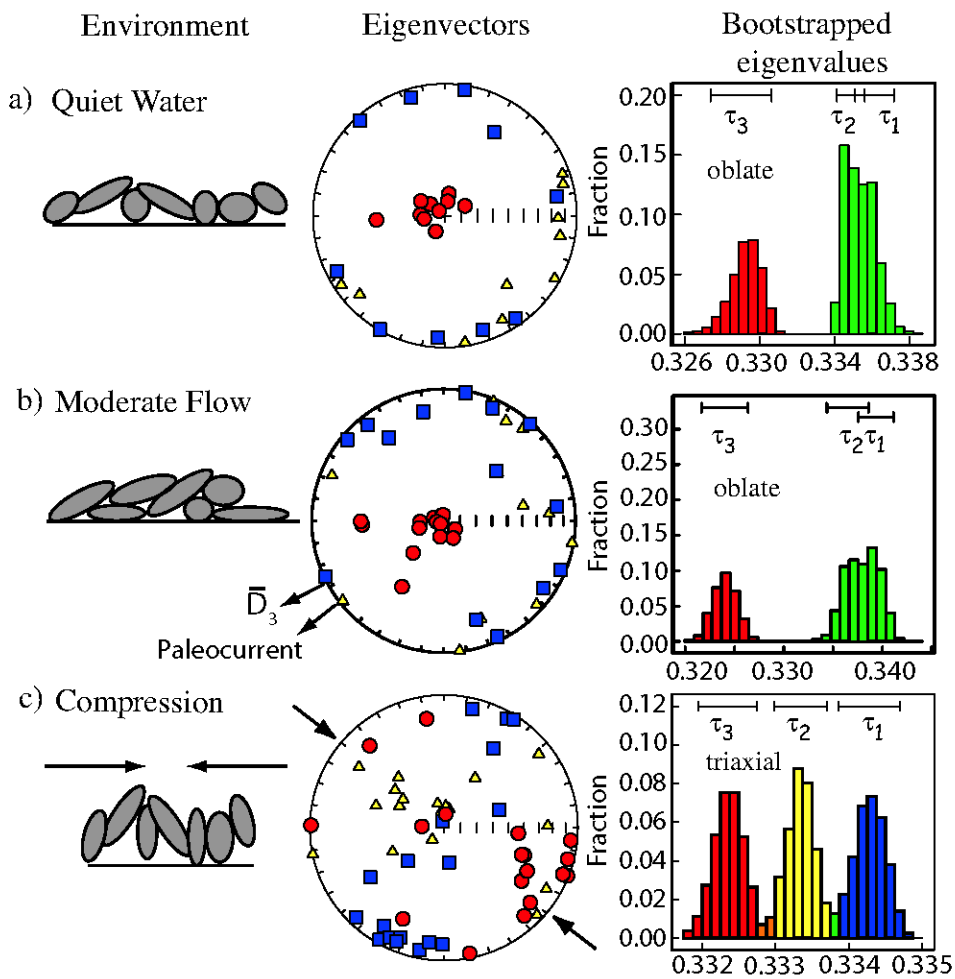

Figure 3. Schematic diagram illustrating development of sedimentary magnetic anisotropy fabric. Eigenvector directions are plotted in the equal area projections whereby circles are the directions V_3 associated with the minimum eigenvalue τ_3, triangles are V_2 associated with τ_2 and squares are the directions V_1 associated with the maximum eigenvalue τ_1. The histograms to the right are bootstrapped eigenvalues for the specimens showing the 95% confidence intervals for τ_1, τ_2, τ_3. a) Quiet water: the V_3 directions are typically vertical and τ_1 and τ_2 are not significantly different (i.e., the fabric is oblate). b) Moderate flow: the V_3 directions are deflected from the vertical by the current, but the fabric is still typically oblate. The bootstrap mean declination for V_3 ($\bar{D}_3$) is the inferred direction of flow, which closely approximates the paleocurrent direction measured from ripples (from *Schwehr and Tauxe* [2003]). c) Uniaxial horizontal deformation: the eigenvalues will be significantly different (i.e., the fabric is triaxial). In extreme cases, the V_3 directions will ultimately become horizontal. Arrows show the direction of compression that is orthogonal to the V_1 orientation.. Note that scales vary for the histograms.

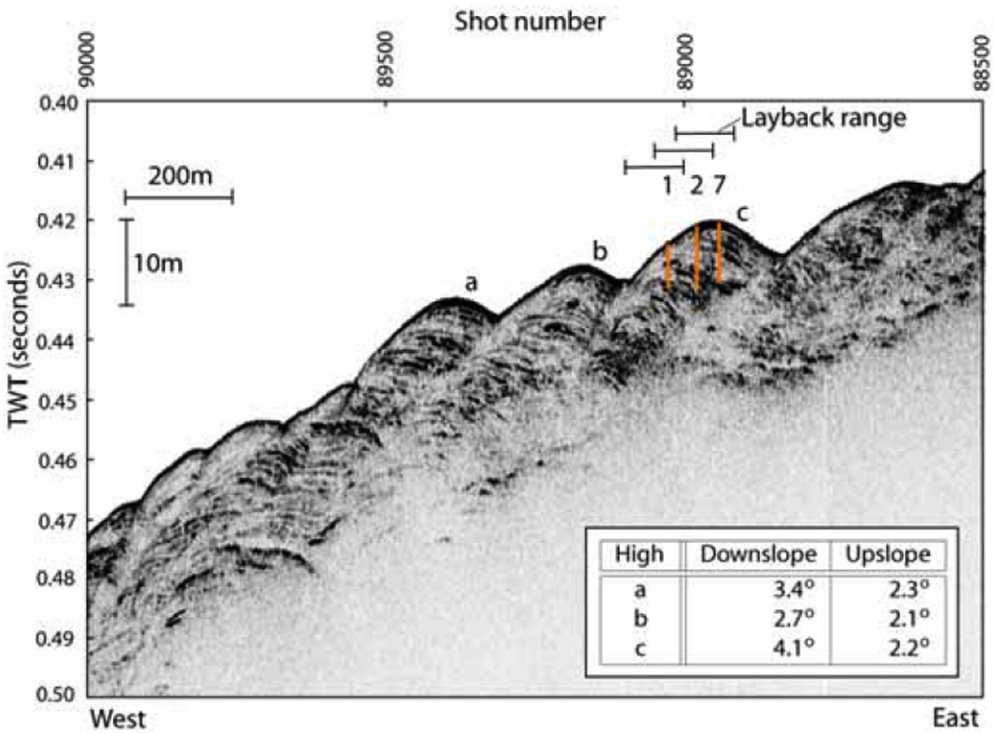

Figure 4. EdgeTech XStar CHIRP seismic line collected in 1999 (See Figure 2). This 1681 m long line trends NW-SE and images three prominent highs with internal reflectors (labeled a-c). Two way travel time is in seconds. Layback is calculated using wire angle and fish depth. The error bars are shown for wire angles ranging from 30-45° with the cores located at a wire angle of 35°, which is why the error bars are not symmetric with respect to the cores. The inset table shows the downslope and upslope dip angles of the three prominent highs that are labeled a-c on the CHIRP seismic line.

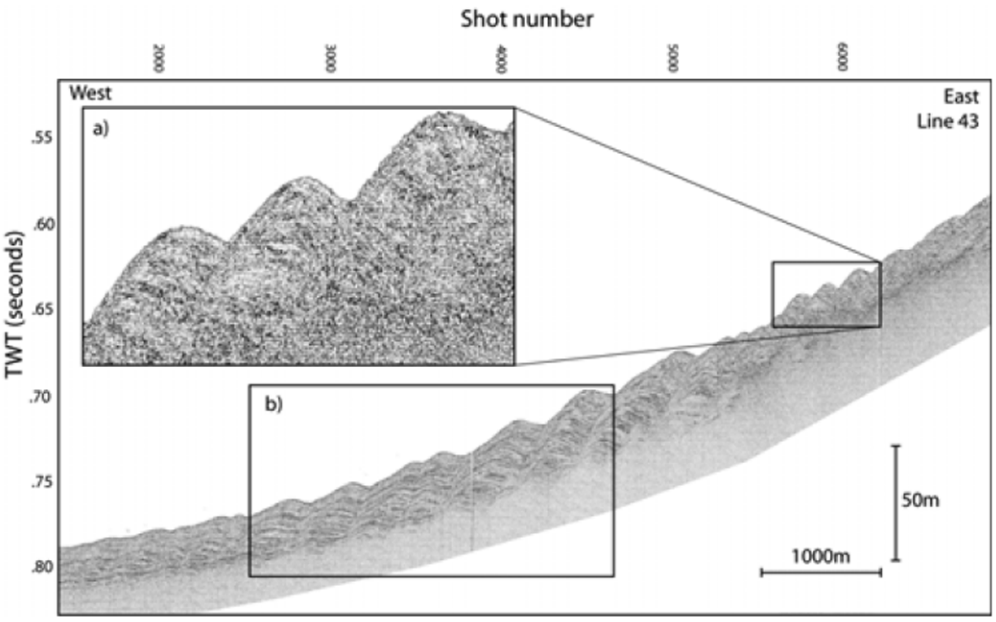

Figure 5. Huntec seismic line collected in August 1995 on cruise W-2-95-NC. The line trends NW-SE across the structure and is from *Gardner et al.* [1999]. Line 43 is 6086 m long, with the inset (region a) covering 910 m. Two way travel time is in seconds. Region (a) images the three structural highs that are shown in Figure 4. Region (b) images a drape that is much thinner upslope in the location of the cores (modified from Figure 4 of *Gardner et al.* [1999]).

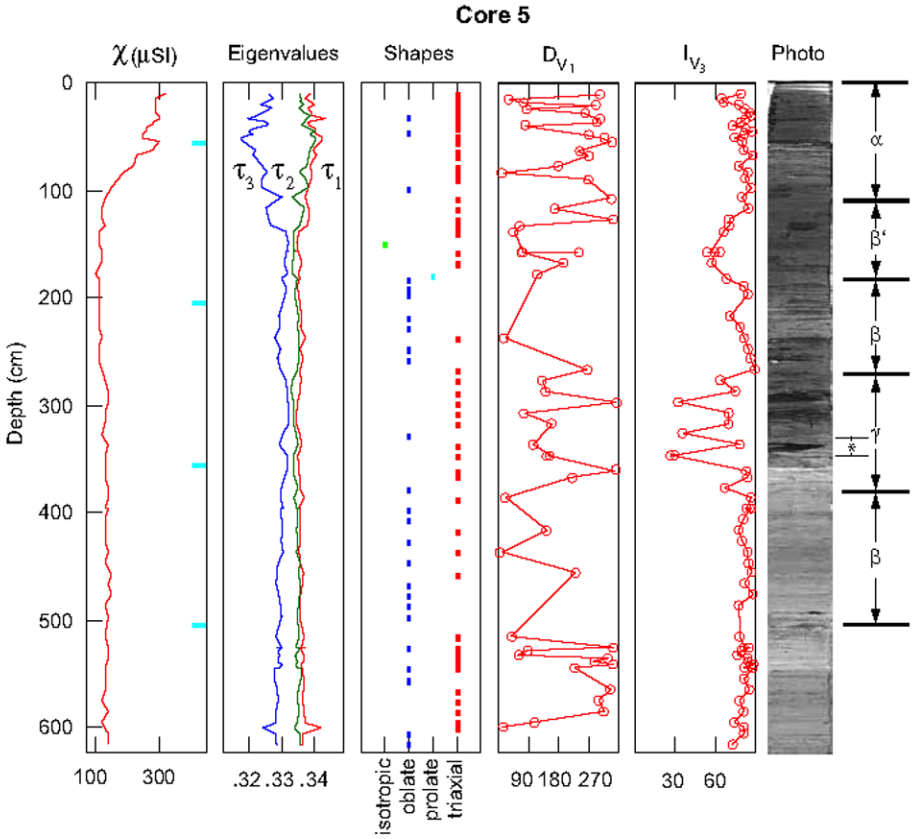

Figure 6. Piston core 5 is located north of the Humboldt Slide as a control core. Down core measurements of bulk susceptibility (χ_{lf}), eigenvalues, fabric type (as illustrated in Figure 3), D_{V_1}, and I_{V_3} are shown. The majority of samples show triaxial fabric suggesting deposition under strong flow conditions. There is no systematic pattern in the D_{V_1}, but there is a zone from 270-380 cm (γ zone) where I_{V_3} differs significantly from vertical, which could possibly be a slump or extreme flow conditions. See Figure 16 for an enlarged view of the region delineated by the (*) to the right of the core photo in the γ region, which appears to be a recumbent fold. The core photo shows that the γ region of shallow I_{V_3} is located just above the transition from overlying darker sediment to the underlying lighter sediments. Vascular plants are concentrated in the upper darker regions.

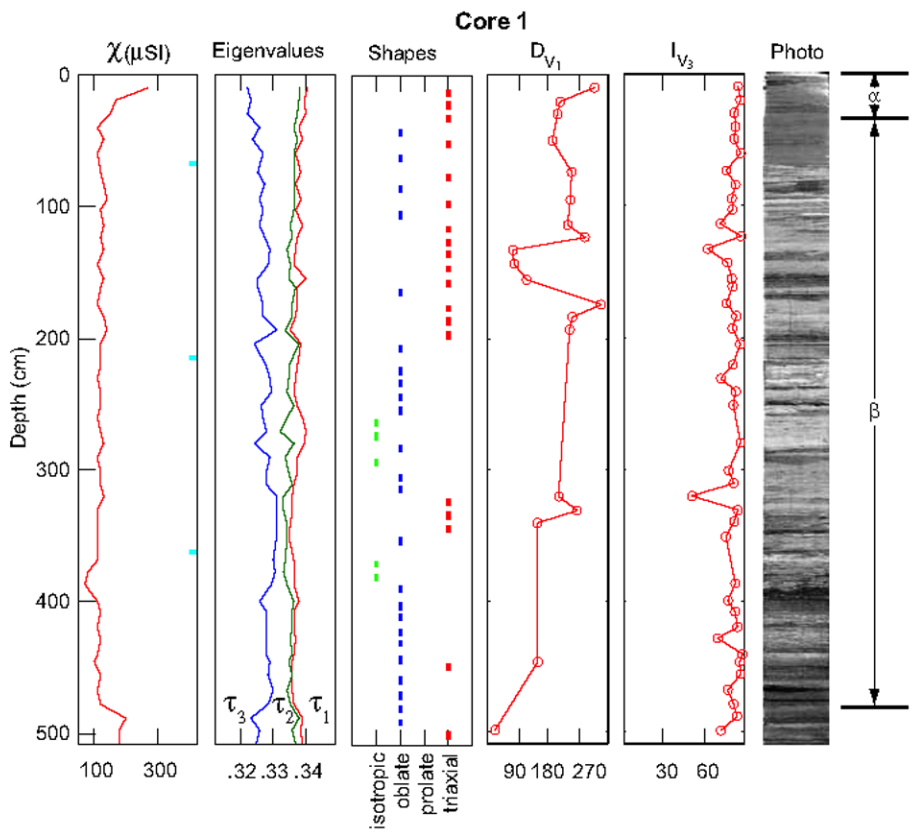

Figure 7. Piston core 1 is located on the downslope limb of the wave structure. Note that the upper 200 cm of the core appears triaxial whereas beneath this, the sample fabrics are predominantly oblate. The eigenvalues suggest a systemic decrease in the overall anisotropy down core. The density of V_1 and V_3 measurements compared to the number of samples in the shapes column appears low because many samples failed to pass the 95% F-tests (*Hext* [1963]). The ticks on the right side of the χ_{lf} graph mark the boundaries where the core was cut into sections.

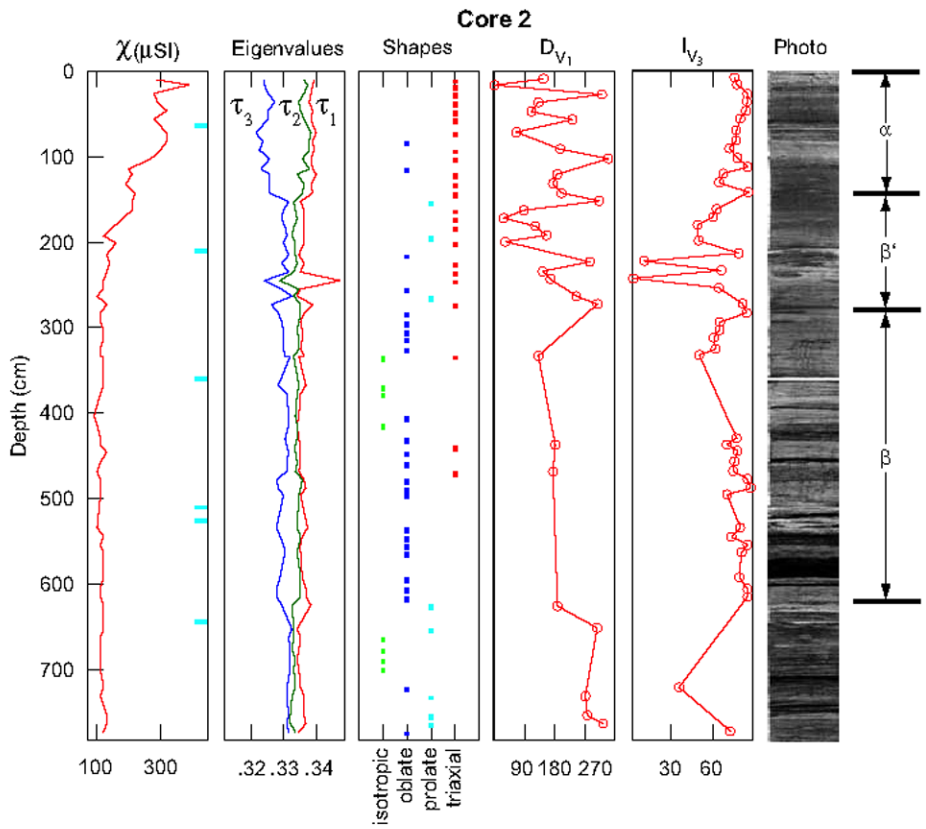

Figure 8. At 100 cm core depth in piston core 2, there is shift in both χ_{lf} and the eigenvalues that culminates at approximately 190 cm. This shift suggests two different sediment sources. Underlying this transition is a region that appears to be deformed (or have been deposited under high flow conditions) from 160 to 280 cm. Pervasive deformation throughout the core is not observed.

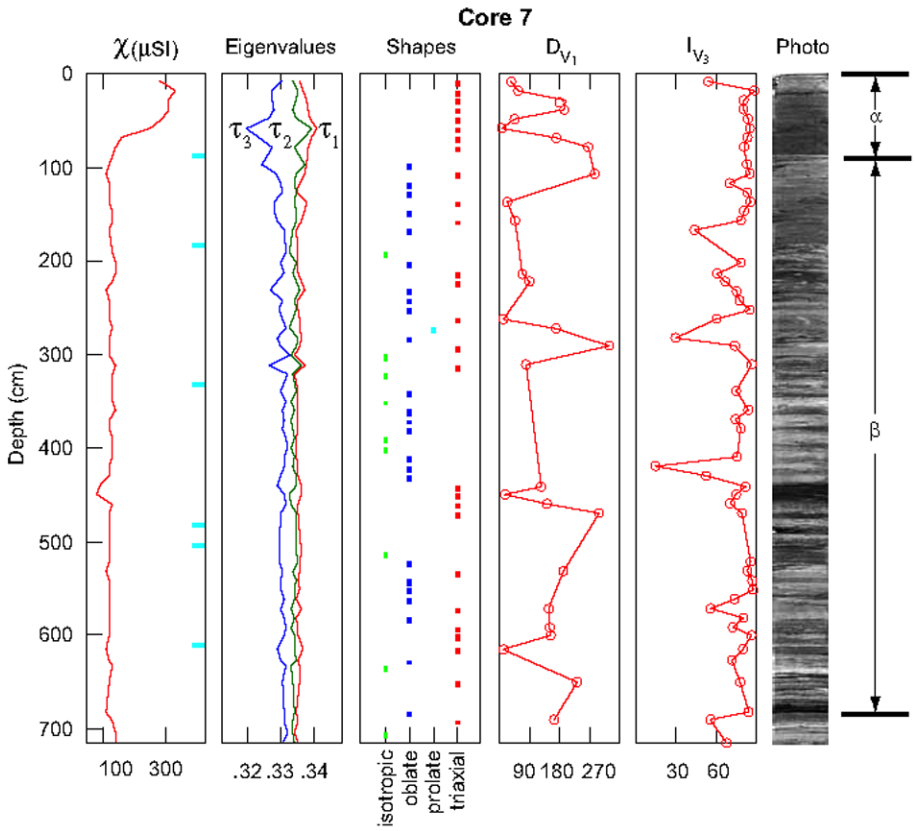

Figure 9. Piston core 7. This core has the same shift in χ_{lf} observed in the other piston cores. There is no discernible trend in the D_{V_1}. The I_{V_3} shows a section with non-vertical vectors, but this is a small region and many of the samples are isotropic.

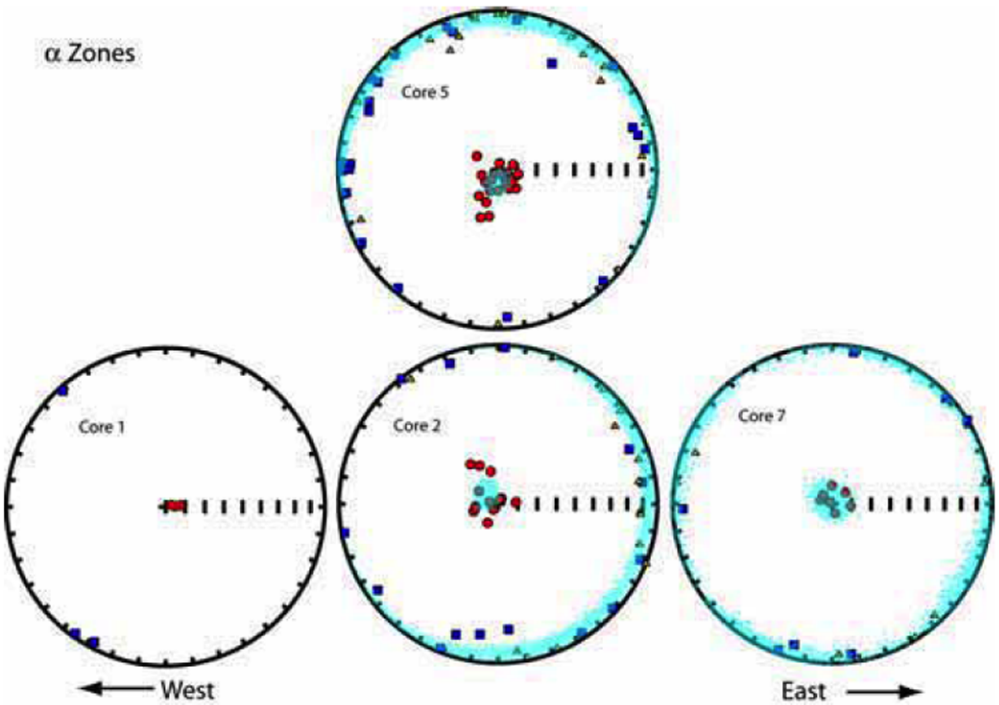

Figure 10. α zones occur at the top of each of the piston cores. This zone is characterized by high χ_{lf}, anisotropy, ARM, and IRM. The individual shape fabrics are predominately triaxial. Bootstrap eigenvectors have a tight cluster near vertical. Blue squares are V_1 ; yellow triangles are V_2; and red circles are V_3. The cyan dots are the bootstrap eigenvectors; eigenvectors are not distinguished.

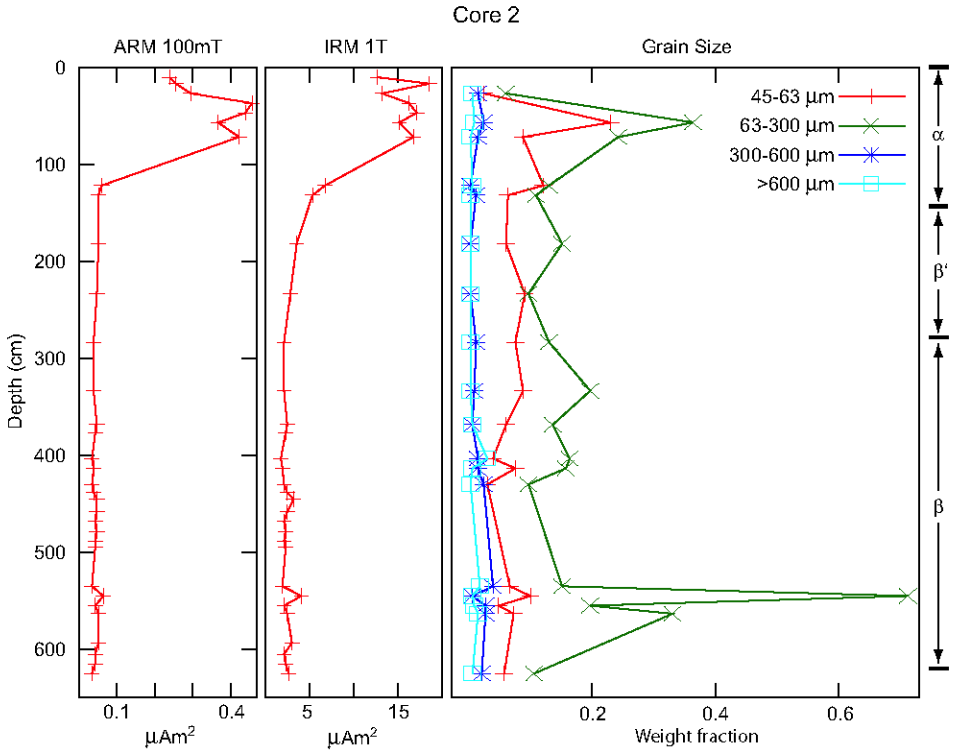

Figure 11. Anhysteretic remanent magnetization (ARM) and isothermal remanent magnetization (IRM) show an abrupt decrease from α to β'. There is a distinct difference in the ARM and IRM in the first meter of the core. There is a much higher concentration of magnetic grains and a different grain population. The 300 and 600 μm sieves were selected to sort out the vascular planet material, where the >600μm material is predominantly twigs and branches. The 63-300μm range captures the sand fraction while the 45-63μm range captures the coarse silt fraction.

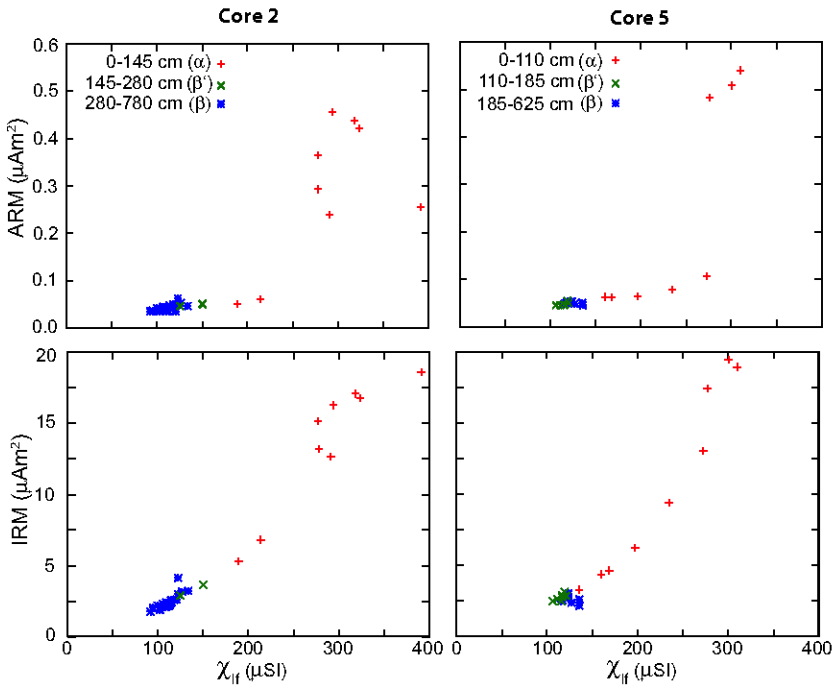

Figure 12. Core 2 and 5 Banerjee plots. *Banerjee et al.* [1981] showed that a χ_{lf} versus ARM plot can show grain size for magnetites based on the slope of a line that passes through the origin. In this figure, cores 2 and 5 show three distinct groups. The top of the core exhibits high χ_{lf}, ARM, and IRM with a transition zone in the middle down to the lower χ_{lf}, ARM, and IRM in the deeper section of the core. Comparing to Figure 11 one can see that shifts in grain size do not necessarily lead to the same change in the magnetic grains.

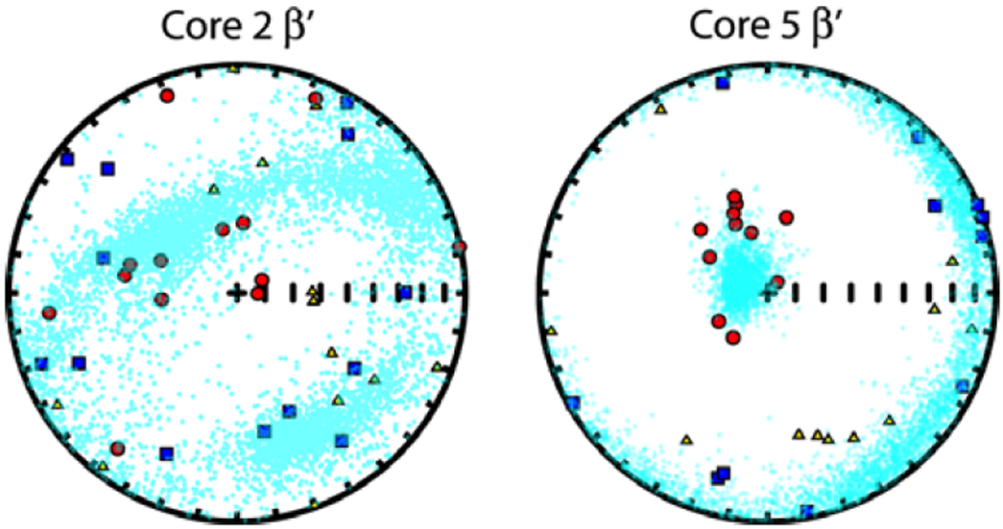

Figure 13. β' zones occur between α and β and has intermediate values of total anisotropy and bulk susceptibility. The individual shape fabrics are predominately triaxial. Note that there are a number of prolate samples in these two β' zones (see Figures 6 and 8). Unlike α and β, β' has V_3 vectors that are deflected from vertical.

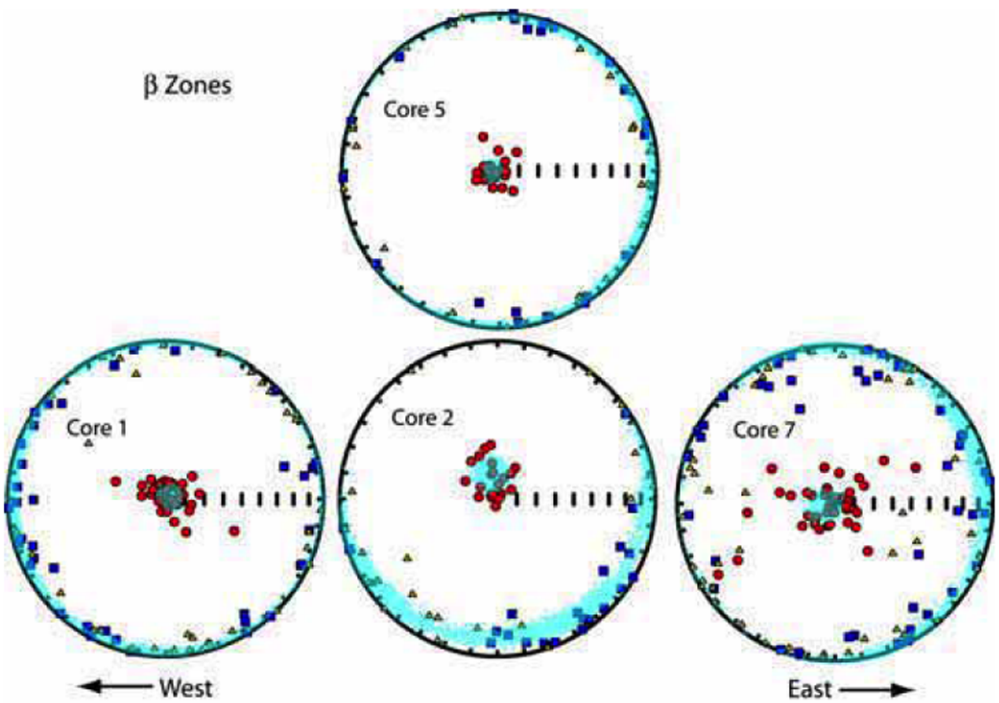

Figure 14. β zones are characterized by lower anisotropy, ARM and IRM compared the α zones. Individual sample shape fabrics are mostly oblate with some isotropic and triaxial samples. Bootstrap eigenvalues have a tight cluster near vertical. For all except core 7, the V_3 are near vertical. Core 7 has a number of small zones with non-vertical V_3 that may record deposition in a moderate current because there is no preferred orientation for V_1.

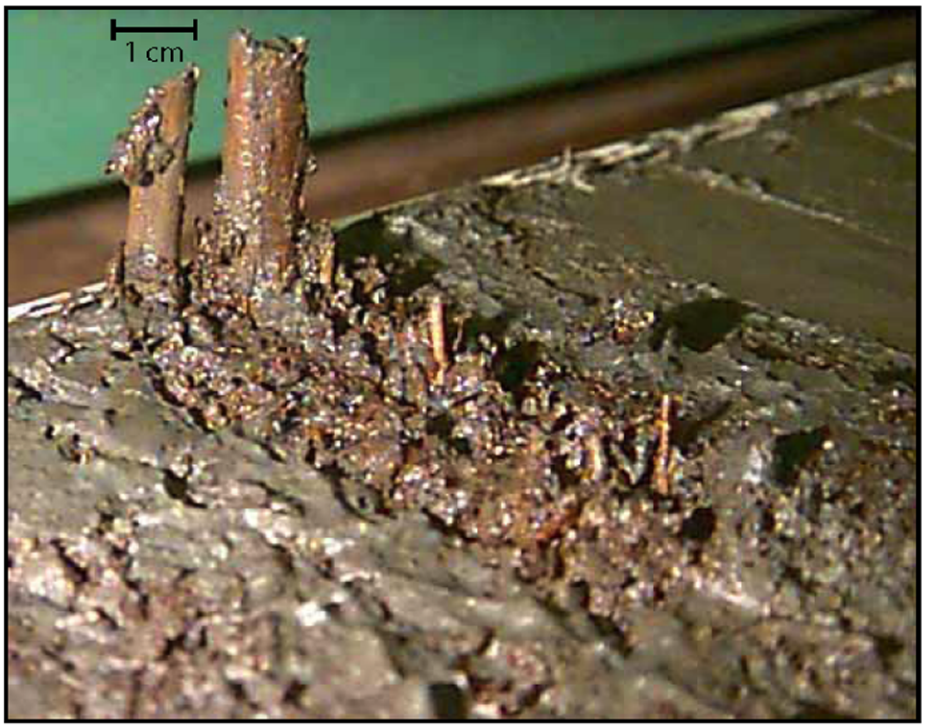

Figure 15. Oblique photograph of core for inside the Humboldt Slide located at 124° 29.055' W, 40° 50.106' N in 419 meters of water. The plant matter shown here (at 130 cm from the core top) illustrates frequent flood layers from the Eel River are deposited in the Humboldt Slide region.

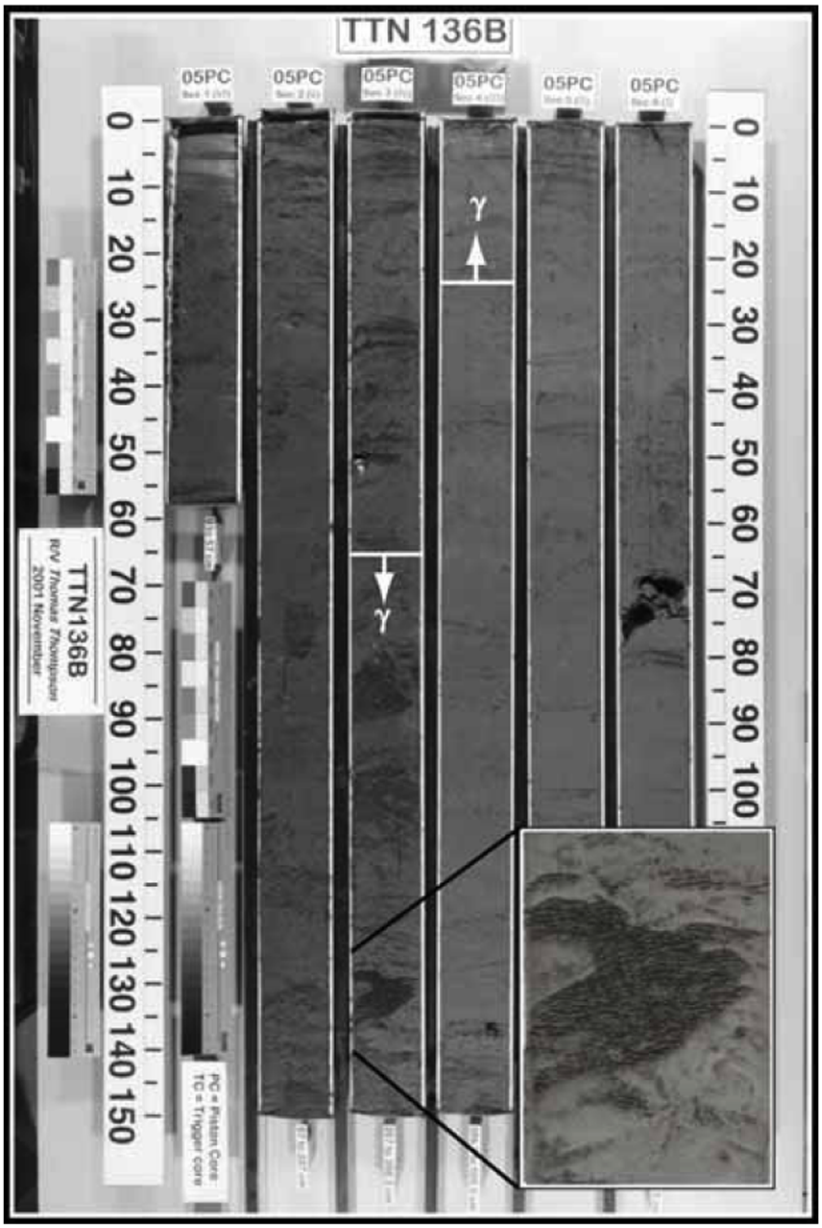

Figure 16. Core 5 photograph. The inset shows an apparent folded layer within the deformed γ zone.

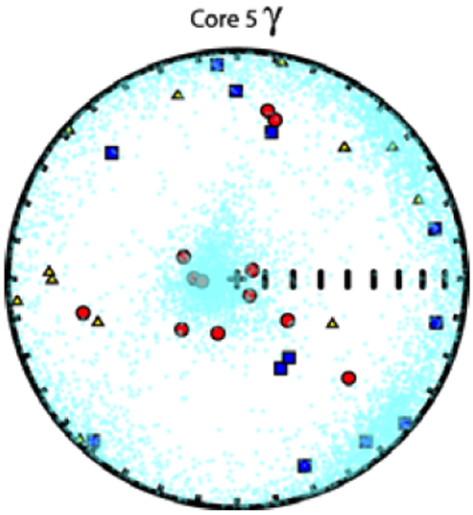

Figure 17. The γ interval is only observed in Core 5. This zone is located between two β zones. γ has triaxial samples, low χ_{lf}, and V_3 vectors that deviate significantly from vertical.

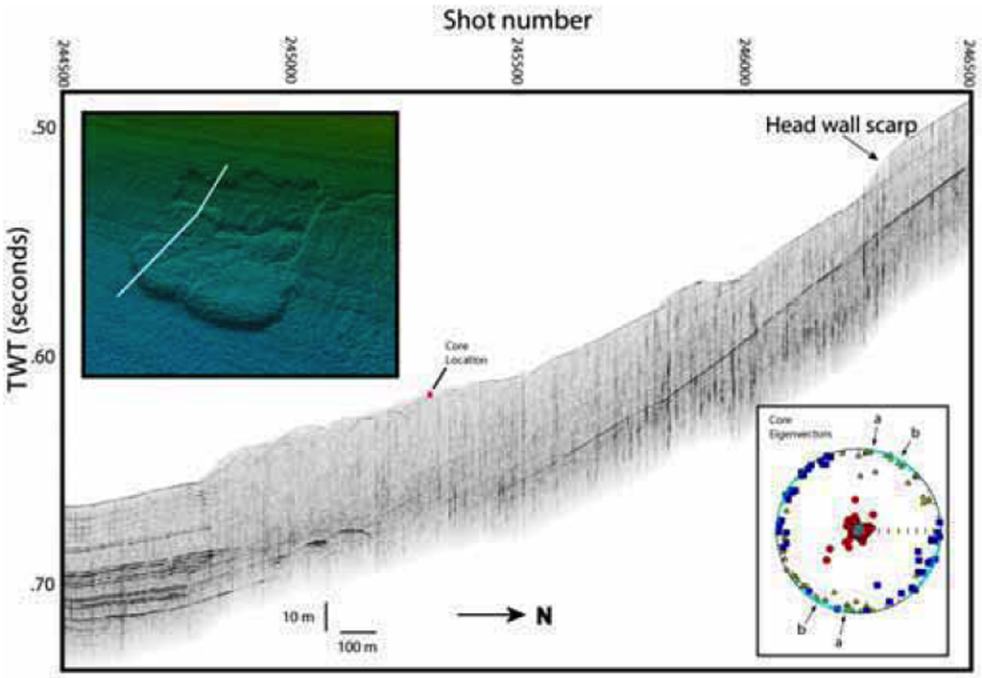

Figure 18. A CHIRP seismic profile images the Gaviota Slide in the Santa Barbara Basin, Southern California. Note the clearly defined head scarp and thickening in the accumulation zone at the base of the slide. The inset shows the slide in EM300 from MBARI (*Eichhubl et al.* [2002]). The expected direction of compression based on morphology is indicated by arrow (a). The direction of compression from the eigenvectors, show by arrow (b), closely matches. This seismic line was collected with a CHIRP seismic system (*Schwehr et al.* [submitted]).

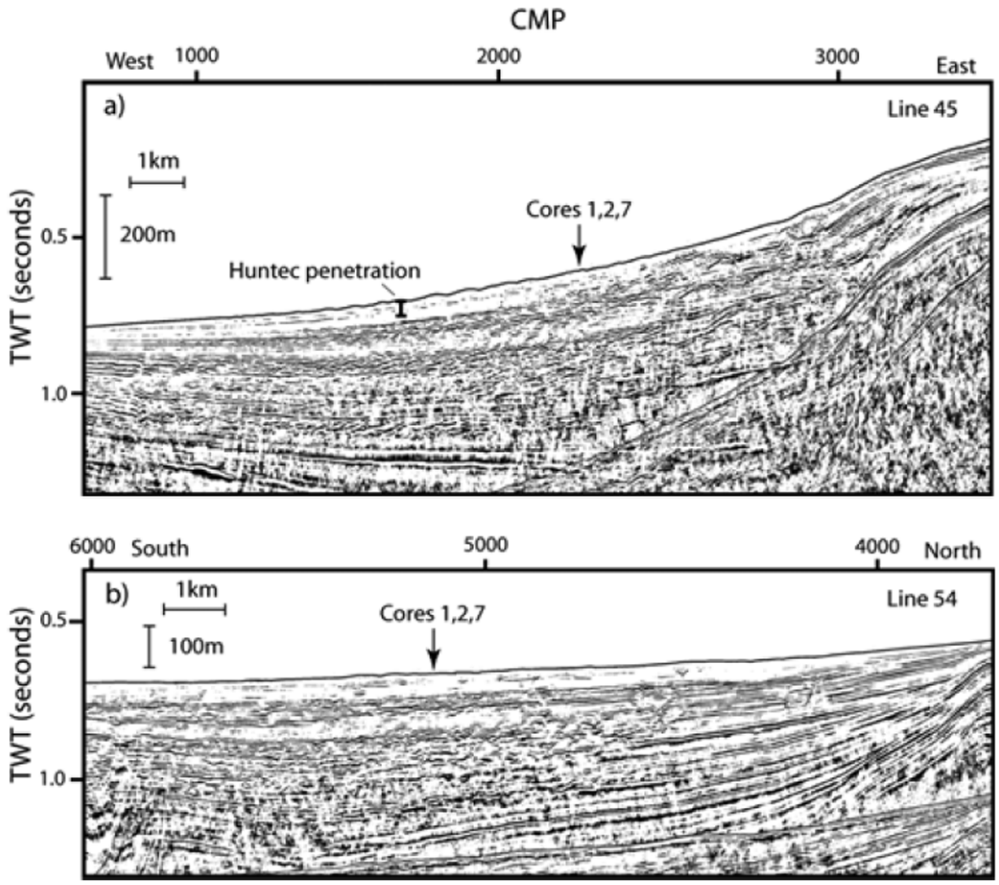

Figure 19. Cruise W9605B multi-channel seismic lines. Line 45 is a dip line imaging the internal structure of the Humboldt Slide. Line 54 is a strike line across the region that includes the Little Salmon Anticline on the northern side. The location of cores 1, 2, and 7 is marked with an arrow. Line 45 runs from CMP 770 to 3323 that spans 16.0 km. Line 54 is 14.6 km long from CMP 3698 to 6017.

IV.L Chapter Acknowledgment

Chapter 4, in full, is the material as submitted to *Marine Geology*, Origin of continental margin morphology: submarine-slide or downslope current-controlled bedforms, a rock magnetic approach, Schwehr, Kurt; Driscoll, Neal; Tauxe, Lisa; 2006.

The CHIRP seismic data was collected by Neal Driscoll on cruise TTN-096. The cores were acquired on cruise TTN-136B with Kurt Schwehr as Chief Scientist using the OSU Coring Group. I was responsible for all of the core processing, CHIRP processing, analytical work, and data analysis. A portion of the magnetic measurements were performed by Andrew Harris and Jason Steindorf. Jim Gardner assisted with the processing of the Huntec seismic data. The data interpretation was done in conjunction with Neal Driscoll and Lisa Tauxe. Lisa Tauxe and Neal Driscoll edited the text.

Chapter V

Conclusion

This thesis has presented a new method for applying anisotropy of magnetic susceptibility (AMS) to complement outcrop and seismic data to understand the processes responsible for strata formation. AMS fabric is sensitive to small amounts of strain on both regional and local scales. This thesis extended the existing techniques with detailed analysis of the bootstrap eigenvectors and where possible the overall anisotropy. The Ardath Shale study demonstrated that the AMS bootstrap technique can detect deformation that is not apparent by visual inspection of the local outcrop (termed crypto-slumps). In the study of the Santa Barbara Basin, the AMS technique was applied to unlithified shallow marine cores. In the accumulation zone of the Gaviota Slide, the AMS bootstrap mean eigenvector matched the direction of compaction predicted from morphology observed in multibeam data to within 20°. Given that the Santa Barbara Basin sediments are very homogenous, it was possible to use the AMS eigenvalues to detect compaction disequilibria. Zones of high water content were inferred from regions of decreased total anisotropy. An unconformity observed with visual inspection and xray images exhibited a marked increase in anisotropy at the interface. The last study applied the AMS to the controversy surrounding the Humboldt Slide. Analysis of the AMS data showed no evidence for post-depositional deformation predicted by the thin skinned slide model. Additionally, the AMS signature was found to be consistent with expected flow directions in the region.

The ability to detect the two types of compaction disequilibria (underconsolidation and apparent overconsolidation) is another step in predicting the recurrence interval and size of submarine landslides that helps assess the tsunamigenic potential of an area (Driscoll et al., 2000; Ward, 2001). Continental shelf and slope areas are becoming increasingly important for economic development of hydrocarbons, wave energy, and other resources. Slope stability is a critical component to understand for engineering and managing safe development.

V.A Ardath Shale

AMS fabric is sensitive to strain even in small amounts on both regional and local scales. Such strain does not have to be visible for effects to be detectable in the AMS and NRM measurements. Several authors have devised tests for sediment deformation based on AMS fabric. Shor et al. (1984) used a strict test that discards all samples with f $> 15^o$, where f is the angular deviation of V_3 from the pole to bedding. Rosenbaum et al. (2000) developed a similar test that also relies on the V_3 vector. They expect "good" samples to have a standard deviation of V_3 inclination (σ_{V_3}) of $< 6.5^o$ and an inclination average of V_3 (I_{V_3}) of $<6^o$ from the vertical. In short, we see a relationship that is opposite to that seen by Rosenbaum et al. (2000), whereby the disturbed intervals are actually more tightly grouped and more vertical than the undisturbed interval.

The principle results of this paleomagnetic study are summarized as follows:

1. The I_{V_3} method (Rosenbaum et al., 2000) may be able to distinguish fluidized zones, but needs to use Hext (1963) statistics.

2. There are many reasons why V_3 could be deflected from the vertical other than post-depositional deformation.

3. Sediments can be severely deformed without deflecting V_3. We propose that adding the eigenvalue test is much more sensitive to deformation than just V_3 deflection.

V.B Santa Barbara

The principle results of our rock magnetic and seismic study may be summarized as follows:

1. AMS, when combined with water content, χ_{lf}, ARM and IRM may add additional information about the compaction history of the sedimentary sequence

revealing subtle compaction disequilibria in sediments of relative uniform composition.

2. Zones with excess water are associated with less compacted AMS signals (relatively lower anisotropy).

3. Abrupt change in the degree of anisotropy can reveal unconformities caused by evacuation of slumped material, and exhumation of underlying sediment. These sediments had generally higher anisotropies than equivalent levels in other cores (apparent overconsolidation).

4. AMS eigenvectors detected the slump with principle strain axis consistent with that expected from the slide morphology.

In summary, anisotropy of magnetic susceptibility is shown to be an effective tool for exploration of sediment consolidation state. The approach is able to identify the location of unconformities that have apparent overconsolidation, and can point to horizons that might become regions of overpressure. None of the methods for detecting compaction disequilibrium works for every possible situation, but AMS complements the arsenal of techniques used for detecting compaction disequilibria. When looking at AMS signatures, it is important to recognize major lithological changes because a change from clay-rich to sand-rich sediment could be misinterpreted as a major change in sediment compaction, or pore pressure. AMS cannot be used in zones where rapid diagenesis of the magnetic fraction is occurring. Caution should be used when fitting exponentials to the sediment water content as only small excursions in water content will be detected.

In addition to overpressure, there are other mechanisms for destabilizing sediments on a slope such as zones of weakness associated with certain lithologies or bioturbation, storm wave loading, bubble-phase gas, and oversteepening. Enhancing our understanding of where and how overpressure zones are likely to form in near surface sediments is helpful for evaluating the risk factors associated with slope failure. Overpressure does not necessarily result in slope failure, but it does

reduce the effective normal force of the overlying sediment thus allowing the ratio of shear stress to effective normal stress to increase. These zones of weakness may be nucleation sites for failures.

V.C Eel

The main results of our rock magnetic and seismic reflection study are summarized as follows:

1. The Humboldt Slide sediments in the upper ~8 m are not undergoing pervasive deformation and folding.

2. The upper section sampled in this study is composed of downslope current-controlled bedforms.

3. Based on MCS data, the majority of the sediment structures with the Humboldt Slide are sediment waves that may mantle a deeply buried older slide.

4. We identified a ~1 m thick slump located to the north of the Little Salmon Anticline in the region with extensive rills.

5. The change in how much and what fraction of material is delivered to the Humboldt Slide area (versus that north of the Little Salmon Anticline and down the Eel Canyon to the south) may have undergone a recent shift caused by the increasing frequency of combined large storm and flood events from 1955 to the present. This possibility requires further research.

Magnetic measurements allow us to test between the alternative hypotheses of slope failure, and sediment waves for the origin of the Humboldt Slide. Specifically, we are able to discern whether the distinctive morphology associated with the feature results from soft-sediment deformation and retrogressive slumping, or downslope current-controlled deposition. The former predicts a triaxial AMS

fabric with essentially north-south oriented maximum axes; the latter predicts an oblate fabric with a possible westward deflection of the minimum axes.

The morphology and internal architecture of the Humboldt Slide are not unique; there are numerous examples along other continental margins with similar morphology and with similar debates regarding their origin (see examples in Lee et al., 2002). Our study of the Eel River margin is applicable to the construction and evolution of other continental margins. Magnetic methods for the detection of deformation should work in many marine sediments assuming that care is taken to avoid interpreting the AMS signatures in regions of rapid diagenetic changes.

Appendix

Table A.1: XStar CHIRP pulse names.

Name	Length (ms)	Start (kHz)	End (kHz)
L	50	1.0	6.0
M	35	1.0	6.0
N	20	3.0	15.0
O	20	2.5	12.5
P	10	1.0	5.5
Q	10	3.5	15.5
R	10	1.0	15.0
S	3	1.0	15.0
T	30	1.0	15.0

A CHIRP seismic reflection

A modified EdgeTech XStar CHIRP subbottom profiler was used to acquire seismic reflection data (Figure A.1). The fish is equipped with two transducers optimized for 0.5-6 kHz and 2-16 kHz. These transducers are combined to produce a linear swept frequency pulse with a Tukey-Hanning taper. The topside is connected to the computer in the fish via an asymmetric digital subscriber line (ADSL) with the pulses being generated locally on the fish. This removes the distortions that occur because of impedance mismatch and noise when the pulse is transmitted down the tether. The XStar system waits a specified delay and then begins recording. The system convolves the returned signal with the sent pulse (termed "match filtering") and then records 3976 samples of 2-byte signed integers (Figure A.2). An example of data recorded for both channels after match filtering is shown in Figure A.3. The XStar system is programmed with 9 chirp modes. In this thesis, only the 'L' pulse was used (Table A.1).

Seismic processing was done with SIOSEIS, pltsegy, and segy-py. Segy-py was used to slice the seismic lines, find and export water bottom picks, and generate base maps. SIOSEIS converted the XStar version of SEG-Y to a more standard SEG-Y form and then for filtering. Pltsegy was used to generate the final figures.

The use of a cable to tow the fish presents an extra challenge. There is a

variable offset between the GPS receiver on the ship and the position of the fish in the water column. To approximate the position of the fish, a "layback" correction must be applied (Figure A.4). During the acquisition of the data for this thesis, the fish was not equipped with a pressure transducer. Therefore multiples from within the dataset were used to calculate a fish depth. Additionally, for the Humboldt Slide chapter, the wire-out was not known. Therefore, a wire angle was estimated based on that found from other cruises. Figure A.5 shows an example processed line with layback calculated with a best estimate of layback and the error bar for the likely range of wire angles. Layback is calculated based on Equation A.1.

$$layback = g + w_d + \sqrt{w_o^2 + (h + f_d)^2} \tag{A.1}$$

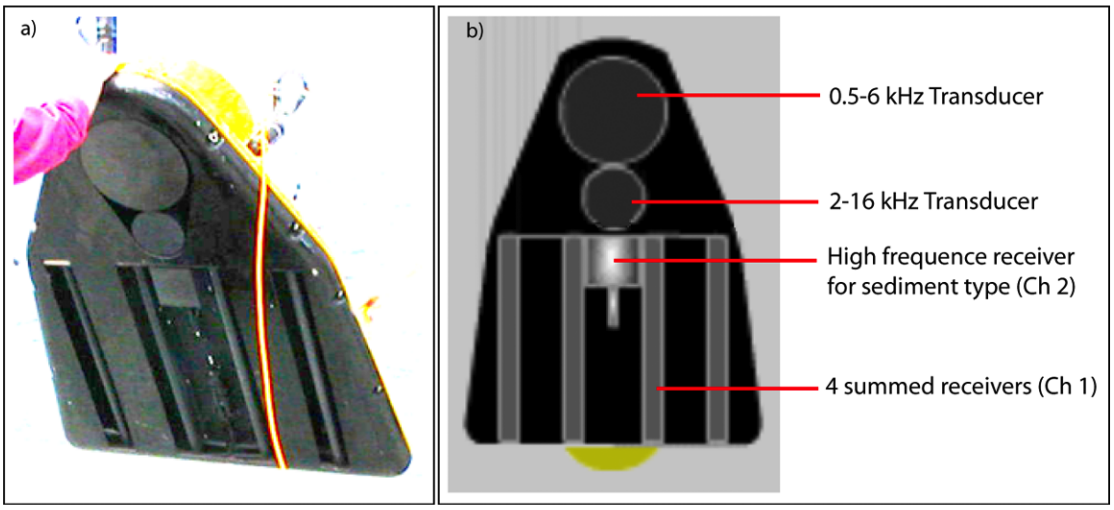

Figure A.1: a) Photograph of the underside of the XStar CHIRP seismic reflection fish. b) Schematic showing the location of the transducers and receivers.

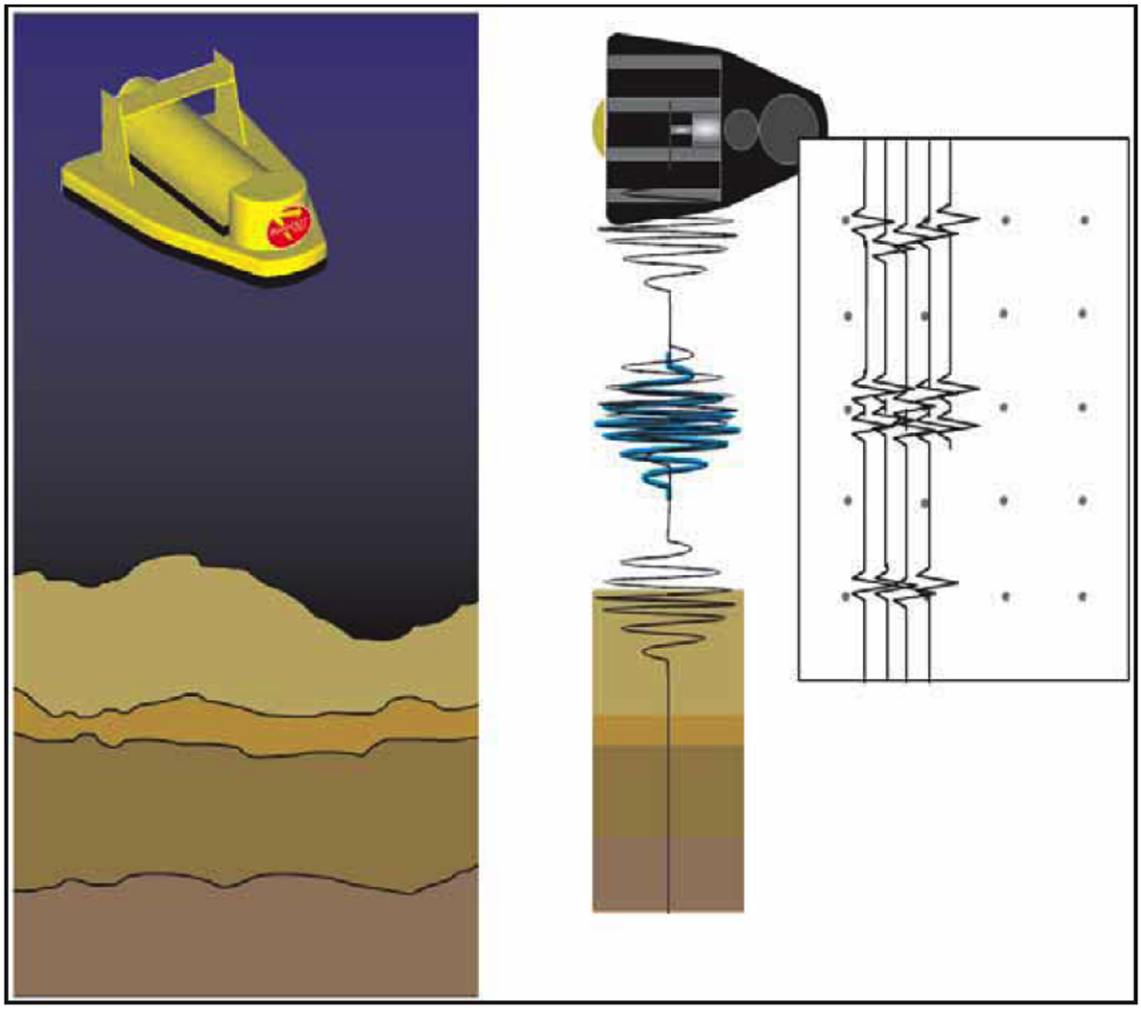

Figure A.2: Match filtering the received waveform with the outgoing pulse. Base image courtesy Genevieve Tauxe.

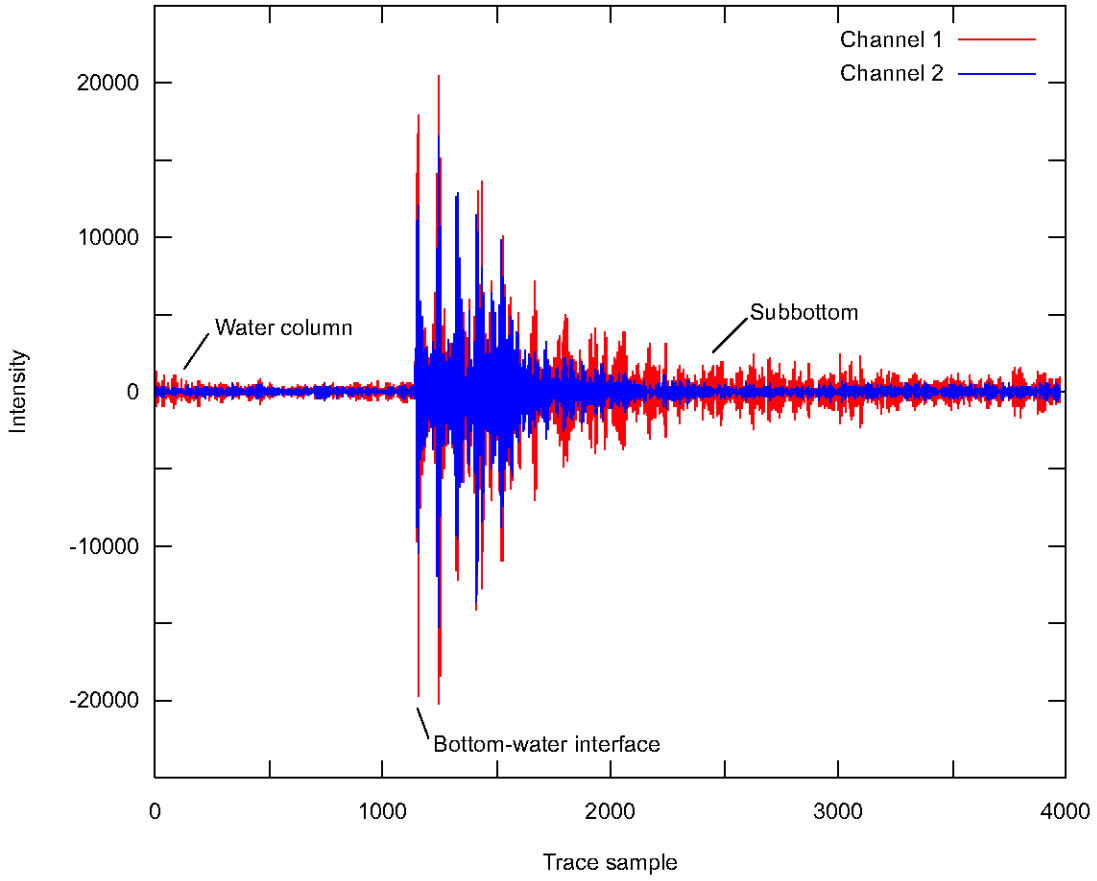

Figure A.3: Example match filtered returns.

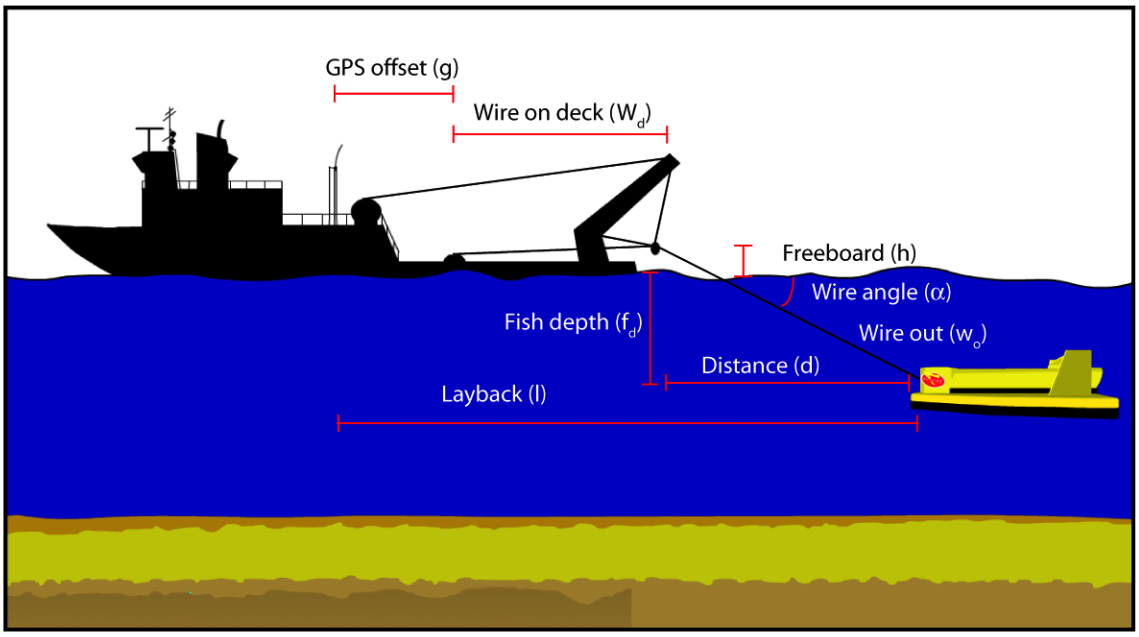

Figure A.4: Fish layback geometry. Base image courtesy Genevieve Tauxe.

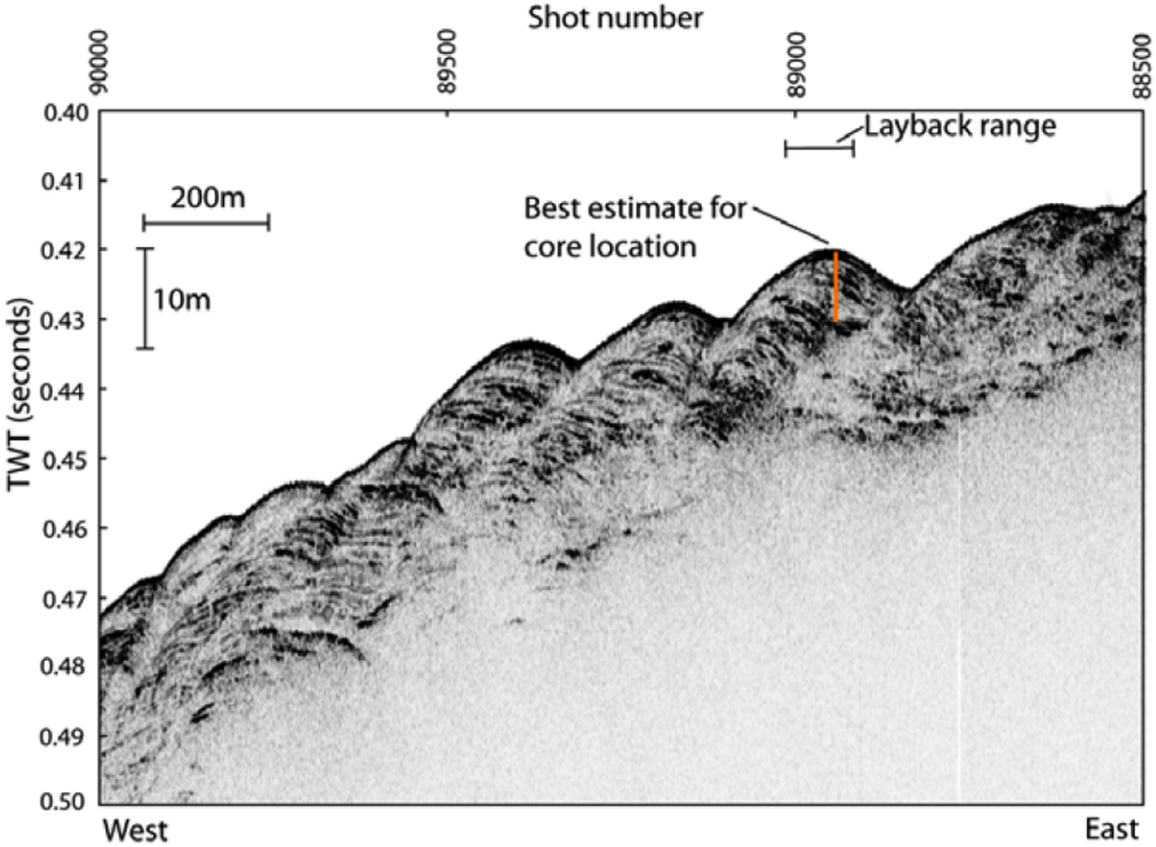

Figure A.5: Example processed seismic line.

B Coring

In these three studies, a different type of coring technique was used for each depending on the material to be sampled and the depth of penetration required. For lithified sediments exposed in outcrop, a water-cooled rock drill is required (Figure A.6). For the Ardath Shale, such a drill was used to acquire short cores. Once the drill has created a cylindrical cut in the rock, a non-magnetic slotted tube is inserted with a gnomon and inclinometer attached at the end. This device is used to get the orientation of the core and scratch a reference line. These cylindrical cores are then cut into standard sized paleomagnetic cylindrical specimens. This coring style allows many specimens to be collected from a particular horizon.

To acquire sediments from near surface marine environments, ship-based coring techniques must be used. For the Santa Barbara Basin, the project required only 1-2 m cores. A simple gravity coring device was used for this project (Figure A.7). The device consists of a metal barrel lined with a plastic tube. A cutting bit with a core catcher is screwed onto the bottom. One to two hundred kilograms are loaded onto the top to help drive the barrel into the sediment column. The system is run into the bottom at the maximum safe speed allowed by the winch (e.g. 30 m/min). The sediment and core liner are extracted by removing the cutter and core catcher and then a crane is used to vertically lift off the core barrel.

The Humboldt Slide study required as much penetration as possible. Therefore a more complicated piston coring system was used (Figure A.8). The system consists of a much longer core barrel (multiple sections connected together) with one to two thousand kilograms of weights. These are hung from a release hook along with a spool of wire to allow the core to free fall to the sea floor. A trigger arm holds a trigger core below the bottom level of the piston core. When the trigger core hits the sea floor, the trigger arm raises and releases the piston core, which free falls. The spool of wire is attached to a piston within the core barrel

with such length that it stops close to the sea floor. The core barrel drops around the piston thereby creating suction that helps bring the sediment into the core liner. On deck, the piston core is laid horizontally and the liner is pushed out of the barrel by hand with a ram.

For the gravity and piston coring systems, the liner is cut into 150 cm or shorter sections for processing. The sections are first numbered with Roman numerals on the ship starting from the deepest section. Once back in the Scripps Institution of Oceanography Core Repository, the core sections are numbered in Arabic starting from the top section of core as section "1." These sections are cut into halves which are designated the "working" and "archive" halves. The two faces are then sampled using standard 8 cm^3 paleomagnetic cubes.

Unlike the rock-drill, the gravity and piston coring systems are lowered on a wire such that there is no easy way to control or record the orientation of the acquired core. As a result, the cores must be oriented based on the natural remanent magnetization (NRM) record in the collected sediment cores. Additionally, the piston core liner was sectioned immediately after being brought on deck without marking the relationship between sections, therefore separate rotations had to be calculated for each core section.

Figure A.6: Rock drill with water cooling.

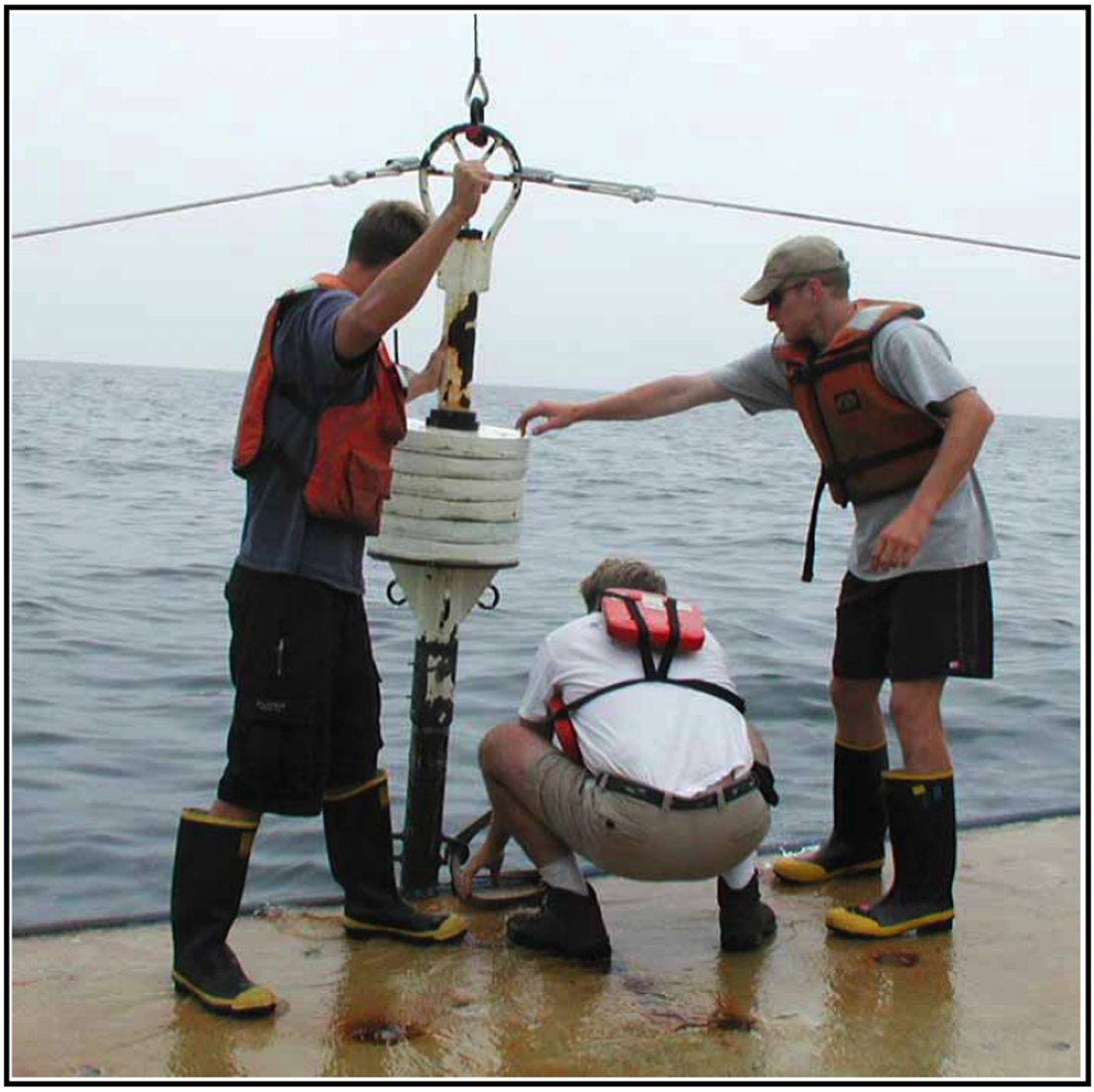

Figure A.7: Photo of the SIO "King Kong" gravity coring system.

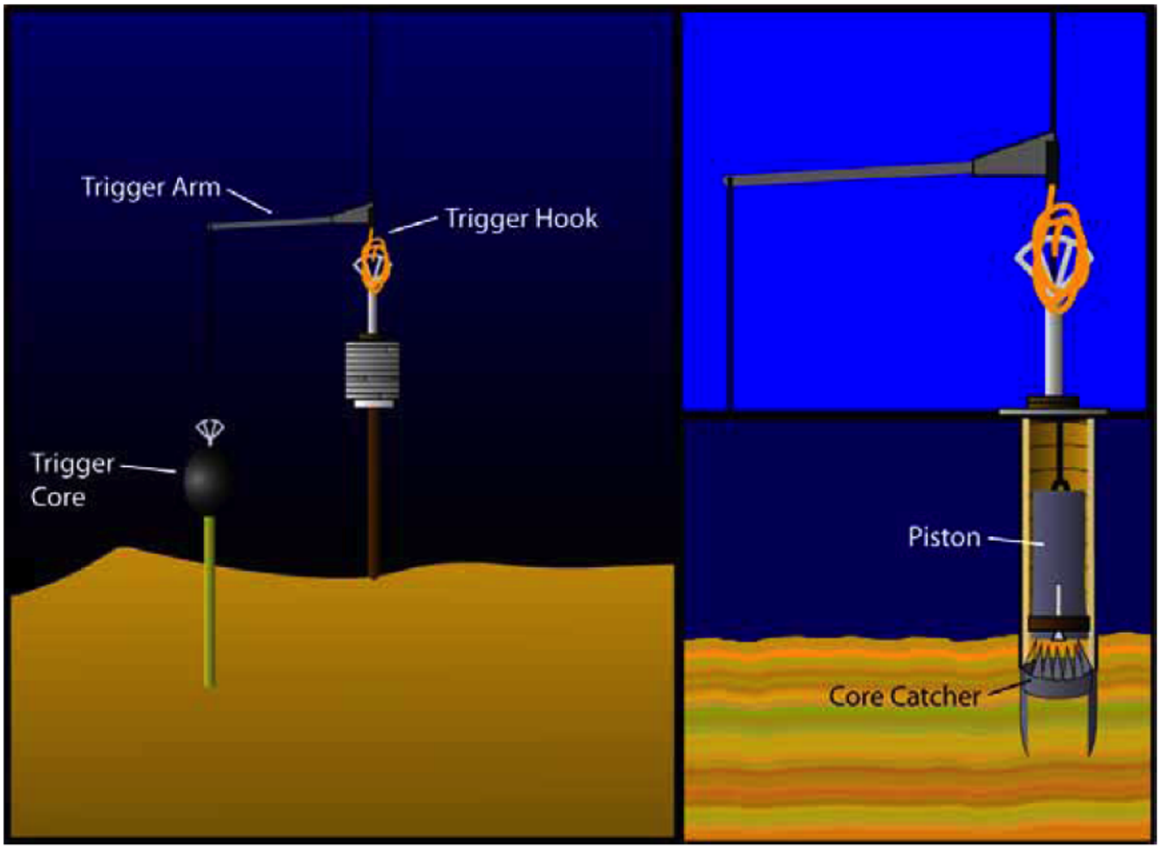

Figure A.8: Schematic of piston coring. Courtesy Genevieve Tauxe.

C Magnetic Properties

The focus of this thesis is the use of magnetic susceptibility as a measure of the sediment fabric. Magnetic susceptibility (χ) is the degree of magnetization of a material (M) in response to an applied alternating magnetic field (H), where

$$M = \chi H \tag{A.2}$$

A hysteresis loop generated from an Alternating Gradient Force Magnetometer (AGFM; Figure A.9) illustrated many of the important magnetic parameters. In Figure A.10, the blue loop is the observed M over a range of applied fields for a small sample (e.g. 4 mg). The measurements start at the top right with an applied positive field and run in a loop, returning to the initial field. The slope on the tails of the graph are the contribution of paramagnetic grains and is known as the high field susceptibility (χ_{lf}). The red curve is the observations after removal of the high field slope. The top of the red curve is the saturation magnetization (M_s). M_r is the saturation remanence where the red loop intersects the y-axis as the applied field is lowered from M_s. The bulk coercivity (B_c) is a measure of how stable the magnetic grains are and is the point where the red curve crosses the x-axis.

Within the inset, the cyan line shows the curve for the an applied field starting with a no remanent magnetization. The slope of this curve is the low field bulk susceptibility (χ_{lf}), which is a composite of the susceptibilities of both the paramagnetic and ferromagnetic grains within a sample. The ratio of χ_{hf}/χ_{lf} gives an estimation of the relative fraction paramagnetic grains in the AMS signature. The AGFM is unable to measure larger paleomagnetic samples, therefore χ_{lf} is measured on a KLY-2 Kappabridge (Figure A.11). To measure AMS, I used the 15 position measurement scheme of Jelinek (1978), eigenparameters and confidences were calculated using Hext statistics (Hext, 1963) with the PMAG software package (Tauxe, 1998).

After the AMS measurements were acquired, the two cryogenic magne-

tometers were used to provide supporting datasets (Figure A.12). First alternating frequency (AF) demagnetization was done using a SI-4. Principle component analysis (PCA) was applied to each specimen to generate best fit directions (Kirschvink, 1980). Then Fisher statistics (Fisher, 1953) were used to calculate an overall best fit declination for each core section. After AF demagnetization, a SI-4 was used with a 100 mT alternating field and a 40μT bias field to measure anhysteretic remanent magnetization (ARM). Isothermal remanent magnetizations (IRM) were imparted with an ASC impulse magnetizer using a 1 tesla field.

Once all of the magnetic measurements were completed, I imported all of the data into a SQL database for analysis.

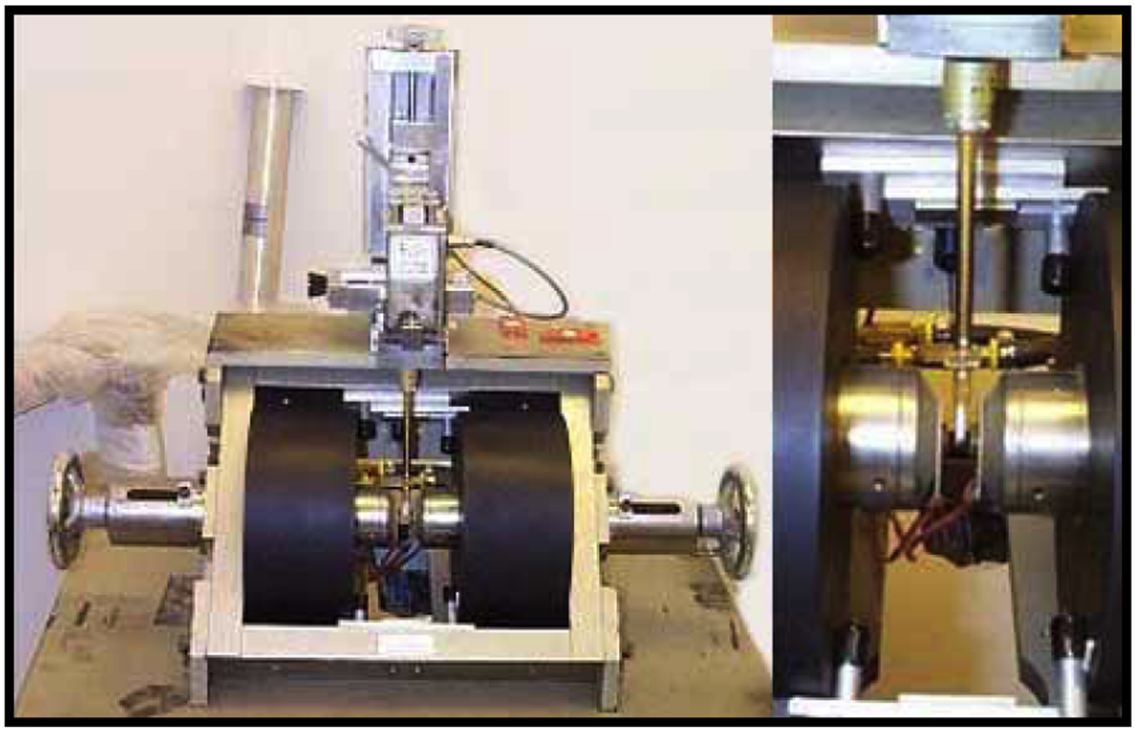

Figure A.9: MicroMag 2900 Alternative Gradient Force Magnetometer (AGFM). Image courtesy SIO Paleomagnetics Laboratory.

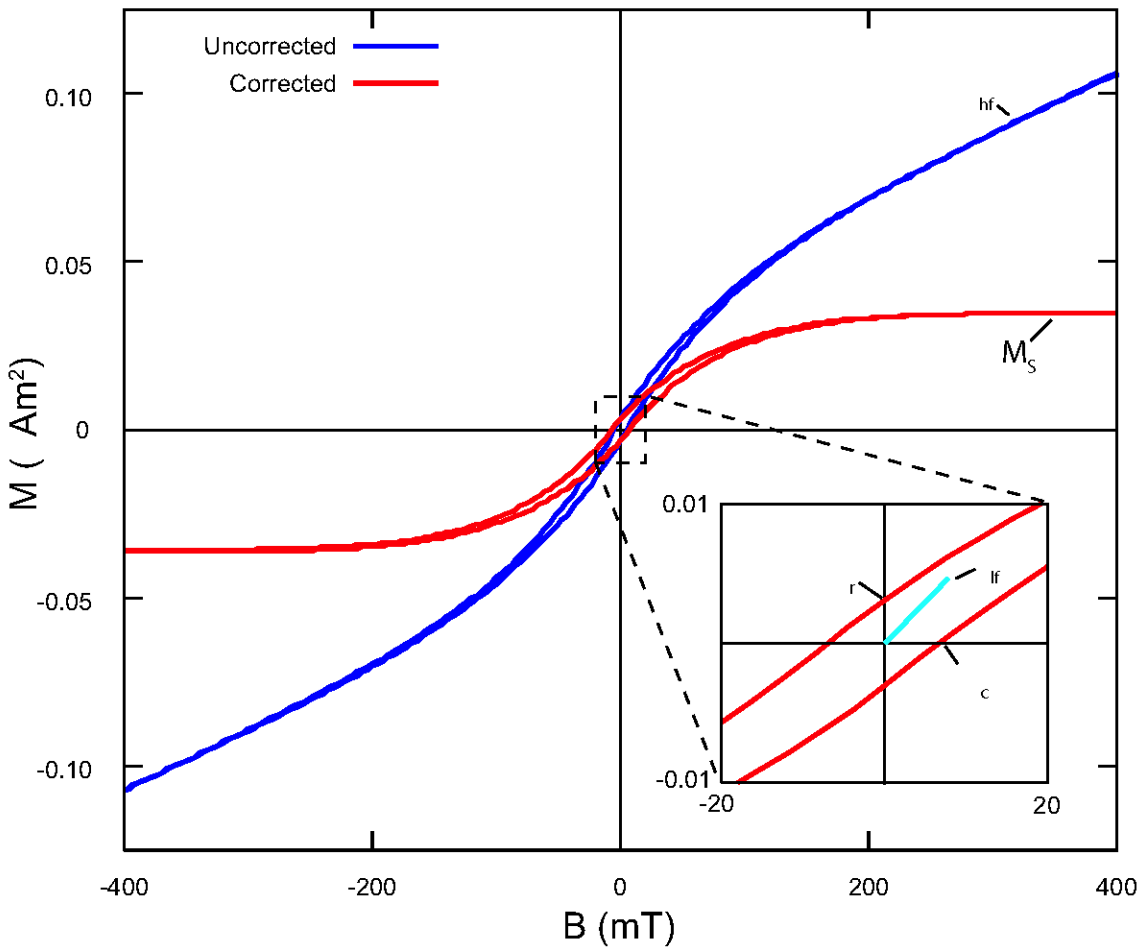

Figure A.10: Example hysteresis loop with magnetic parameters.

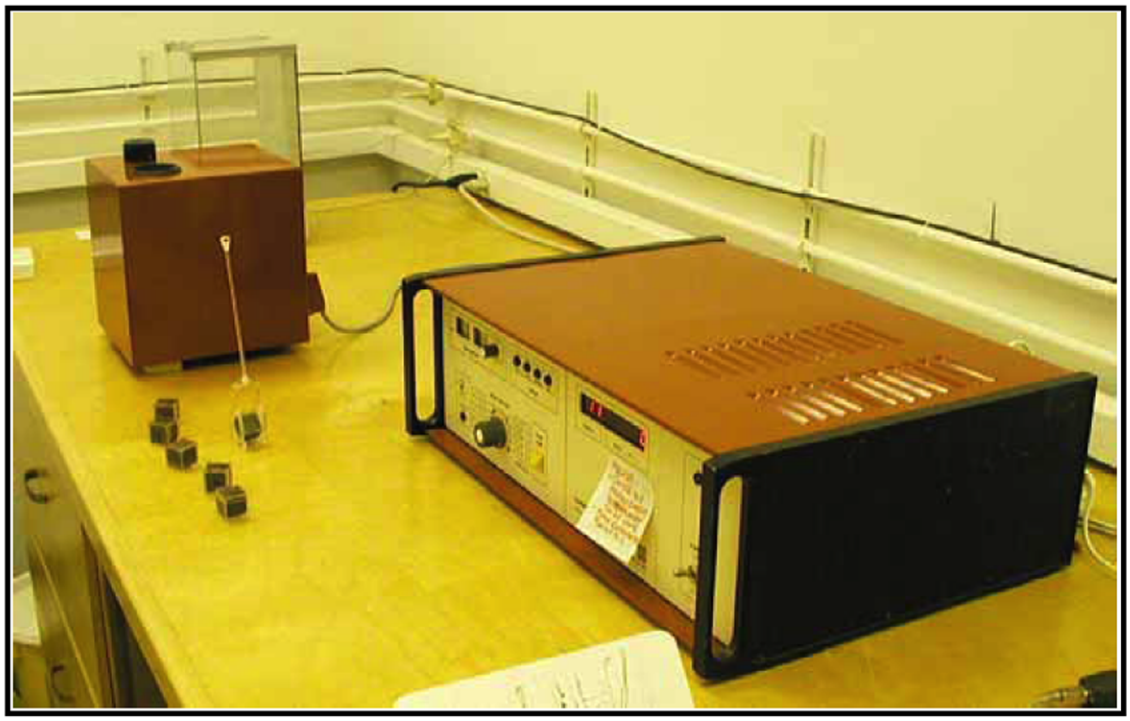

Figure A.11: The KLY-2 Kappabridge measures χ_{lf}.

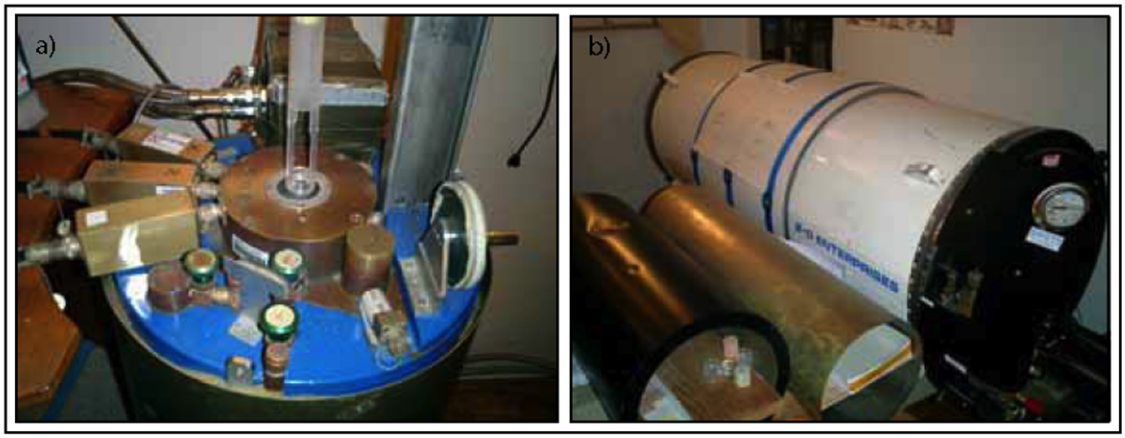

Figure A.12: Cryogenic magnetometers in the SIO Paleomagnetics Laboratory.

D Software development

In the process of completing this thesis, I have produced several software packages to assist in data processing: X-Core, density, pmag-kds-py, and segy-py. X-Core supports the study and integration of datasets for combined magnetic and seismic stratigraphic study by providing a unified OpenInventor based visualization. The X-Core software package is a 3D data base access and integration system that combines sedimentalogical, paleomagnetic, and seismic data into a visually clean display of relevant parameters. The density software package processes volumetric data and displays 3D probability distribution functions such as those produced by bootstrapping of AMS data sets. Pmag-kds-py complements pmag and pmag-py by L. Tauxe (Tauxe, 1998) by adding processing for alternating gradient force magnetometers (AGFM), magnetic unit conversions, simple fabric simulation, and AMS processing. Finally, segy-py introduces low level support for parsing and managing SEG-Y formatted seismic data. Segy-py complements the processing and display functionality of CWP/SU: Seismic-Un*x (Stockwell, 1999), SIOSEIS (Henkart, 2005), and pltsegy (Harding, 2005). Both pmag-kds-py and segy-py have interfaces to SQL databases to ease the management of large datasets.

References

J.S. Booth, D.W. O'leary, P. Popenoe, and W.W. Danforth. U.S. Atlantic continental slope landslides: Their distribution, general attributes, and implications. *US Geological Survey Bulletin*, 2002:14–22, 1993.

N. Christie-Blick and N.W. Driscoll. Sequence stratigraphy. *Annual Review of Earth and Planetary Sciences*, 23:451–478, 1995.

W.P. Dillon, M.W. Lee, K. Fehlhaber, and D.R. Coleman. Gas hydrates on the Atlantic continental margin of the United States–controls on concentration. In D.G. Howell, editor, *The future of energy gasses*, volume 1570 of *US Geological Survey Professional Paper*, pages 313–330. 1993.

D. J. Dodds. Attenuation estimates from high resolution subbottom profiler echoes. In *Saclant Asw Research Conference on Ocean Acoustics Influienced by the Sea Floor*, volume 907, page 19, La Spezia, Italy, 1980. Plenum Press.

N. Driscoll and J.B. Diebold. Tectonic and stratigraphic development of the Caribbean: New constraints from multichannel seismic data. In P. Mann, editor, *Caribbean Basins. Sedimentary Basins of the World*, volume 4, pages 591–627. Elsevier Science B. V., Amsterdam, 1999.

Neal W Driscoll, J. K. Weissel, and J. A. Goff. Potential for large-scale submarine slope failure and tsunami generation along the U.S. mid-Atlantic coast. *Geology*, 28(5):407–410, 2000.

B Dugan and P.B. Flemings. Overpressure and fluid flow in the New Jersey continental slope: Implications for slope failure and cold seeps. *Science*, 289: 288–291, 2000.

R.W. Embley and R.D. Jacobi. Mass wasting in the western North Atlantic. In P.R. Vogt and B.E. Tucholke, editors, *The Western North Atlantic region*, volume M, pages 479–490. Boulder Colorado, Geological Society of America, 1986.

D. Evans, E.L. King, N.H. Kenyon, C. Brett, and D. Wallis. Evidence for long-term instability in the Storrega Slide region off western Norway. *Marine Geology*, 130:281–292, 1996.

M. A. Fisher, W. Normark, H. G. Greene, H. J. Lee, and R. Sliter. Geology and tsunamigenic potential of submarine landslides in Santa Barbara Channel, Southern California. *Marine Geology*, 224:1–22, 2005.

R. A. Fisher. Dispersion on a sphere. *Proc. Roy. Soc. London, Ser. A*, 217: 295–305, 1953.

J.V. Gardner, D.B. Prior, and M.E. Field. Humboldt Slide - a large shear-dominated retrogressive slope failure. *Marine Geology*, 154:323–338, 1999.

L. Granar. Magnetic measurements on swedish varved sediments. *Arkiv. for Geo.*, 3:1–40, 1958.

A. Harding. pltsegy, http://trident.ucsd.edu/~alistair/pltsegy/pltsegy_main.html. 2005.

P. Henkart. SIOSIES, http://sioseis.ucsd.edu. 2005.

G. R. Hext. The extimation of second-order tensors, with related tests and designs. *Biometrika*, 50:353–357, 1963.

Jenna C Hill, Neal W Driscoll, J. K. Weissel, and J. A. Goff. Large-scale elongated gas blowouts along the U.S. Atlantic margin. *J. Geophys. Res.*, 109 (B09101):14, 2004.

W.S. Holbrook. Seismic studies of the Blake Ridge: implications for hydrate distribution, mathane expulsion, and free gas dynamics. In C.K. Paull and W.P. Dillon, editors, *Natural Gas Hydrates: Occurrence, Distribution, and Detection*, volume 124 of *Geophysical Monograph*. AGU, 2001.

W.S. Holbrook, D. Lizarralde, I.A. Pecher, A.R. Gorman, K.L. Hackwith, M. Hornbach, and D. Saffer. Escape of methane gas through sediment waves in a large methane hydrate province. *Geology*, 30(5):467–470, 2002.

G. Ising. On the magnetic properties of varved clay. *Arkiv. For. Mate., Astr., Och Fys.*, 29:1–37, 1942.

V. Jelinek. Statistical processing of anisotropy of magnetic susceptibility measured on groups of specimens. *Studia Geophys. et geol.*, 22:50–62, 1978.

J. L. Kirschvink. The least-squares line and plane and the analysis of paleomagnetic data. *Geophys. Jour. Roy. Astron. Soc.*, 62:699–718, 1980.

H. J. Lee, J. P. M. Syvitski, G. Parker, D. Orange, J. Locat, E. W. H. Hutton, and J. Imran. Distinguishing sediment waves from slope failure deposits: field examples, including the "Humboldt slide", and modelling results. *Marine Geology*, 192(1-3):79–104, 2002.

U. T. Mello and G. D. Karner. Developement of sediment overpressure and its effect on thermal maturation: Application to the Gulf of Mexico Basin. *AAPG Bulletin*, 80(9):1367–1396, 1996.

L. F. Pratson and B. J. Coakley. A model for the headward erosion of submarine canyons induced by downslope eroding sediment flows. *Geological Society of America Bulletin*, 108(2):225–234, 1996.

A. I. Rees. The use of anisotropy of magnetic susceptibility in the estimation of sedimnentary fabric. *Sedimentology*, 4:257–271, 1965.

J. Rosenbaum, R. Reynolds, J. Smoot, and R. Meyer. Anisotropy of magnetic susceptibility as a tool for recognizing core deformation: reevaluation of the paleomagnetic record of pleistocene sediments from drill hole OL-92, Owens Lake, California. *Earth Planet. Sci. lett.*, 178:415–424, 2000.

A. N. Shor, D. V. Kent, and R. D. Flood. Contourite or turbidite?: magnetic fabric of fine-grained Quaternary sediments, Nova Scotia continental rise, fine-grained sediments: Deep water processes and facies. In D.A.V. Stowe and D.J.W. Piper, editors, *Fine-grained sediments: deep water processes and facies*, pages 257–273. Blackwell Scientific Publications, 1984.

J. W. Stockwell. The CWP/SU: Seismic Un*x package. *Computers and Geosciences*, 25(4):415–419, 1999.

L. Tauxe. *Paleomagnetic Principles and Practice*. Klewer Academic Publishers, 1998.

Fabio Trincardi, Antonio Cattaneo, Annamaria Correggiari, and Domenico Ridente. Evidence of soft sediment deformation, fluid escape, sediment failure and regional weak layers within the late Quaternary mud deposits of the Adriatic Sea. *Marine Geology*, 213(1-4):91–119, 2004.

Steven N. Ward. Landslide tsunami. *Journal of Geophysical Research*, 106 (B6):11201–11216, 2001.

J. D. A. Zijderveld. A.C. demagnetization of rocks: analysis of results. In D. Collinson, editor, *Methods in Paleomagnetism*, pages 254–286. Chapman and Hall, 1967.